

ABSTRACT

Title of Document: CHARGE TRANSPORT IN GRAPHENE WITH ADATOM OVER-LAYERS ; CHARGED IMPURITY SCATTERING, DIELECTRIC SCREENING, AND LOCALIZATION.

Chaun Jang, Doctor of Philosophy, 2011

Directed By: Professor, Michael S. Fuhrer,
Department of Physics.

Graphene, a single atom thick plane of graphite, is a novel two-dimensional electron system in which the low-energy electrons behave as massless chiral Dirac fermions. This thesis explores the effects of disorder in graphene through controlled surface modification in ultra-high vacuum (UHV), coupled with *in situ* electronic transport experiments. Three different roles of adatom overlayers on graphene are investigated. First, the effects of charged impurity scattering are studied by introducing potassium ions on the graphene at low temperature in UHV. The theoretically expected magnitude and linear density-dependence of the conductivity due to long range Coulomb scattering is verified. Second, the effective dielectric constant of graphene is modified by adding ice overlayers at low temperature in UHV. The opposing effects of screening on scattering by long range (charged impurity) and short range

impurities are observed as variations in conductivity, and the changes are in agreement with Boltzmann theory for graphene transport within the random phase approximation. The minimum conductivity of graphene is roughly independent of charged impurity density and dielectric constant, in agreement with the self-consistent theory of screened carrier density inhomogeneity (electron and hole puddles). Taken together, the experimental results on charged impurity scattering and dielectric screening strongly support that long range Coulomb scattering is the dominant scattering mechanism in as-fabricated graphene on SiO₂. In addition to the semi-classical transport properties, quantum transport is also studied with cobalt decorated graphene. Strong localization is achieved in the disordered graphene through deposition of cobalt nanoclusters. In finite magnetic field a phase transition occurs from the localized state to the quantum Hall state. Scaling analysis confirms that the transition is a quantum phase transition which is similar to the localization - delocalization transitions in other two dimensional electron systems.

CHARGE TRANSPORT IN GRAPHENE WITH ADATOM OVER-LAYERS ;
CHARGED IMPURITY SCATTERING, DIELECTRIC SCREENING, AND
LOCALIZATION.

By

Chaun Jang

Dissertation submitted to the Faculty of the Graduate School of the
University of Maryland, College Park, in partial fulfillment
of the requirements for the degree of
Doctor of Philosophy
2011

Advisory Committee:
Professor Michael S. Fuhrer, Chair
Professor Christopher J. Lobb
Associate Professor Min Ouyang
Associate Research Scientist William G. Cullen
Professor Janice E. Reutt-Robey

© Copyright by
Chaun Jang
2011

Acknowledgements

I could not imagine the completion of this important work without helps from all my friends in Maryland.

First of all, I would like to thank my advisor, Professor Michael S. Fuhrer. He has given me lots of freedom to wondering around many research projects, and allowed me to co-work with other students. Supports and guidance from him prove that my first delight of joining his group was not an overreaction. I wonder how he could take care of all the members such well in spite of the big size of his group.

I would also like to thank the members of my dissertation committee, Prof. Christopher J. Lobb, Prof. Min Ouyang, Prof. Janice E. Reutt-Robey and Dr. William G. Cullen, for honoring me by serving in my committee.

I would like to thank Professor Ellen D. Williams and members of her group. Most of my experiments using UHV system were supported by Prof. Williams. She was a good caregiver to a naive graduate student like me. And I am especially grateful to Masahiro Ishigami and Jian Hao Chen. I learned a lot of laboratory skills from them and it was great pleasure to work with the talented scientists with sense of humors.

I would like to thank all the group members whom I met during my graduate program. Enrique Cobas, Adrian Southard, Daniel Lenski, Tareq Ghanem, Gokhan Esen, Brad Conrad, Tracy Moore, SungJae Cho, Shudong Xiao, David Tobias, Alexandra Curtin, Claudia Ojeda, Jun Yan, Kristen Burson, Michelle Zimmermann, Harold Cai, Jack Hellerstedt, Liang Li, Jinglei Ping, Jacob Tosado, Mahito

Yamamoto, and Dohun Kim. They have been responsible for the equipment maintenance and training the instruments. And they have willingly shared their experiences and knowledge in science (also in life) to deal with my problems.

I would like to thank Prof. Das Sarma, Dr. Shaffique Adam, Dr. Euyheon Hwang, for the discussions and theories in this dissertation. I also would like to thank all the staffs working in the department.

I made so many Korean friends in Maryland. I will miss the meals and refreshing chats (topics from high energy physics to biology) with the friends, Hanhee Paik, Jaekwang Jeong, Hyeokshin Kwon, Hongsuk Kang, Dujin Kim, Zaeill Kim, Dohun Kim, Youngsoo Yoon, Youngnoh Yoon, Hongki Min, and Jonghee Lee.

Lastly, I would like to thank my parents and a sister. I am feeling sorry for not being with them to pursue my selfish desire for science. I do appreciate for their endless love and belief.

Table of Contents

Acknowledgements.....	ii
Table of Contents.....	iv
List of Figures.....	vi
Chapter 1 : Introduction to graphene, a new type of two dimensional electron system	1
Chapter 2 : Theoretical Background.....	7
2.1 Impurity scattering in graphene.....	7
2.2 Minimum conductivity of graphene.....	11
2.3 Quantum Hall effects in graphene; disorder effects.....	13
2.4 Magnetic field induced delocalization in 2D system.....	15
Chapter 3 : Experimental Methods.....	20
3.1 Fabrication of Graphene Field Effect Device.....	20
3.2 The Helitran ultra-high vacuum compatible LT-3B open cycle cryostat.....	25
3.3 Transport measurements (lock-in technique) in ultra-high vacuum.....	27
3.4 Adatom deposition.....	28
3.4.1 Potassium deposition.....	30
3.4.2 Ice deposition.....	30
3.4.3 Co deposition.....	31
Chapter 4 : Charged impurity scattering in graphene.....	33
4.1 Methods.....	45
4.2 Supplementary Information.....	47
4.2.1 Theoretical predictions for charged impurity scattering in graphene.....	47
4.2.2 Experimental studies of transport in graphene.....	50

4.2.3 Comparison of our work to theory.....	51
4.2.4 Effect of Impurity Charge $Z \neq 1$	54
4.2.5 Determination of Potassium Dosing Rate.....	54
Chapter 5 : Tuning the effective fine structure constant in graphene ; opposing effects of dielectric screening on short- and long-range potential scattering	56
Chapter 6 : Magnetic Field induced insulator-quantum Hall conductor transition in disordered graphene	69
Chapter 7 : Summary	83

List of Figures

Figure 1.1 Graphene band structure from tight binding calculation.	3
Figure 2.1 Gate voltage dependent conductivity of graphene device.	8
Figure 2.2 QHE in graphene.	15
Figure 2.3 I-QH transition in GaAs/AlGaAs heterostructure.	16
Figure 2.4 Phase diagrams of the integer quantum Hall effect (IQHE).	17
Figure 3.1 Optical microscope image of an exfoliated flake containing graphene on 300nm SiO ₂ /Si substrate.	21
Figure 3.2 Micro-Raman spectroscopy of a single layer graphene.	22
Figure 3.3 Optical microscope image of graphene Hall bar device.	23
Figure 3.4 Removal of resist residue by annealing in H ₂	24
Figure 3.5 The LT-3B ultra high vacuum compatible cryostat with dimensions.	26
Figure 3.6 Schematic of a low frequency lock-in technique.	28
Figure 3.7 Photograph of the UHV chamber (top) and schematic of the system (bottom).	29
Figure 3.8 Mini e-beam evaporator with dimensions.	32
Figure 4.1 Optical micrograph and Raman spectrum of a graphene device.	35
Figure 4.2 Potassium doping of graphene.	36
Figure 4.3 Inverse electron mobility $1/\mu_e$ and hole mobility $1/\mu_h$ vs. doping time.	38
Figure 4.4 Shift of minimum conductivity point with doping.	40
Figure 4.5 Change in behavior near minimum conductivity point with doping.	42
Figure 5.1 Schematic illustrating dielectric screening in graphene.	58

Figure 5.2 Conductivity of the graphene device as a function of back-gate voltage..	60
Figure 5.3 μ_{sym} , σ_{sym} and σ_{min} as a function of number of ice layers.....	62
Figure 6.1 ρ_{xx} vs V_g for different temperatures, and Raman spectroscopy of the disordered device	72
Figure 6.2 Temperature dependences of the ρ_{xx} for different carrier densities.....	74
Figure 6.3 Longitudinal and Hall resistivities $\rho_{\text{xx}}, \rho_{\text{xy}}$ of cobalt-decorated graphene as a function of gate voltage at 10 T and 2.5 K.....	76
Figure 6.4 Phase transition at a fixed gate voltage.	78
Figure 6.5 The phase transition at different carrier densities (gate voltages).....	80

Chapter 1 : Introduction to graphene, a new type of two dimensional electron system

Because of its fundamental simplicity as well as applications of metal-oxide-semiconductor field effect transistor (MOSFET) devices in the silicon electronics industry, the research on electrons confined in two dimensions has become a leading edge of modern condensed matter physics. The studies of two dimensional electron systems (2DES) emerged from investigations of the semiconductor - oxide interface in MOSFETs. The quantum Hall effect in 2DESs [1] is a remarkable example of new physics which has enriched our understanding of the nature of 2D electrons in high magnetic fields. As semiconductor film growth techniques have improved, more advanced research on 2DESs has been enabled by making semiconductor hetero-junctions and quantum wells [2,3].

Meanwhile there are naturally formed materials such as graphite which offer new possibilities for making 2DESs if they can be made thin enough. Graphite is composed of covalently-bonded two-dimensional sheets of carbon arranged in a hexagonal lattice, called graphene, stacked upon each other and bonded through weak van der Waals forces to form a three-dimensional solid. Due to the weak bonding between graphene sheets, graphite can be peeled apart or exfoliated to produce thin films. The isolation of a single sheet of graphite by this method has been a longtime goal for researchers [4,5]. In 2004 this concept became a reality when Novoselov *et al.* [6] reported astonishing experimental results of graphene field effect devices

fabricated by the exfoliation technique. Stimulated by the observation, a tremendous number of publications on graphene from researchers around the world soon followed, and the 2010 Nobel Prize was awarded to the Kostya Novoselov and Andre Geim as the pioneers of graphene discovery.

Why was the realization of the graphene field effect device so exciting? And what makes it different from the other conventional 2DESs? One answer lies in graphene's unusual band structure, first calculated almost 60 years before the work of Novoselov and Geim [7-9]. The tight binding calculation taking into account up to second-nearest neighbor hopping term gives an approximate analytic equation (1.1) for graphene's conduction band (+) and valence band (-),

$$E_{\pm}(q) \approx 3t' \pm \hbar v_F |\vec{q}| - \left(\frac{9t'a^2}{4} \pm \frac{3ta^2}{8} \sin(3\theta_q) \right) |\vec{q}|^2, \quad (1.1)$$

where t (t') is the nearest (second nearest) neighbor hopping amplitude with $t \approx 2.5$ eV $\gg t' \approx 0.1$ eV, a is the distance between carbon atoms (0.14 nm), q is the 2D wave vector measured from the K point of the Brillouin zone, and

$v_F = 3ta/2$, $\theta_q = \arctan^{-1}[q_x/q_y]$. Eqn. (1.1) is valid for small $q \ll 2\pi/a$. At low energy (keeping only linear- q terms), and defining the energy $E(q=0) = 0$, we have the linear dispersion relation

$$E_{\pm}(q) = \pm \hbar v_F q + O(q/k)^2 \quad (1.2)$$

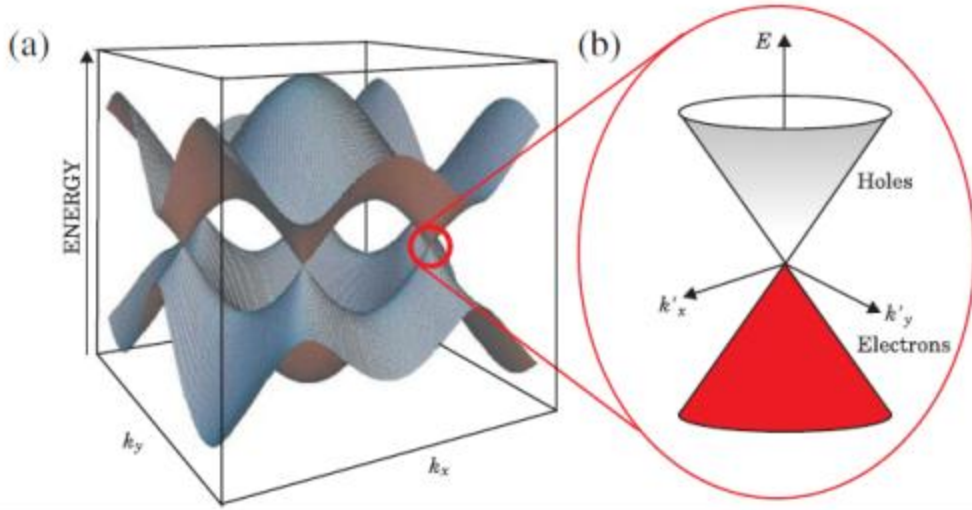


Figure 1.1 Graphene band structure from tight binding calculation. Adapted from ref.[10]. (a) Graphene band structure. (b) Enlargement of the band structure close to the K and K' points showing the Dirac cones.

As shown in figure 1.1, graphene has a linear dispersion relation, with conduction and valence band crossing at $q = 0$. Graphene is hence a zero band-gap semiconductor with linear long-wavelength dispersion for both carriers (electron, hole). The energy depends on the graphene Fermi velocity, $v_F \sim 10^8$ cm/s (1/300 of the velocity of light).

There is another peculiar property in graphene carrier dynamics due to the presence of sublattices A and B (two atoms per unit cell). Using the nearest neighbor tight binding Hamiltonian, in which Fourier transformed operators are expanded near K (K') point in the BZ, the resulting effective low energy Hamiltonian is

$$H = \hbar v_F \begin{pmatrix} 0 & q_x - iq_y \\ q_x + iq_y & 0 \end{pmatrix} = \hbar v_F \vec{\sigma} \cdot \vec{q}, \quad (1.3)$$

and the wavefunction satisfies the massless Dirac equation

$$-i\hbar v_F \vec{\sigma} \cdot \nabla \Psi(\vec{r}) = E \Psi(\vec{r}), \quad (1.4)$$

where $\vec{\sigma} = (\sigma_x, \sigma_y)$ is the 2D Pauli matrices and $\Psi(\vec{r})$ is a 2 component electron wave function. The Hamiltonian near the K' point is the complex conjugate of the Hamiltonian near the K point (equation (1.3)) [11] In momentum space, eigenfunctions for the equation (1.4) can be written as

$$\psi(\mathbf{q}, \mathbf{K}) = \frac{1}{\sqrt{2}} \begin{pmatrix} e^{-i\theta_q/2} \\ \pm e^{i\theta_q/2} \end{pmatrix}, \quad (1.5 \text{ a})$$

$$\psi(\mathbf{q}, \mathbf{K}') = \frac{1}{\sqrt{2}} \begin{pmatrix} e^{i\theta_q/2} \\ \pm e^{-i\theta_q/2} \end{pmatrix}, \quad (1.5 \text{ b})$$

where \pm correspond to the eigenenergies $E = \pm \hbar v_F q$. Under rotation of θ , the change of the wave functions sign (phase change by π) indicates that the wave function is a 2D spinor, termed pseudospin, analogous to real electron spin. Because the helicity (chirality) is defined as the projection of the momentum operator along the direction of pseudospin, the wave functions are also eigenstates of the helicity operator, thus the chirality is well defined in graphene related to the pseudospin.

In addition to the quasi-relativistic physics of carriers, graphene has other properties that make it distinct from other 2DESs. Graphene is a perfect two dimensional system with atomic thickness. The carriers are truly confined in a 2D plane and the outsides of the plane are exposed to the environment directly. In contrast, in the conventional semiconductor 2DESs, the confinement of electrons in a 2D plane is obtained by tuning the electrical properties of outer layers of the heterostructures. Hence the conventional 2DES is embedded in a 3 dimensional material, and environmental control of the 2DESs is highly limited. However in

graphene, unlike the other 2DES, modification of the surrounding properties can be achieved simply by depositing materials on graphene, or transferring graphene to different substrates. This opens the experimental possibility of tuning the properties of graphene through addition of adatoms or overlayers while measuring electrical transport of the massless Dirac fermions.

In this thesis I present experimental observations of changes in electrical transport signals of graphene with three different types of materials on graphene. To minimize the effects from environmental contaminants other than the test materials, graphene devices are placed in an ultra-high vacuum chamber. Then electrical signals from the devices are measured *in situ* while I introduce materials of interests on the graphene in the UHV. For the high magnetic field measurements on highly disordered graphene with cobalt nanocluster decoration in Chapter 6, I measured the transport properties of graphene *ex situ* after the cobalt deposition in the UHV. Chapter 2 lays out the theoretical framework for understanding charge transport in graphene in the presence of disorder, which is used for analyses of the experimental results in the following chapters (Ch. 4 - 6), on impurity scattering and the localization-delocalization transition in graphene. In chapter 3, I describe the experimental methods used in the work, including the fabrication of graphene field-effect devices, and the measurement of graphene transport *in situ* in ultra-high vacuum. Chapter 4 – 6 of this thesis consists of independent research results. Chapter 4 is devoted to the effect of adsorbed potassium on graphene, which acts as a charged impurity [12]. Chapter 5 presents a study of the effect of modifying the dielectric environment of graphene using ice overlayers as a clean dielectric deposited in UHV [13]. Chapter 6

covers the insulator - quantum Hall transition in disordered graphene realized by decoration with Co particles. Finally, in the last chapter (chapter 7) I will summarize the thesis with brief introductions of follow up (future) researches.

Chapter 2 : Theoretical Background

In this chapter I review the theory of charge carrier transport in graphene in the presence of charged impurity disorder and weak point disorder (delta-function correlated disorder) within semi-classical Boltzmann transport theory using the random phase approximation (RPA) for calculation of the screening properties of graphene. Section 2.1 develops the theory of graphene's conductivity at high carrier density. Section 2.2 describes the "self-consistent theory" for the minimum conductivity in graphene with charged impurity disorder. For the transport beyond the semi-classical model, quantum Hall effect with magnetic field is discussed in section 2.3, and strong localization in graphene and the insulator-quantum Hall phase transition induced by magnetic field in 2DESs are discussed in section 2.4.

2.1 Impurity scattering in graphene

In spite of the theoretical expectation of the carrier density-independent conductivity, $\sigma(n) = \text{constant}$, of graphene due to the linear dispersion relation [14], experiments reported that the conductivity of graphene depends linearly on carrier density n , i.e. $\sigma(n) \propto n$ [15-17]. A typical conductivity curve of graphene as a function of the back gate voltage, which is applied from a highly doped silicon substrate through SiO₂ gate dielectric, is shown in figure 2.1. The carrier density is given by $n = c_g(V_g - V_{g,\text{CNP}})/e$, where $c_g = 1.15 \times 10^{-8} \text{ F/cm}^2$ is the gate capacitance per unit area for the 300 nm thick SiO₂ gate dielectric, e the elementary charge, and $V_{g,\text{CNP}}$ the gate voltage at charge neutrality. Both positive and negative (electron and

hole) carrier densities can be tuned by the back gate voltages. Figure 2.1 shows that the conductivity is ambipolar, symmetric for electrons and holes (as expected since graphene has electron-hole symmetry at low energy), and has roughly linear carrier density dependence. Near the charge neutral point, where the carrier changes from electron to hole, the conductivity does not vanish, rather saturates to a value called minimum conductivity (σ_{\min}). The transport curve can be considered as combination of two regions; roughly linear conductivity at high density and constant conductivity at low density. The intersection of the two different regions defines the width of the plateau (ΔV_g).

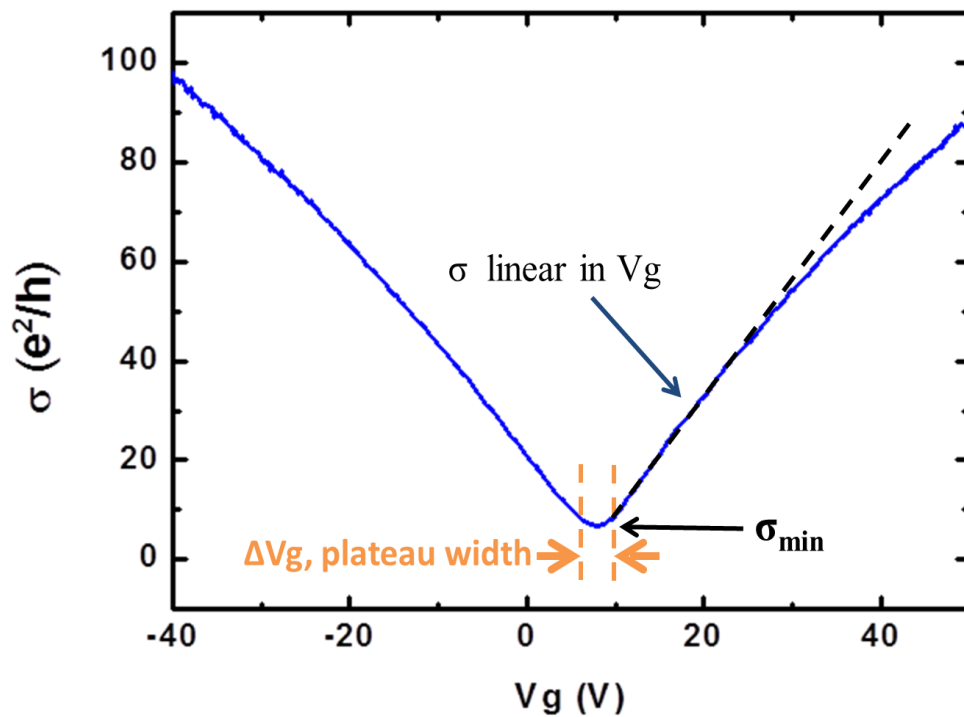


Figure 2.1 Gate voltage dependent conductivity of graphene device.

To explain the linear dependence of graphene's conductivity on charge carrier density, long-range disorder (Coulomb potential impurity) was proposed in many theoretical studies [18-24]. Adam *et al.* described the minimum conductivity of graphene as due to spatially-fluctuating carrier density (electron and hole “puddles”) induced by the random charged impurity potential [25]. The self-consistent screening of the impurity potential by the induced carrier density was then used to calculate graphene's minimum conductivity, and the results were able to explain the relative independence of the minimum conductivity on disorder strength. Below I discuss these theories in more detail.

For graphene, semi-classical diffusive conductivity is given by

$$\sigma = \frac{2e^2 E_F \tau}{h}. \quad (2.1.1)$$

$$\frac{1}{\tau} = \frac{4E_F}{\pi\gamma^2} \int_0^1 d\eta \eta^2 \sqrt{1-\eta^2} \left| \frac{V(\eta)}{\varepsilon(\eta)} \right|^2, \quad (2.1.2)$$

where e is the elementary charge, h is Planck's constant, E_F is the Fermi energy, $\hbar^{-1}\gamma$ is the Fermi velocity, $V(\eta)$ is impurity scattering potential, the momentum transfer $q = |k - k'| = 2k_F \eta$, and $\varepsilon(\eta)$ is the static RPA dielectric function [26] and is given by

$$\varepsilon(\eta) = 1 + \frac{g_s g_v \pi}{8} \frac{e^2}{\kappa \gamma} + \frac{2\pi e^2}{\kappa \eta} \Pi^+(\eta), \quad (2.1.3)$$

where g_s , and g_v are the spin and valley degeneracies, Π^+ is the intraband polarizability, and κ is the background lattice dielectric constant. Note that the screening decreases as κ increases.

Using scattering potential for long range impurity, $V^L(\eta) = \frac{\sqrt{n_{imp}} \pi e^2}{\kappa k_F \eta}$,

conductivity due to long range disorder is obtained as

$$\sigma^L = \frac{2e^2}{h} \left(\frac{n}{n_{imp}} \right) \frac{1}{F_1(2r_s)}, \quad (2.1.3)$$

$$\frac{F_1(x)}{x^2} = \frac{\pi}{4} + 3x - \frac{3x^2\pi}{2} + x(3x^2 - 2) \frac{\arccos[1/x]}{\sqrt{x^2 - 1}},$$

where $r_s = e^2/\kappa\hbar v_F$ is the effective fine structure constant of graphene which has no carrier density dependence. For graphene on SiO₂, the effective dielectric constant $\kappa = 2.5$ (average of dielectric constants of SiO₂ and vacuum), $F_1(2r_s) = 0.1$ and the conductivity is

$$\sigma = 20 \frac{e^2}{h} \left(\frac{n}{n_{imp}} \right). \quad (2.1.4)$$

From the results, the dependence of mobility on the impurity density and the dielectric constant of the environments is predicted; testing these predictions experimentally is the subject of chapters 4 and 5.

Even though it is believed that the Coulomb scattering has the dominant effect on charge transport in graphene, there are still additional scattering mechanisms.

Especially for short range disorder, such as point defects or dislocations in the carbon lattice, the conductivity calculation is straightforward with scattering potential

$V^S(\eta) = \sqrt{n_{imp}} V_0$, where V_0 is a constant short range potential strength. [27] The

calculated conductivity due to short range disorder is

$$\sigma^s = \frac{4\pi e^2}{h} \frac{\gamma^2}{n_{imp} V_0^2} \frac{1}{F_2(2r_s)}, \quad (2.1.5)$$

$$F_2(x) = \frac{\pi}{2} - \frac{16x}{3} + 40x^3 + 6\pi x^2 - 20\pi x^4 + 8x^2(5x^3 - 4x) \frac{\arccos[1/x]}{\sqrt{x^2 - 1}}$$

The result indicates that the conductivity due to short range scattering has no carrier density dependence even when including screening, but the conductivity could be changed by tuning the dielectric constant of the environment. A combination of short- and long-range scattering in graphene will lead to a sublinear $\sigma(n)$ which is generally experimentally observed (see Fig. 2.1). This hypothesis is verified in chapter 5, where the effects of dielectric constant change on the conductivity (due to long- and short-range scattering) are experimentally verified with ice deposition on graphene.

2.2 Minimum conductivity of graphene

The minimum conductivity of graphene, the saturation of the linear in density conductivity at low carrier density, is another interesting issue which has been extensively studied by theorists. If an ideally clean graphene is considered, a universal minimum conductivity, $\sim 4e^2/\pi h$, is calculated based on the Kubo and Landauer formulas [28]. However, experimental results showed that the observed minimum conductivities are not universal rather vary around the range, $4-8 e^2/h$, which is larger than the theoretical value [12,17,29]. In the presence of Coulomb disorder, graphene is never undoped, and the Fermi energy cannot lie uniformly at the Dirac point over a macroscopic sample. The random Coulomb potential produces electron and hole puddles. Recently both analytical and numerical results

successfully explained the magnitude and disorder dependence of the minimum conductivity by considering the effects of electron and hole puddles.[25,30,31]

Using a self-consistent approximation, where the puddle density is calculated by considering the potential of the charged impurities screened self-consistently by the puddle carrier density, a theory was developed by Adam *et al.* [25] to relate the impurity density and the minimum conductivity. A calculation within RPA gives the rms carrier density in the puddles n^* as

$$\begin{aligned} \frac{n^*}{n_{imp}} &= 2r_s^2 C_o^{RPA}(r_s, a = 4d\sqrt{\pi n^*}), \\ C_o^{RPA}(r_s, a) &= -1 + \frac{4E_1(a)}{(2 + \pi r_s)^2} + \frac{2e^{-a}r_s}{1 + 2r_s} \\ &\quad + (1 + 2r_s a)e^{2r_s a} (E_1[2r_s a] - E_1[a(1 + 2r_s)]), \end{aligned} \quad (2.2.1)$$

where d is the impurity distance to graphene, and $E_1(z) = \int_z^\infty t^{-1} e^{-t} dt$ is the exponential integral function. From the determination of n^* , the pinned carrier density which leads to the minimum constant conductivity, the minimum conductivity value and plateau width ΔV_g may be calculated [25]. The minimum conductivity is given by

$$\sigma_{\min} = n^* e \mu. \quad (2.2.2)$$

,where μ is field effect mobility. The plateau width in gate voltage $\Delta V_g = 2n^*e/c_g$ [25].

The predicted dependence of the minimum conductivity on impurity density and dielectric constant are studied in chapters 4 and 5 respectively.

2.3 Quantum Hall effects in grahpene; disorder effects

One of the most striking phenomena stemming from the Dirac nature of the massless fermions in graphene is the unique quantum Hall effect (QHE). In the presence of magnetic field perpendicular to the 2D plane, quantized energy levels (Landau levels, LL) can be calculated by solving the Dirac equation in magnetic field [32-35]. The result is

$$E_n = \text{sgn}(n)\hbar\omega_c\sqrt{|n|}, \quad \text{with } n = 0, \pm 1, \pm 2, \dots \quad (2.3.1)$$

where $\omega_c = v_F\sqrt{2eB/(\hbar c)}$ is a ‘cyclotron frequency’, and v_F is the fermion velocity.

Differently from the conventional (semiconductor) 2DES, there is a LL at zero energy.

Moreover the quantization for the Hall conductivity, σ_{xy} , has the unconventional form as depicted in Figure 2.2 (a),

$$\sigma_{xy} = \nu \frac{e^2}{h} = 4\left(n + \frac{1}{2}\right) \frac{e^2}{h}, \quad n = 0, \pm 1, \pm 2, \dots \quad (2.3.2)$$

where $\nu = n\Phi_0/B$ is the LL filling factor, Φ_0 is the flux quantum, and B is the magnetic field strength. The $\frac{1}{2}$ -shift to the conventional integer quantum Hall effect (IQHE) can be understood as the factor induced by the additional Berry phase which the electrons acquire when completing a closed orbit due to their chiral nature [36,37].

According to the scaling theory of localization, in the absence of magnetic field there are only localized states in a non-interacting 2 dimensional electron system (2DES) at low temperature for any amount of disorder in the system [38]. When a strong magnetic field applied perpendicular to the 2DES, LL quantization becomes important and it is possible to observe QHE which indicates the existence of extended

states. In understanding the underlying physics of the QHE phenomena and the associated phase transition (localization-delocalization), the topological character and disorder effects are essential factors, and the same statements could be applied to the unconventional QHE in graphene. Recently D. N. Sheng *et al.* [39] carried out a numerical study using a tight binding model with random disorder and established the phase diagram of the system (Figure 2.2 (b)) As shown in the figure, the following properties are predicted for QHE of disordered graphene: (1) the quantum Hall plateaus can be destroyed with strong disorder (or weak magnetic field), (2) the $\nu=2$ QH state is the most robust to the disorder strength, and (3) an insulating region emerges at zero energy with relatively weak disorder.

Using as-fabricated graphene on SiO₂, which is weakly disordered with the dominant disorder thought to be long-wavelength charged impurity scattering which does not produce localization, many groups have reported the phase transitions in magnetic field, such as the plateau-plateau transition (e.g., arrow D in figure 2.2 (b))[40], and the plateau to $N = 0$ insulator transition (arrow A in figure 2.2 (b))[41,42]. Yet the transitions from insulator to higher order LL quantum Hall states (e.g., arrow F in figure 2.2 (b)) have not been observed experimentally due to a lack of insulating states in normal graphene [40-42].

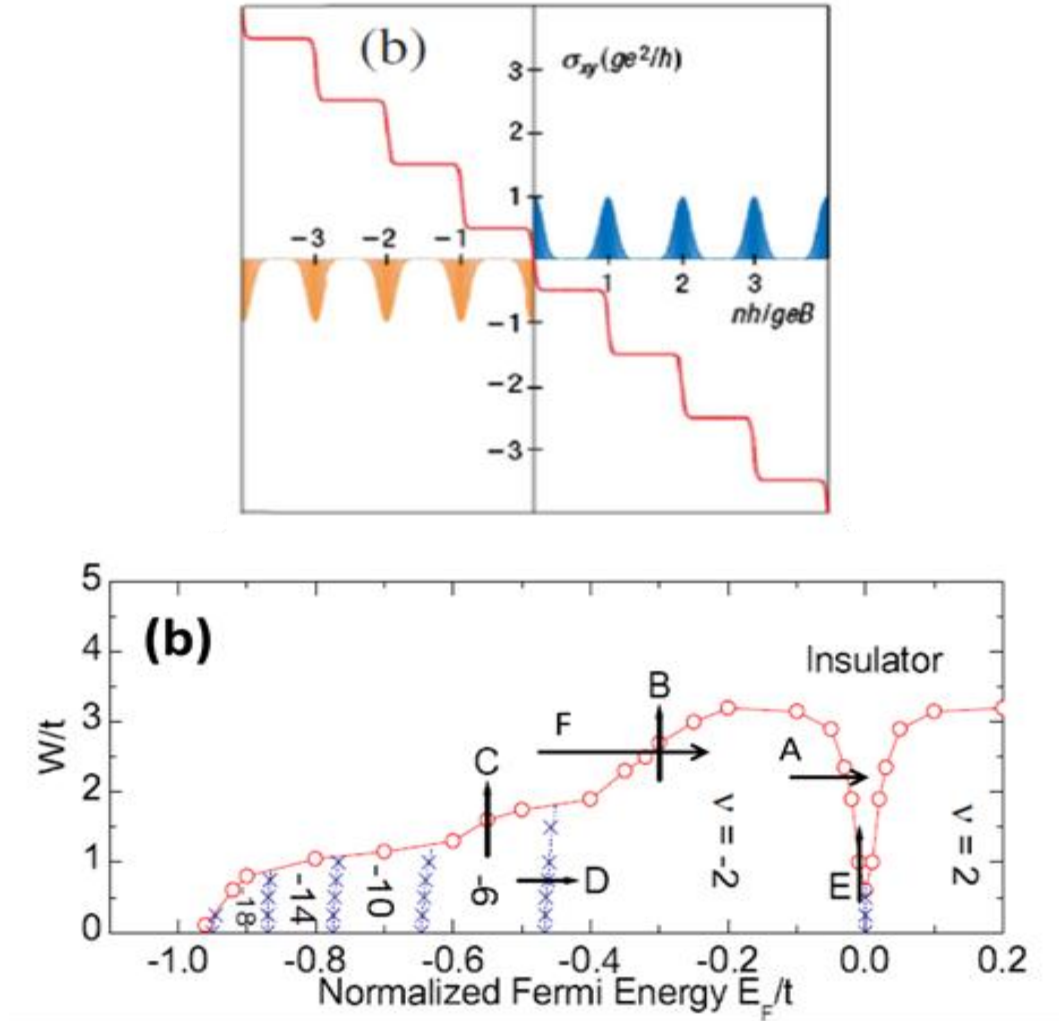


Figure 2.2 QHE in graphene.
 (a) Illustration of the unconventional QHE in graphene. Adapted from Ref. [43].
 (b) Phase diagram for the unconventional QHE with disorders. W/t is the normalized disorder strength. Arrows are examples of the possible phase transitions. Adapted from ref. [39].

2.4 Magnetic field induced delocalization in 2D system

To explain the connection between the extended states at finite B and the localized state at $B = 0$, Khmel'nitskii [44] and Laughlin [45] developed a scaling argument. In the argument, the extended states could float up in energy as magnetic

field decreases, and eventually energies of all the extended states could be higher than the Fermi level (i.e. the system becomes an insulator). Using the float up scenario, the global phase diagram (GPD) of integer QHE was constructed later by Kivelson *et al.* [46]. The only possible phase transition from the insulator to the $\nu=1$ QH state, predicted by the GPD, has been observed experimentally in many 2DEGs [47-53] (one of the examples is presented in figure 2.3).

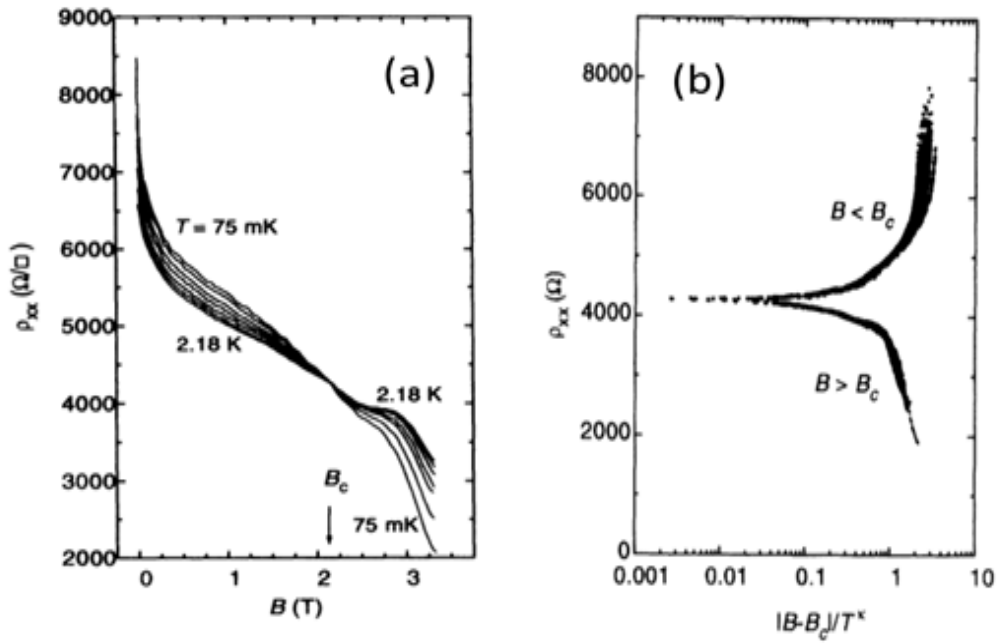


Figure 2.3 I-QH transition in GaAs/AlGaAs heterostructure. (a) magnetoresistance curves for the sample. Transition from insulating (left) to metallic (right) is separated by the critical magnetic field B_c (b) Scaling analysis with ρ_{xx} against $|B-B_c|/T^k$ (dimensionless scaling variable). The collapsed data verifies phase transition of the system. Figures are adapted from ref.[51]

In addition to the float up scenario, a new picture with destruction of the extended state by increasing disorder (or decreasing B) was proposed [54,55] to explain the experimental observations of a transition from insulator to QH state with filling factor higher than 1, which is forbidden in GPD [49,56,57]. In the phase diagram constructed by numerical simulations with the tight binding model, the direct transitions from insulating state to QH state with arbitrary filling factors are possible (see figure 2.4).

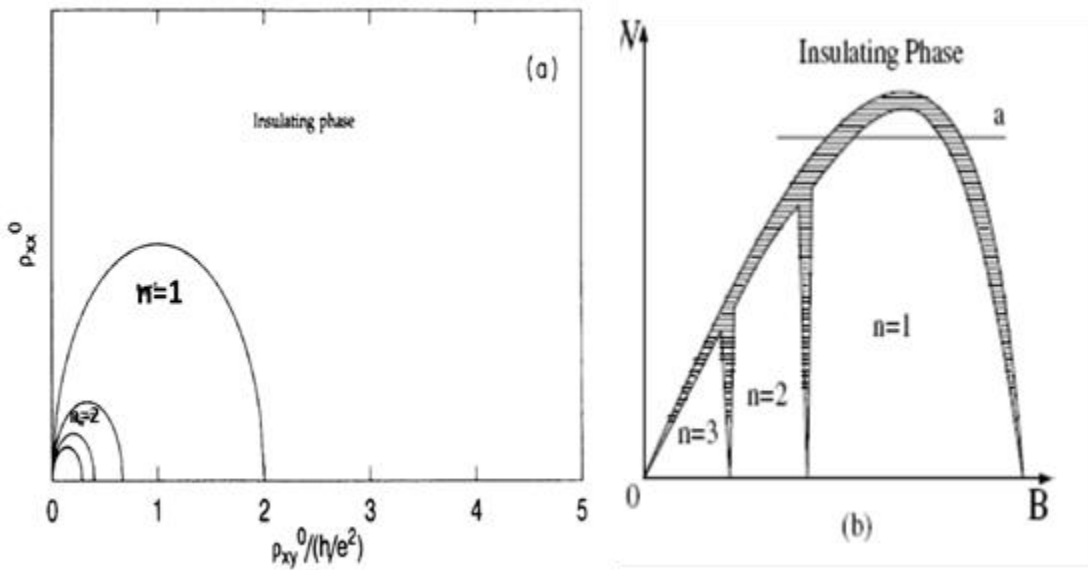


Figure 2.4 Phase diagrams of the integer quantum Hall effect (IQHE). (a) global phase diagram of the IQHE. Adapted from ref. [46] (b) An example of phase diagram of the IQHE from numerical calculation. Adapted from ref. [58] For both graphs, x axis is the magnetic field and y axis is the disorder strength.

To study the insulator-quantum Hall phase transition discussed above in graphene, realization of strong localization is essential. However, localization of charges in graphene is somewhat different from other 2DESs with massive electrons because of the chiral Dirac fermions in two valleys at K and K' points of the first BZ, exhibiting Berry phase π . Weak localization results from the constructive interference of wavefunctions traveling in opposite directions around closed loop scattering paths. When the chiral charge travels around phase coherent closed loops, it acquires a phase difference π , which gives rise to destructive interference and weak anti-localization. In a perfect massless Dirac system this weak-antilocalization (WAL), suppression of the back scattering behavior is expected and the system should remain metallic to $T = 0$. The WL can be restored if inter-valley scattering is considered, which mix pseudospins of different valleys (break the chirality). Higher-order terms in the Hamiltonian also do not conserve chirality. Upon further enhancement of the inter-valley scattering, when the localization length is comparable to phase coherence length, it is expected to induce strong localization (Anderson insulating state) in graphene [59]. Inter-valley scattering can be increased by introducing short range impurities which break sublattice symmetry. In chapter 6, insulating graphene is achieved by chemisorption of Co clusters on graphene, and the transition from insulator into the $\nu = 2$ QH state with magnetic field is studied.

It is argued that the plateau-plateau transition of 2DES can be described with the universal temperature scaling exponent ($\xi = 0.42$) in certain conditions (low temperature, short range scattering dominant limit) [60,61]. But in graphene, through the numerical calculations [62,63], it is unlikely that the argument of universality of

the scaling exponent holds due to the nature of relativistic 2D fermions. The theoretical study of the lowest LL in graphene [63], by considering tight binding Hamiltonian with disorder, shows that the localization length exponent can be varied as the system is tuned from weak to strong disorder. The similar results, new class of universality compared to the conventional 2DESs, are also obtained employing a Supersymmetric technique with disorders which give rise to inter-valley scattering [62].

Chapter 3 : Experimental Methods

In this chapter, experimental techniques used in the subsequent chapters are presented. Section 3.1 describes fabrication methods of graphene field effect devices which are used for the electrical transport studies of graphene covered in chapters 4-6. In section 3.2, the Helitran ultra-high vacuum (UHV) compatible open cycle cryostat is presented. Section 3.3 covers the electrical transport measurements in UHV with schemes of experimental setup. The measurements methods described in section 3.3 are used in the rest of the thesis (Ch. 4-6). The last section, section 3.4, consists of three different adatom deposition methods for potassium (Ch.4), water or ice (Ch.5), and cobalt (Ch.6).

3.1 Fabrication of Graphene Field Effect Device

In order to get graphene devices which will be used in the experiments of subsequent chapters, the mechanical exfoliation [6] method was used by starting from either Kish graphite or natural graphite. The graphite flakes are exfoliated on highly doped silicon wafers with 300 nm SiO₂ over layer. The low resistivity silicon layer can be used as back gate electrode and the oxide layer operates as the gate dielectric material. The 300 nm oxide layer also gives good color contrast at visible wavelengths for single layer graphene on the wafer, which makes it easier to find graphene under the optical microscope.

Figure 3.1 shows a typical optical micrograph of a graphite flake after the exfoliation. Single-layer regions can be identified by optical contrast alone, but the

number of layers in the flake is confirmed from Raman spectra obtained by using the Horiba Jobin-Yvon LabRAM HR-VIS micro-Raman system (with 633nm laser). As shown in the Figure 3.2, single layer graphene can be identified by the unique single Lorentzian 2D peak in the spectrum [64].

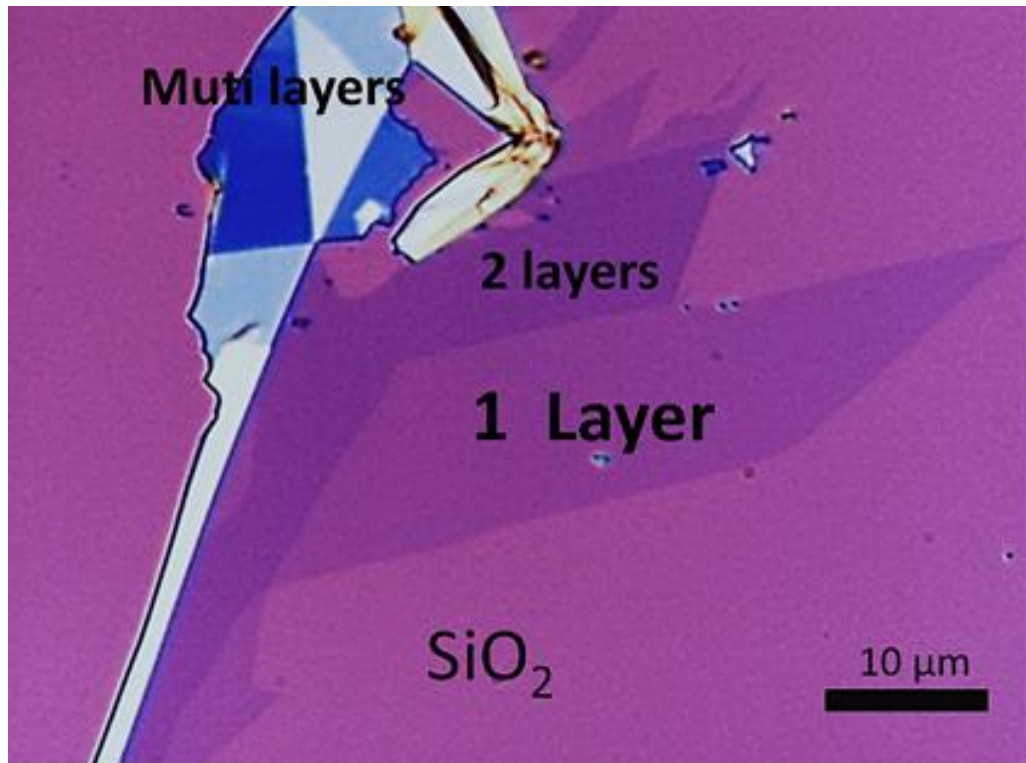


Figure 3.1 Optical microscope image of an exfoliated flake containing graphene on 300nm SiO₂/Si substrate. The number of graphene layers can be distinguished from contrasts of the flake area.

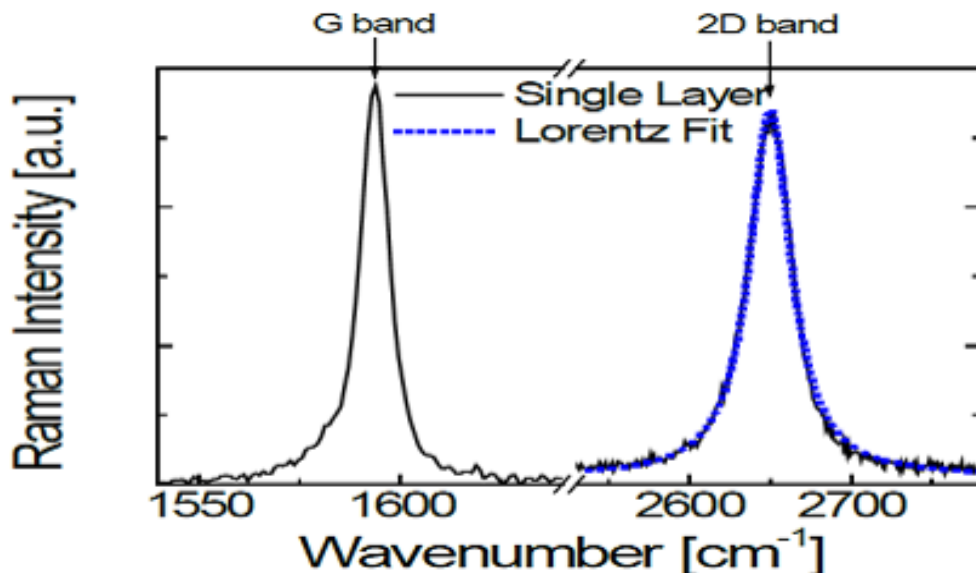


Figure 3.2 Micro-Raman spectroscopy of a single layer graphene. The single Lorentzian 2D band at approximately 2650 cm^{-1} verifies the single layer graphene.

The exact positioning of the etching mask and electrode patterns on the graphene flake is achieved using the alignment function provided in the Nanometer Pattern Generation System (NPGS). For the process, alignment marks (consists of square gold pads) are deposited near the graphene flake through the same metal lift off process. The alignment pattern works as a reference to the graphene flake position in all the subsequent patterns. When the shape of the graphene is not convenient for connecting electrical contacts, the flake is patterned into a Hall bar shape by oxygen plasma etching [65] with reactive ion etcher. A mask for the etching is prepared by electron-beam lithography (using an FEI corporation XL-30 SEM, and NPGS) using poly(methyl methacrylate) resist (950 PMMA A4, MicroChem Corp.) spun at 6000rpm for 1 minute over the graphene followed by developing in the developer liquid (IPA/MIBK 3:1) for 1 minute. Electrodes for the device are also

lithographically defined by electron beam lithography similar to the etching mask fabrication, except that a bilayer resist of MMA/MAA copolymer (MMA EL11, MicroChem Corp., spun at 4000 rpm for 1 minute and 950 PMMA A4 (6000 rpm for 1 minute)) are used. The double layer resist is used to get a good undercut profile after electron beam exposure and development which is required for the metal lift off process. Final metal contacts are made after thermal evaporation of 3 nm chromium (as an adhesion layer) and 80 nm gold followed by the lift off in acetone. (see figure 3.3)

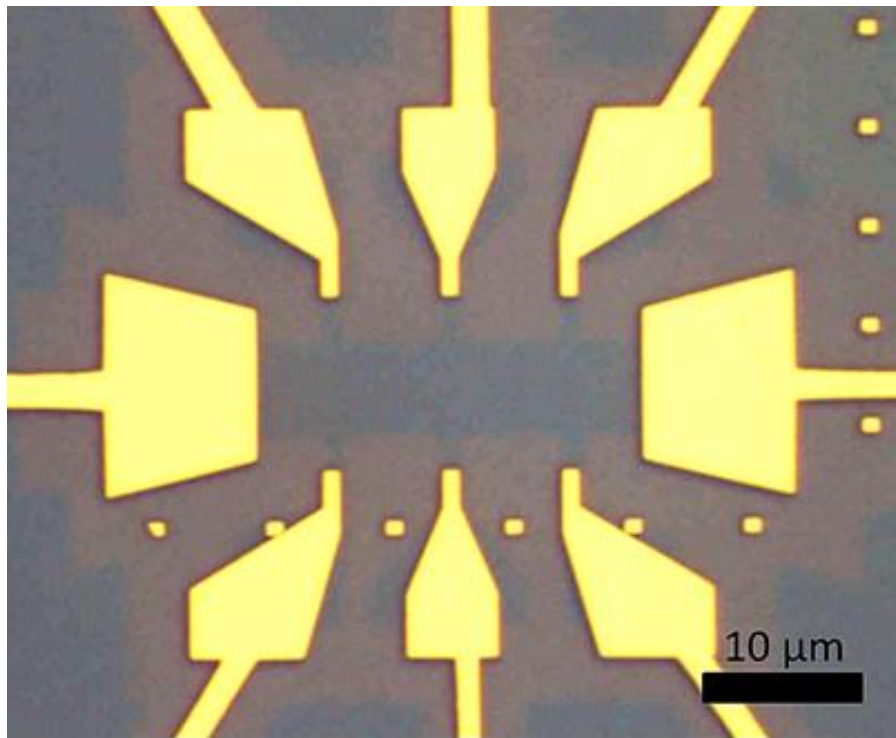


Figure 3.3 Optical microscope image of graphene Hall bar device. Graphene (dark purple) is patterned by oxygen plasma etching and Cr/Au electrodes (yellow color) are connected. Small squares are used for alignment of patterns for the etching and the electrode deposition.

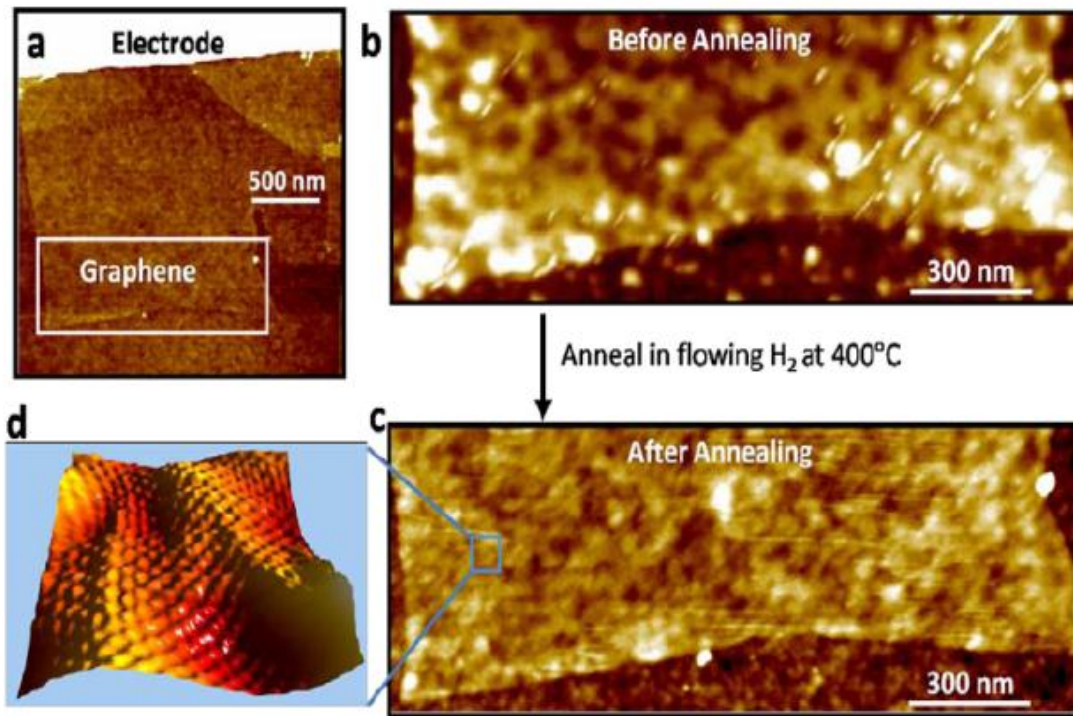


Figure 3.4 Removal of resist residue by annealing in H₂.

(a) Non-Contact AFM topography of clean graphene device on SiO₂ substrate; b)&c) Zoomed-in AFM images of graphene on SiO₂ (white rectangle in a) before (b) and after (c) removal of PMMA residue; d) atomically-resolved STM micrograph of the cleaned graphene surface. Figures from ref. [66]

Before placing the devices in a ultra-high vacuum (UHV) chamber, the devices are annealed in flowing H₂ and Ar (with flow rate of H₂ 1700 ml/min, Ar 1900 ml/min) at 350 °C for 1 hour to remove resist residues [12,66]. In figure 3.4, the effect of the annealing is presented by comparing images of the surface before and after the cleaning process. The devices after H₂ annealing are usually heavily doped when exposed to the air (mainly doped with oxygen mediated by water molecules in the air), however the doping in ambient condition could be removed by overnight bake out in the UHV at 450 - 490 K [12].

3.2 The Helitran ultra-high vacuum compatible LT-3B open cycle cryostat

The Helitran UHV compatible LT-3B open cycle cryostat (designed and manufactured by Advanced Research Systems Inc.) allows us to perform electrical transport measurements in UHV at various temperature ranges. Through multi-pin UHV feedthroughs of the cryostat (See figure 3.5), wires for electrical signals are connected between instruments placed outside of the chamber and devices in the chamber. Using liquid helium or liquid nitrogen, the temperature at the sample stage could be cooled down to 10K (for liquid helium) and 77K (for liquid nitrogen). In the open cycle cryostat, the coolant evaporates at the cold tip and the resultant gas runs out to the exhaust port (see Figure 3.5). Control of the temperature at the sample stage is accomplished by adjusting evaporated gas flow rate at the end of the exhaust port. The experimentally achieved lowest temperature (10 K which is higher than one specified in the manual 4.2 K) is attributed to additional thermal load from electrical wiring anchored to the cold finger and a custom sample stage added at the end of the cold tip. For baking the sample at the temperature higher than 400 K, which is essential for removing doping in the air, a heater is attached to the cold tip. All the temperatures measured here are obtained using DT 670 silicon diodes as thermometers placed close to the sample stage.

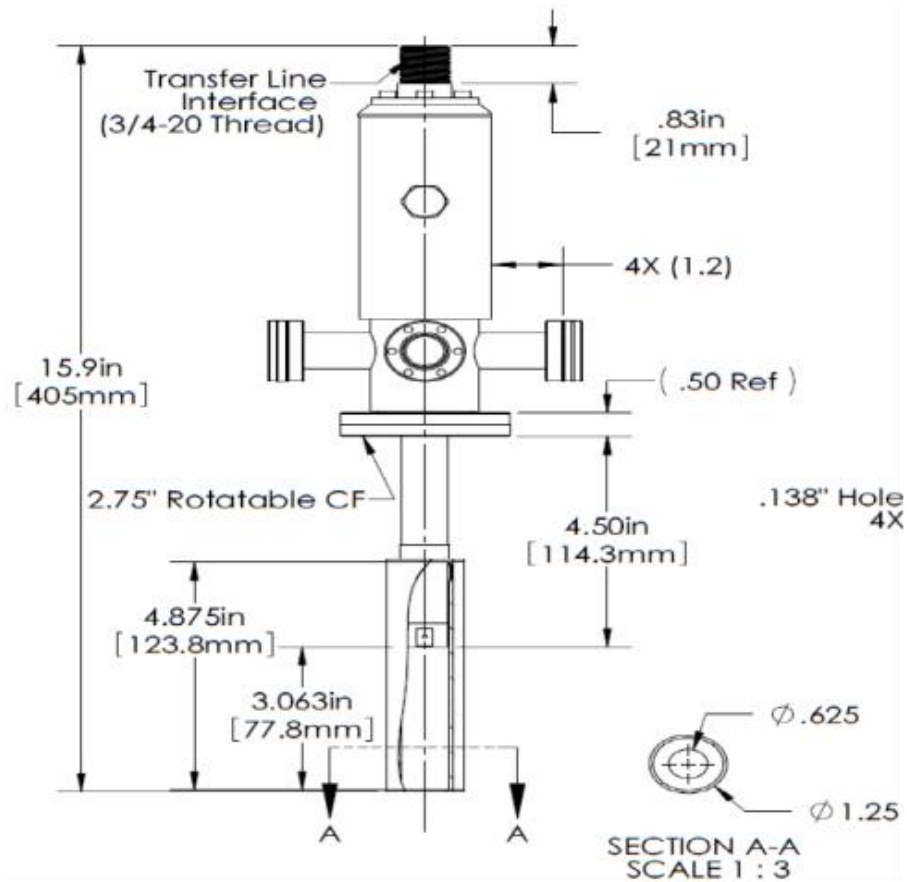
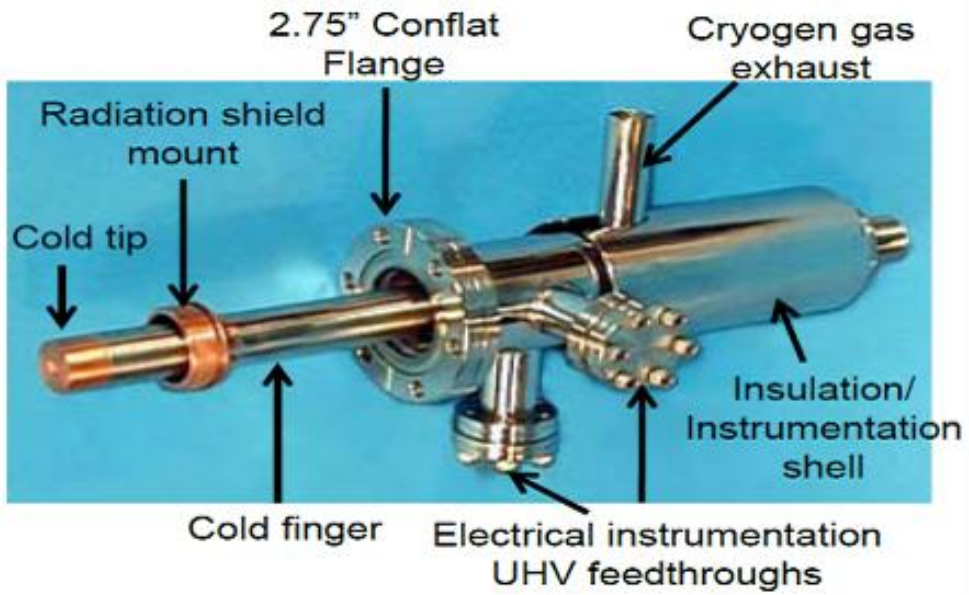


Figure 3.5 The LT-3B ultra high vacuum compatible cryostat with dimensions. Electrical wires and custom sample stage not shown. Drawing from Advanced Research Systems, Inc.

3.3 Transport measurements (lock-in technique) in ultra-high vacuum

For the longitudinal resistivity measurements (and Hall measurements in Ch. 6) of the graphene device, the conventional four-probe low-frequency lock-in technique is used. One (or two for Hall measurements in Ch. 6) Stanford SR830 lock-in amplifier is used as both a signal source and a phase-sensitive voltage detector. The phase-sensitive detection of AC signal with known frequency is effective in reduction of electrical noise with frequencies which are not close to the input signal frequency. [67] Because of the relatively low resistance of graphene devices (0.1~10 k Ω), the voltage output of the lock-in amplifier can be converted to a current source by connecting a 10M Ω resistor ($R_s \gg R_{\text{device}}$) in series to the circuit. The measured voltage difference is collected in the computer through either DAC board or GPIB cable. To minimize Joule heating, the current is limited to 50-100 nA. The frequency of the source was set to be in a range of 17-220 Hz. The charge carrier density of the device can be tuned by applying back gate voltage to the doped silicon substrate from a Keithley source meter. The total schematic of the measurements is depicted in figure 3.6

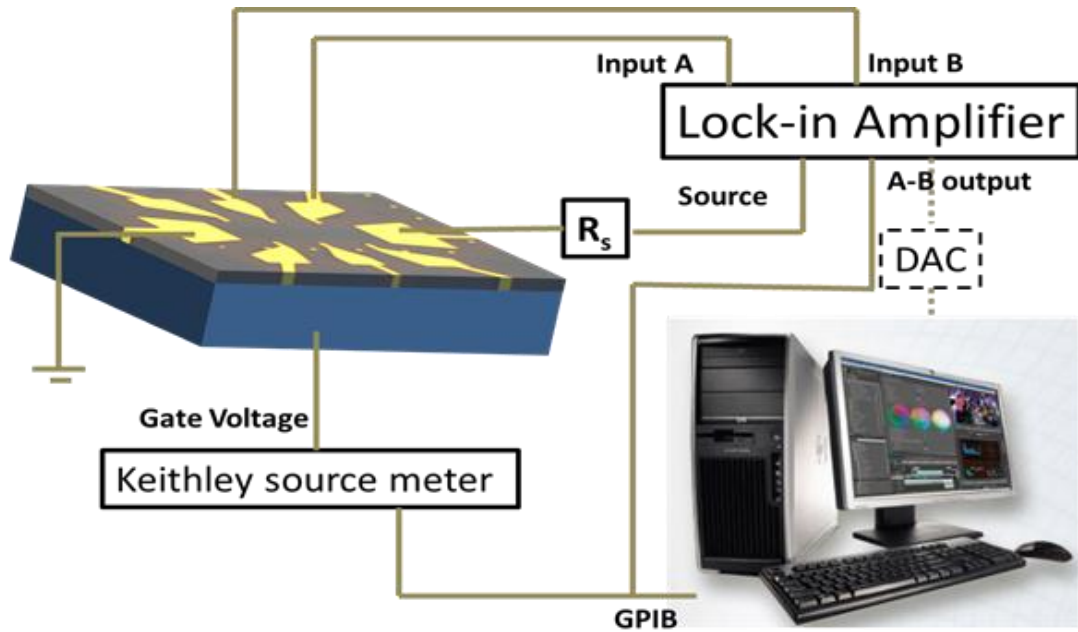


Figure 3.6 Schematic of a low frequency lock-in technique.

A low frequency AC voltage applied through the resistor R_s ($=10\text{ M}\Omega$) is used as a current source. And the gate voltage is applied to Si substrate from a Keithley source meter. A-B outputs of the lock-in amplifier are transferred to a computer through either a DAC board or GPIB connections.

3.4 Adatom deposition

Once the graphene field effect device is fabricated and loaded in the UHV chamber, electrical transport measurements are carried out while adatoms are introduced from sources installed at the other side of the chamber (see figure 3.7). In the research described in this thesis, I have used three different kinds of sources for adatom deposition. Subsection 3.4.1 describes the evaporation source used to deposit potassium, a model charged impurity on graphene, for the experiments described in chapter 4. Subsection 3.4.2 describes the method of ice deposition, which is used to modify the dielectric environment of graphene as discussed in chapter 5. Subsection

3.4.3 describes cobalt deposition by e-beam evaporator which is used to create disordered insulating graphene for the studies in chapter 6.

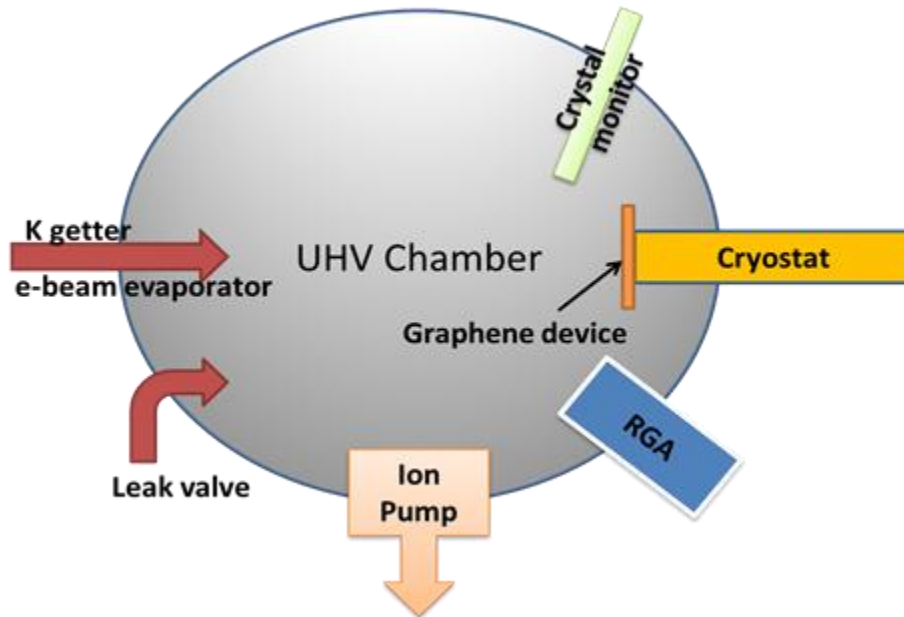
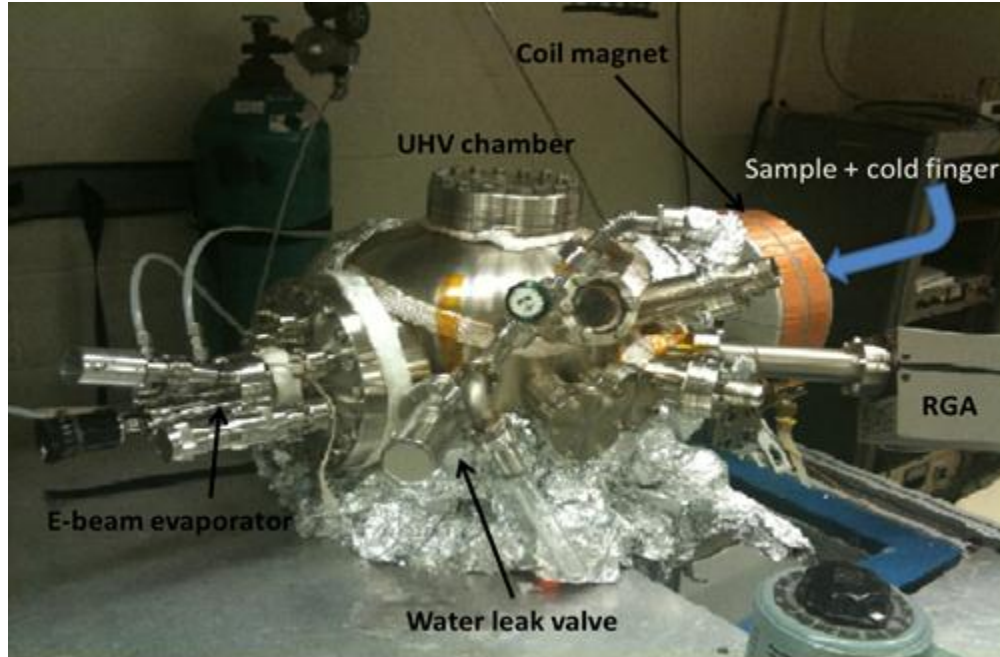


Figure 3.7 Photograph of the UHV chamber (top) and schematic of the system (bottom).

The cryostat with device is not installed (position is indicated as a blue arrow) in the UHV chamber photo.

3.4.1 Potassium deposition

As a source of charged impurity on graphene, a commercially available potassium (K) source (potassium getter, SEAS getters) is chosen. The getter consists of packed reactive materials placed in an open metal container for use in a vacuum system. When it is heated up, the reactive material evaporates and adsorbs gases. Thus the getter is usually used to maintain the vacuum by removing small amounts of gases in the evacuated and sealed system. The getter is placed to the UHV chamber on the opposite side to the LT-3B cryostat installed (with device). The getter was outgassed during bake out of the UHV chamber by applying 2 to 3 A from a power supply, while the sample stage is covered with a shutter placed between the source and the cold tip of the cryostat. Then actual deposition on graphene is performed with preheating (passing 6 to 7 A for 40 s) followed by opening (2 s) the shutter. More details are presented in *methods* of chapter 4.

3.4.2 Ice deposition

In order to introduce high purity water, which will be leaked into the UHV chamber as a source of ice layer formation on graphene, Nanopure water is prepared in a tube which is connected to a leak valve and a turbo pump. Several cycles of degassing process known as ‘freeze-pump-thaw’ is followed to remove residual gases dissolved in the water. During the process, the tube is placed into iced acetone to freeze water then the frozen tube (also ice) is pumped out using the external turbo pump. When the frozen ice melts in room temperature at low pressure, dissolved gases boils out, thus the water can be purified by repeating the cycle. A low rate of

introducing water molecules into the chamber is achieved by the leak valve and the partial pressure of water in the chamber is monitored by a residual gas analyzer (RGA) positioned off-axis and behind the sample (see figure 3.7). The position of the leak valve knob which produces a partial pressure of $\sim 5 \times 10^{-8}$ torr is marked during the calibration using RGA. Then the total exposure of the sample to water molecules introduced into the chamber is controlled by varying the valve opening time from 5 to 20 seconds while keeping the leak rate set as before. Note that the time for the exposure is comparable to the reaction time of the leak valve (time delay to reach the calibrated target pressure), hence the uncertainties in estimation of ice layer numbers could be big.

3.4.3 Co deposition

For the deposition of cobalt atoms as a magnetic impurity on graphene, a small electron-beam evaporator (EGN 4, Oxford Applied Research) is used. As a source, a cobalt rod (99.995%, Alfa Aesar) is installed in the evaporator. The evaporation rate of the cobalt is controlled by adjusting e-beam power while monitoring the ion current and simultaneously the evaporation rate using a quartz-crystal film-thickness monitor. In the experiments presented in chapter 6, an evaporation rate less than 0.1 \AA/s (measured at the crystal monitor) is used with 20 to 21 W of electron-beam power (corresponding to 50 nA of ion currents). The total amount of cobalt evaporated on the graphene device is estimated to be around 1 nm when accounting for the position of the crystal monitor and the sample stage relative to the evaporator. As shown in figure 3.8, a shutter can be used to control exposure of

the evaporated flux to the sample stage and a water line is connected for cooling the source.

After the cobalt deposition, the sample is warmed up and baked at 430K overnight which is expected to lead to irreversible formation of Co clusters on the graphene device. AFM images of the final device are obtained *ex situ* to verify the nano-clusters on graphene directly (see chapter 6).

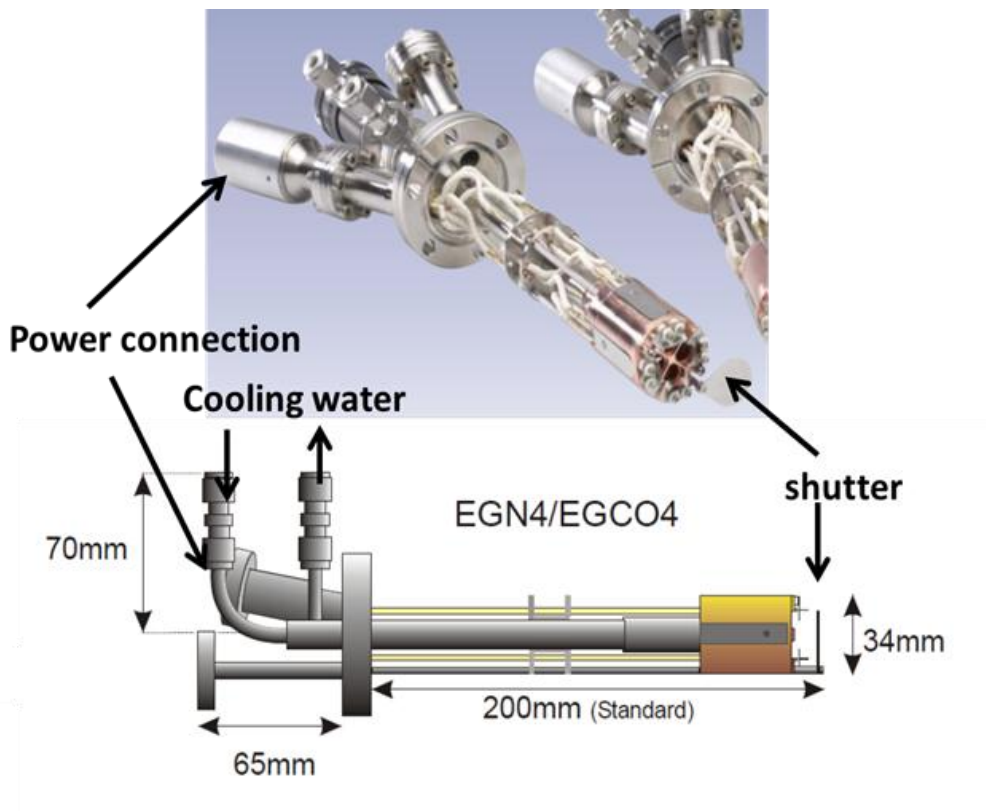


Figure 3.8 Mini e-beam evaporator with dimensions. Image and drawing from Oxford Applied Research

Chapter 4 : Charged impurity scattering in graphene¹

Since the initial demonstration of the ability to experimentally isolate a single graphene sheet [6], a great deal of theoretical work has focused on explaining graphene's unusual carrier-density-dependent conductivity $\sigma(n)$, and its minimum value (σ_{min}) of nearly twice the quantum unit of conductance ($4e^2/h$) [6,16,17,29,68,69]. Potential explanations for such behavior include short-range disorder [18,21,32,70], 'ripples' in graphene's atomic structure [71,72] and the presence of charged impurities [18,19,21,22,25,73-75]. Here, we conduct a systematic study of the last of these mechanisms, by monitoring changes in electronic characteristics of initially clean graphene [66] as the density of charged impurities (n_{imp}) is increased by depositing potassium atoms onto its surface in ultrahigh vacuum. At non-zero carrier density, charged-impurity scattering produces the widely observed linear dependence [6,16,17,29,68,69,76] of $\sigma(n)$. More significantly, we find that σ_{min} occurs not at the carrier density that neutralizes n_{imp} , but rather the carrier density at which the average impurity potential is zero [25]. As n_{imp} increases, σ_{min} initially falls to a minimum value near $4e^2/h$. This indicates that σ_{min} in the present experimental samples [6,16,17,29,68,69,76] is governed not by the physics of the Dirac point singularity [77,78], but rather by carrier-density inhomogeneities induced by the potential of charged impurities [21,22,25,69].

¹ This chapter was adapted from: C. Jang, J.-H. Chen, S.Adam, M.S. Fuhrer, and E.D. Williams, and M.Ishigami, *Nature Physics* **4**, 377 (2008)

Several theoretical studies [18,19,21,22,25,73-75] have predicted charged-impurity scattering in graphene to produce $\sigma(n)$ of the form

$$\sigma(n) = Ce \left| \frac{n}{n_{imp}} \right| + \sigma_{res}, \quad (4.1)$$

where C is a constant, e is the electronic charge and σ_{res} is the residual conductivity at $n = 0$ (this last term was predicted only in refs [74,75]). Hwang *et al.*[22] first calculated the screened Coulomb potential within the random phase approximation, and used the results to determine $C = 5 \times 10^{15} V^{-1} s^{-1}$. Novikov [73] noted that, beyond the Born approximation used in ref. [22], an asymmetry in C for attractive versus repulsive scattering (electron versus hole carriers) is expected for Dirac fermions. Experimentally, the behavior described by equation (4.1) is ubiquitously observed in graphene, strongly suggesting that charged-impurity scattering is the dominant scattering mechanism in present samples. Here, we provide the first direct verification of equation (4.1) for charged-impurity scattering in graphene, and determine the constant C . We also observe the expected asymmetry for attractive versus repulsive scattering for Dirac fermions [73].

At low carrier density, the conductivity does not vanish linearly, but rather saturates to a constant value near $4e^2/h$ (ref. [17]). Early theoretical work [77,78] on massless Dirac fermions predicted $\sigma_{min} = 4e^2/\pi h$ for vanishing disorder. However, in the presence of charged impurities, a finite conductivity $\sim 4e^2/h$ is predicted over a plateau of width ΔV_g [21,22,25]. Here, we measure experimentally the dependence on n_{imp} of σ_{min} , ΔV_g and the gate voltage $V_{g,min}$ at which the minimum conductivity occurs,

and find agreement with theoretical predictions [21,22,25], indicating that disorder due to charged impurities is the relevant physics at the minimum conductivity point in present samples.

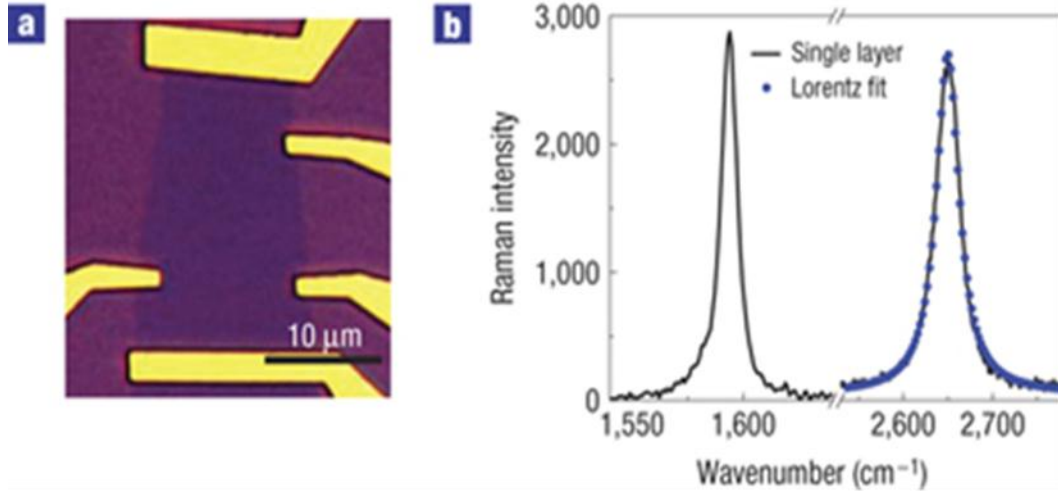


Figure 4.1 Optical micrograph and Raman spectrum of a graphene device. (a) Optical micrograph of the device. (b) 633 nm micro-Raman shift spectrum acquired over the device area, with Lorentzian fit to the D' peak, confirming that the device is made from single-layer graphene (vertical scale is same throughout b).

Figure 4.1(a) shows the graphene device used in this study, and Fig. 4.1(b) shows its micro-Raman spectrum; the single Lorentzian D' peak confirms that the device is single-layer graphene [64] (see the *Methods* section). To vary the density of charged impurities, the device was dosed with a controlled potassium flux in sequential 2 s intervals at a sample temperature $T = 20$ K in ultrahigh vacuum (UHV). The gate-voltage-dependent conductivity $\sigma(V_g)$ was measured *in situ* for the pristine device, and again after each doping interval. After several doping intervals, the device was annealed in UHV to 490 K to remove weakly adsorbed potassium [79], then

cooled to 20 K and the doping experiment repeated; four such runs (runs 1–4) were carried out in total.

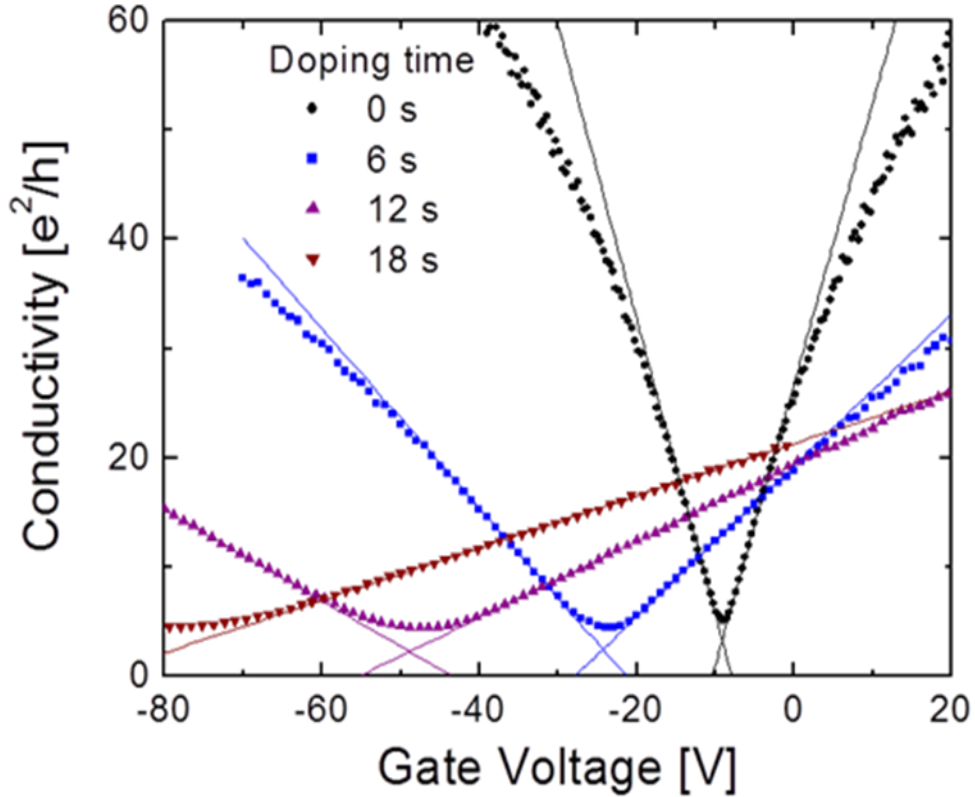


Figure 4.2 Potassium doping of graphene.

The conductivity (σ) vs. gate voltage (V_g) curves for the pristine sample and three different doping concentrations taken at 20K in ultra-high vacuum are shown. Data are from Run 3. Lines are fits to equation (4.1), and the crossing of the lines defines the points of the residual conductivity and the gate voltage at minimum conductivity ($\sigma_{res}, V_{g,min}$) for each data set. The variation of σ_{min} with impurity concentration is shown in Figure 4.5.

Figure 4.2 shows the conductivity versus gate voltage for the pristine device and at three different doping concentrations at 20 K in UHV for run 3. On K-doping, (1) the mobility decreases, (2) $\sigma(V_g)$ becomes more linear, (3) the mobility asymmetry for holes versus electrons increases, (4) the gate voltage of minimum

conductivity $V_{g,min}$ shifts to more negative gate voltage, (5) the width of the minimum conductivity region in V_g broadens and (6) the minimum conductivity σ_{min} decreases, at least initially (see also Fig. 4.5 below). In addition, (7) the linear $\sigma(V_g)$ curves extrapolate to a finite σ_{res} at $V_{g,min}$. All of these features have been predicted [18,19,21,22,25,73-75] for charged-impurity scattering in graphene; we will discuss each in detail below.

Effects (4) and (5) were observed in a previous study in which graphene was exposed to molecular species [80]. However, the authors reported no changes in mobility, concluding that charged-impurity scattering contributes negligibly to the mobility of graphene. As discussed further in the *Supplementary Information* section, the previous experiments did not control the environment and had low initial sample mobility. The failure to observe effects (1)–(3) therefore is most likely due to the presence of significant concentrations of both positively and negatively charged impurities [80,81], although the presence of water and resist residue [66] may also be contributing factors [80].

We first examine the behavior of $\sigma(V_g)$ at high carrier density. For V_g not too near $V_{g,min}$, the conductivity can be fitted (Fig. 4.2) by

$$\sigma(V_g) = \begin{cases} \mu_e c_g (V_g - V_{g,min}) + \sigma_{res} & V_g > V_{g,min} \\ -\mu_h c_g (V_g - V_{g,min}) + \sigma_{res} & V_g < V_{g,min} \end{cases} \quad (4.2)$$

where μ_e and μ_h are the electron and hole field-effect mobilities, c_g is the gate capacitance per unit area, $1.15 \times 10^{-4} \text{ Fm}^{-2}$, and σ_{res} is the residual conductivity that is determined by the fit. The mobilities are reduced by an order of magnitude during each run, and recover on annealing. The electron mobilities ranged from 0.081 to 1.32

$m^2 V^{-1} s^{-1}$ over the four runs, nearly covering the range of mobilities reported so far in the literature ($\sim 0.1 - 2 m^2 V^{-1} s^{-1}$) [17,29,69].

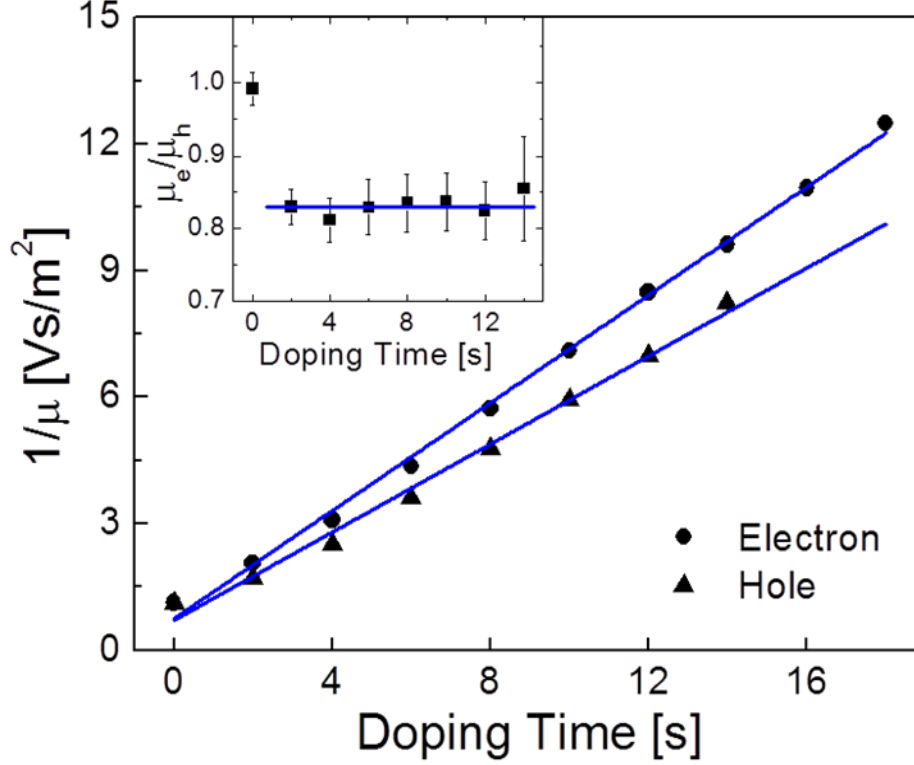


Figure 4.3 Inverse electron mobility $1/\mu_e$ and hole mobility $1/\mu_h$ vs. doping time. Experimental error determined from standard error propagation is less than 4% (see *Methods*). Lines are linear fits to all data points. Inset: The ratio of μ_e to μ_h vs. doping time. Error bars represent experimental error in determining the mobility ratio from the fitting procedure (see *Methods*). Data are from run 3 (same as Figure 4.2).

For uncorrelated scatterers, the mobility depends inversely on the density of charged impurities, $1/\mu \sim n_{imp}$, and equations (4.1) and (4.2) are identical. We assume n_{imp} varies linearly with dosing time t as potassium is added to the device. Figure 4.3 shows $1/\mu_e$ and $1/\mu_h$ versus t , which are linear, in agreement with $1/\mu \sim n_{imp}$, hence verifying that equation (4.1) describes charged-impurity scattering in graphene. We

estimate the dosing rate $dn_{imp}/dt = (2.6-3.2) \times 10^{15} m^{-2} s^{-1}$ and the maximum concentration of $(1.4-1.8) \times 10^{-3}$ potassium per carbon (see the *Supplementary Information* section). From this point, we parameterize the data by $1/\mu_e$, proportional to the impurity concentration (the data set for e is more extensive than for h because of the limited V_g range accessible experimentally).

Figure 4.3, inset shows that, although the μ_e and μ_h are not identical, their ratio is fairly constant at $\mu_e/\mu_h = 0.83 \pm 0.01$ (see the *Methods* section). Novikov [73] predicted $\mu_e/\mu_h = 0.37$ for an impurity charge $Z = 1$; however, the asymmetry is expected to be reduced when screening by conduction electrons is included.

As K-dosing increases and mobility decreases, the linear behavior of $\sigma(V_g)$ (Fig. 4.2) associated with charged-impurity scattering dominates, as predicted theoretically [22]. At the lowest K-dosing level, sub-linear behavior is observed for large $|V_g - V_{g,min}|$ as anticipated. The dependence of the conductivity on carrier density $n \sim |V_g - V_{g,min}|$ is expected to be $\sigma \sim n^a$ with $a = 1$ for charged impurities and $a < 1$ for short-range and ripple scattering (see the *Supplementary Information* section). Adding conductivities in inverse according to Matthiessen's rule indicates that scattering other than by charged impurities will dominate at large n , with the crossover occurring at larger n as n_{imp} is increased [22]. A previous study [29] also found more linear $\sigma(V_g)$ for devices with lower mobility. Thus, our data indicate that the variation in observed field-effect mobilities of graphene devices is determined by the level of unintentional charged impurities.

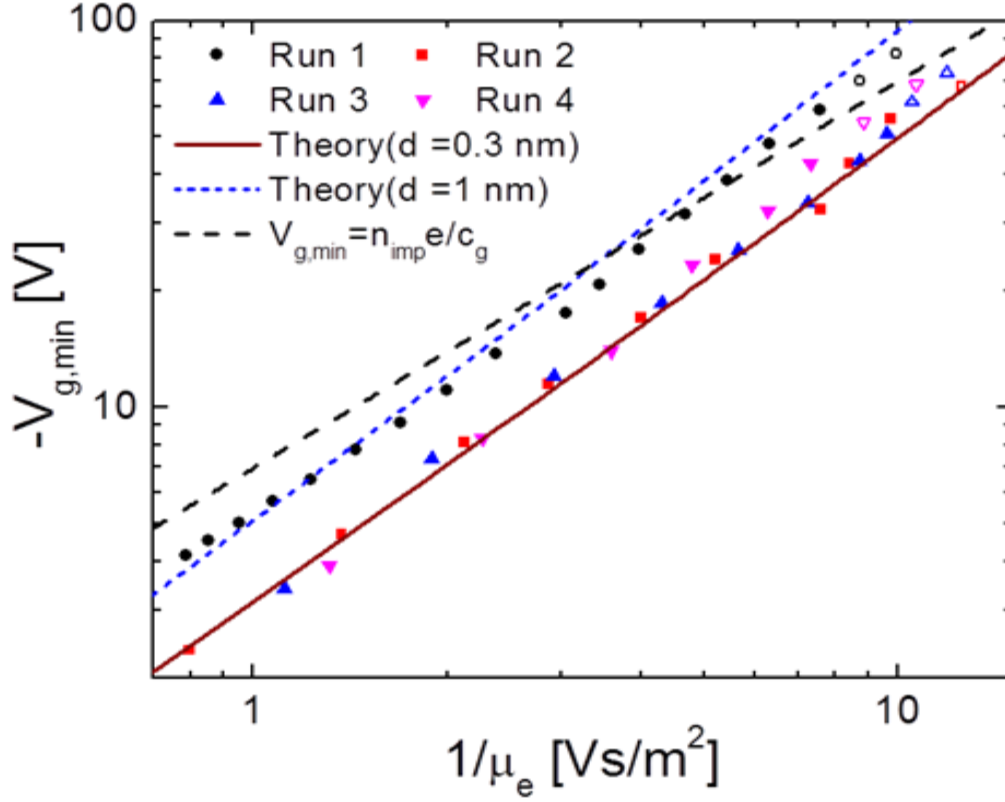


Figure 4.4 Shift of minimum conductivity point with doping.

The gate voltage of minimum conductivity $V_{g,min}$ is shown as a function of inverse mobility, which is proportional to the impurity concentration. All four experimental runs are shown. Each data set has been shifted by a constant offset in $V_{g,min}$ in order to make $V_{g,min}(1/\mu_e \rightarrow 0) = 0$, to account for any rigid threshold shift. The offset (in volts) is -10, 3.1, 5.6, and 8.2 for the four runs, respectively, with the variation likely to be due to accumulation of K in the SiO₂ on successive experiments. The open dots are $V_{g,min}$ obtained directly from the $\sigma(V_g)$ curves rather than fits to equation (4.1) because the linear regime of the hole side of these curves is not accessible due to heavy doping. The solid and short-dashed lines are from the theory of Adam et al. [25] for an impurity-graphene distance $d = 0.3$ nm (solid line) and $d = 1$ nm (short-dashed line), and approximately follow power laws with slopes 1.2 and 1.3, respectively. The long-dashed line shows the linear relationship $\Delta V_{g,min} = n_{imp} Z e / c_g$, where $n_{imp} = (5 \times 10^1 \text{ V}^{-1} \text{ s}^{-1}) / \mu$ and $Z = 1$.

We now examine the shift of the curves in V_g . Figure 4.4 shows $V_{g,min}$ as a function of $1/\mu_e$. Run 1 differs from runs 2–4, presumably owing to irreversible changes as potassium reacts with charge traps on silicon oxide and/or edges and defects of the graphene sheet. After run 1, subsequent runs are very repeatable, other than an increasing rigid shift to more negative voltage in the initial gate voltage of minimum conductivity. (The same distinction between first and subsequent experiments is seen in Fig. 4.5 as well.) It might be expected that the minimum conductivity would occur at the induced carrier density that precisely neutralizes the charged-impurity density: $n = -Zn_{imp}$ or $\Delta V_{g,min} = -n_{imp}Ze/c_g$ [80], where e is the elementary charge and Ze is the charge of the potassium ion. This prediction is shown as the long-dashed line in Fig. 4.4; the experimental data show a distinctly different effective power-law dependence. Adam *et al.* [25] proposed that the minimum conductivity in fact occurs at the added carrier density at which the average impurity potential is zero, $\Delta V_{g,min} = -ne/c_g$, where n is a function of n_{imp} , the impurity spacing d from the graphene plane and the dielectric constant of the SiO_2 substrate. The theory also assumes that $Z = 1$; experimentally, a reasonable evaluation [82] of Z for dilute potassium on graphite is ~ 0.7 . The theoretical lines in Fig. 4.4 are given by the exact result of Adam *et al.* [25], and follow an approximate power-law behavior of $\Delta V_{g,min} \sim n_{imp}^b$ with $b = 1.2 - 1.3$, which agrees well with experiment. The only adjustable parameter is the impurity–graphene distance d ; we show the results for $d = 0.3$ nm (a reasonable value for the distance of potassium on graphene [82-84]) and $d = 1.0$ nm (the value used by Adam *et al.*). As $\Delta V_{g,min}$ gives an independent estimate of

n_{imp} , the quantitative agreement in Fig. 4.4 verifies that $C = 5 \times 10^{15} \text{ V}^{-1} \text{ s}^{-1}$ in equation (4.1), as expected theoretically

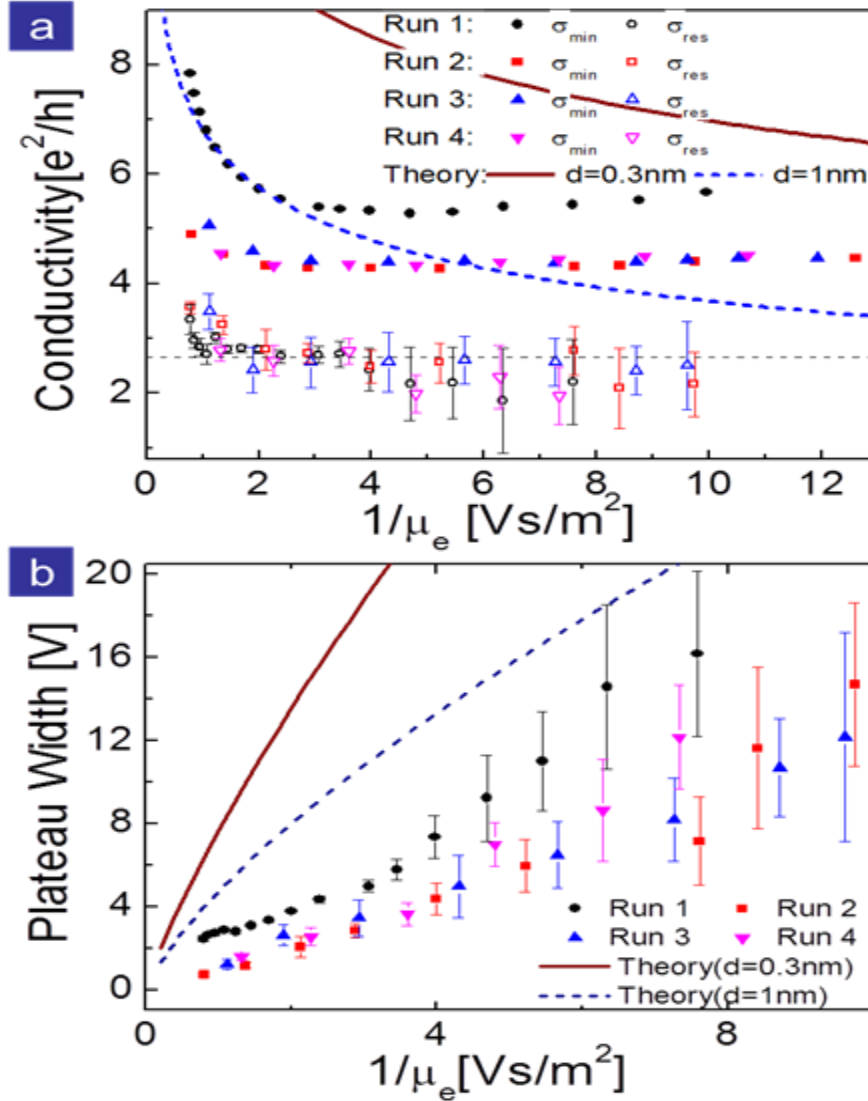


Figure 4.5 Change in behavior near minimum conductivity point with doping. (a) The minimum conductivity and the residual conductivity (defined in text) as a function of $1/\mu_e$ (proportional to the impurity density). (b) The plateau width ΔV_g as a function of $1/\mu_e$. In a and b, data from all four experimental runs are shown, as well as the theoretical predictions of the minimum conductivity and plateau width from Adam et al.[25] for $d = 0.3 \text{ nm}$ (solid line) and $d = 1 \text{ nm}$ (short-dashed line). Error bars represent experimental error in determining σ_{res} and ΔV_g from the fitting procedure (see *Methods*); σ_{min} is measured directly

We now turn to the behavior near the point of minimum conductivity. Figure 4.5 (a) shows the minimum conductivity σ_{min} and residual conductivity σ_{res} as a function of $1/\mu_e$, and Fig. 4.5 (b) shows the plateau width ΔV_g as a function of $1/\mu_e$; ΔV_g is the difference between the two values of V_g for which $\sigma_{min} = \sigma(V_g)$ in equation (4.2). The predictions from the theory of Adam *et al.* [25] for σ_{min} and ΔV_g are also shown. The minimum conductivity drops on initial potassium dosing, and shows a broad minimum near $4e^2/h$ before gradually increasing with further exposure. Notably, the cleanest samples show σ_{min} significantly greater than $4e^2/h$, and strongly dependent on charged-impurity density, indicating that the universal behavior [77,78] of σ_{min} associated with the Dirac point is not observed even in the cleanest samples. The irreversible change in the value of σ_{min} between run 1 and runs 2–4 is larger than the entire variation within runs 2–4. This difference between initial and subsequent runs indicates that the initial K-dosing and anneal cycle introduces other types of disorder (possibly short-range scatterers induced by irreversible chemisorption of potassium on defects or reaction of potassium with adsorbates) that have a comparable or greater impact on σ_{min} than charged impurities. That, for some disorder conditions (run 1), σ_{min} varies significantly with n_{imp} , but for other conditions (runs 2–4), the decrease in σ_{min} saturates rapidly with increasing n_{imp} , and is nearly constant for a very broad range of doping, suggests that the substantial variations reported in the literature (some groups report that σ_{min} is a universal value [17], whereas other groups observe variation in σ_{min} from sample to sample [29]) are probably due to poor control of the chemical environment of the devices measured. The observed residual conductivity σ_{res} is finite and surprisingly constant (Fig. 4.5 (a)); it is only weakly

dependent on doping, and shows little variation between the first run and subsequent runs. Finite σ_{res} has been predicted theoretically [74,75] for graphene with charged impurities; however, the magnitude has not been calculated. The change of ΔV_g with doping (Fig. 4.5 (b)) agrees only qualitatively with the theory, which predicts larger values and a sublinear dependence on doping. However, the quantitative disagreements between experiment and theory in Fig. 4.5 (a),(b) are connected: mobility, minimum conductivity and residual conductivity determine ΔV_g .

In summary, the dependence of conductivity of graphene on the density of charged impurities has been demonstrated by controlled potassium doping of clean-graphene devices in UHV at low temperature. The minimum conductivity depends systematically on charged-impurity density, decreasing on initial doping, and reaching a minimum near $4e^2/h$ only for non-zero charged-impurity density, indicating that the universal conductivity at the Dirac point [17,77,78] has not yet been probed experimentally. The high-carrier-density conductivity is quantitatively consistent with theoretical predictions for charged-impurity scattering in graphene [18,19,21,22,25,73-75]. The addition of charged impurities produces a more linear σ (V_g), and reduces the mobility, with the constant $C = \mu n_{imp} = 5 \times 10^{15} \text{ V}^{-1} \text{ s}^{-1}$, in excellent agreement with theory. The asymmetry for repulsive versus attractive scattering predicted for massless Dirac quasiparticles [73] is observed for the first time. Finally, the minimum conductivity point [25] occurs at the applied gate voltage at which the average impurity potential is zero and not at the voltage at which the gate-induced carrier density neutralizes the impurity charge.

Other observations indicate the need for fuller experimental and theoretical understanding. The irreversible changes in the behavior around $V_{g,min}$ between the first and subsequent doping runs indicate that the precise value of the minimum conductivity depends on the interplay of more than one type of disorder, and hence cannot be explained by existing theories [18,21,22,25,32,70,72,74,75]. An interesting new feature, the residual conductivity, may point to physics beyond the simple Boltzmann transport picture [74,75]. Further experiments including introducing short-range (neutral) scatterers to graphene will be useful in addressing these questions. Full understanding may require scanned-probe studies of graphene under well-controlled environmental conditions [66], which can completely characterize the disorder due to defects, charged and neutral adsorbates and ripples, as well as probe the electron scattering from each [85].

4.1 Methods

Fabrication of graphene devices and *in situ* transport measurements in UHV are described in chapter 3. Experiments are carried out at pressures lower than 5×10^{-10} torr and device temperature $T = 20$ K. Potassium doping is accomplished by passing a current of 6.5 A through a getter (SAES Getters) for 40 s before the shutter is opened for 2 s. The getter temperature during each potassium dosage was 763 ± 5 K as measured by optical pyrometry. The stability of the potassium flux was monitored by a residual gas analyzer positioned off-axis and behind the sample (see the *Supplementary Information* section). All measurements were carried out on one four-

probe device shown in Fig. 4.1 (a), although several two-probe devices showed similar behavior.

Conductivity σ is determined from the measured four-probe sample resistance R using $\sigma = (L/W)(1/R)$. Because the sample is not an ideal Hall bar, there is some uncertainty in the (constant) geometrical factor L/W . We estimate $L/W = 0.80 \pm 0.09$, where the error bars represent \pm one standard deviation. This 11% uncertainty in L/W translates into an 11% uncertainty in the vertical axes of Figs 4.2 and 4.3, the horizontal axes of Figs 4.4 and 4.5 (b) and both axes of Fig. 4.5 (a). Such scale changes are comparable to the spread among different experimental runs, and do not alter our conclusions. Notably, the uncertainty represents a systematic error, so relative changes in, for example, the minimum conductivity with charged-impurity density are still correct.

Best fits to equation (4.1) were determined using a least-squares linear fit to the steepest regime in the $\sigma(V_g)$ curves. The steepest regime of the $\sigma(V_g)$ curves was determined by examining $d\sigma/dV_g$; the fit was carried out over a 2 V interval in V_g around the maximum of $d\sigma/dV_g$. Other criteria for determining the maximum field-effect mobility give similar results. The experimental errors in μ_e and μ_h are determined by the fitting procedure described above; the errors in $V_{g,min}$, σ_{res} , ΔV_g (plateau width) and μ_e/μ_h are then calculated using equation (4.1) and standard error propagation. The errors (standard deviation) in μ_e , μ_h and $V_{g,min}$ were typically less than 4% . σ_{min} is measured directly, and has less than 1% error. Error bars (\pm one standard deviation) are shown in Fig. 4.3, inset for the errors in μ_e/μ_h , and in Fig. 4.5

for the errors in σ_{res} and ΔV_g . The weighted mean of μ_e/μ_h at non-zero dosing time is 0.83 and the weighted standard deviation of the mean is 0.01.

4.2 Supplementary Information

4.2.1 Theoretical predictions for charged impurity scattering in graphene

We briefly review the state of theoretical and experimental work on zero magnetic-field charge transport in graphene to place this work in context. Early theoretical work [77,78] on massless Dirac fermions using the Kubo formalism showed that the conductivity at the Dirac point for vanishing disorder is $4e^2/\pi h$. The minimum conductivity on order $4e^2/\pi h$ in graphene in the absence of disorder has been verified by others using the Kubo [28] and Landauer formalisms [28,86]. The addition of point scatterers gives a finite conductivity at finite carrier density which is *independent* of carrier density [14]. Attempts [21,70] to extrapolate between the high- and zero-density limits of scattering from short-range disorder have given a square-root dependence of conductivity on density, in contradiction with the experimentally-observed linear dependence.

Several groups [18,19,21,22,25] found charged impurity scattering in graphene to produce a conductivity linear in charge density and inversely proportional to impurity density, i.e.

$$\sigma(n) = Ce \left| \frac{n}{n_{imp}} \right|, \quad (4.2.1)$$

This is equivalent to a constant mobility inversely proportional to charged impurity

density $\mu = C/n_{imp}$. The constant C was determined to be on order $10^{16} \text{ V}^{-1} \text{ s}^{-1}$ [18,19,21,22,25], depending on the approximation used to calculate the screened Coulomb potential. Hwang, *et al.*[22] calculated the screened Coulomb potential within the random phase approximation, giving the most precise estimate of $C = 5 \times 10^{15} \text{ V}^{-1} \text{ s}^{-1}$.

The minimum conductivity for graphene with charged impurity scatterers has been treated theoretically by several groups. Numerical calculations [21,22] showed a finite conductivity of order $4e^2/h$ at zero charge density, which persisted over a plateau width roughly determined by the impurity density, and Adam, *et al.* [25] calculated the plateau width analytically. Adam, *et al.* also found analytically the dependence of minimum conductivity on density, and calculated the density at which the minimum conductivity occurs, adapting the theory of semiconductor band tails [87] to this problem. The minimum conductivity problem was also treated by Cheianov, *et al.* [88]; the results are qualitatively consistent with Adam, *et al.*, but they made no quantitative prediction of its magnitude or dependence on charged impurity density.

Recent work either extending Boltzmann transport theory to include electron-hole correlations [74] or using the current-current correlation function to calculate the Conductivity [75] has suggested Eqn. (4.2.1) may be modified to

$$\sigma(n) = Ce \left| \frac{n}{n_{imp}} \right| + \sigma_{res}, \quad (4.2.2)$$

which leaves the field-effect mobility independent of density, but does modify the minimal conductivity. Trushin and Schliemann [74] made no prediction for the

magnitude of σ_{res} , while Yan, *et al.* [75] found a residual conductivity $\sigma_{res} = 0.9e^2/h$ for a particular impurity density $n_{imp} = 7.8 \times 10^{11} \text{ cm}^{-2}$. However, both works exclude the charge inhomogeneity caused by the random Coulomb potential, so it is not clear how to determine the minimum or residual conductivities in the presence of this inhomogeneity.

Novikov [73] extended the semi-classical approach beyond the Born approximation, and found that charged impurity scattering obeys Eqn. (4.2.1), but C is dependent on the relative sign of carrier and impurity; C is still of order $10^{15} \text{ V}^{-1} \text{ s}^{-1}$, but the electron-hole asymmetry in C is expected to be a factor of 0.37 for graphene on SiO_2 in the absence of screening by conduction electrons. Including screening will reduce this value, and our experimental value 0.83 is very reasonable. Importantly, the asymmetry is only found for scattering by charged impurities, and not for scattering by ripples (see below); furthermore the asymmetry is associated with massless Dirac quasiparticles, and is not observed for massive quasiparticles in conventional materials. Thus, the observation of this asymmetry is definitive evidence that we are observing charged impurity scattering of massless Dirac particles.

Katsnelson and Geim [72] point out that *in addition* to charged impurity scattering, scattering by ripples could produce the behavior in Eqn. (4.2.1); in general ripples with height-height correlation function given by $\langle [h(r) - h(0)]^2 \rangle \propto r^{2H}$ produce

a conductivity in the form $\sigma(n) = Ce \left(\frac{n}{n_{imp}} \right)^{2H-1}$, which is equivalent to Eqn. (4.2.1)

for $2H = 2$. However, the experimentally measured exponent for the height-height

correlation function of graphene on SiO₂ is $2H = 1.1$ [66]; notably, this result was measured for samples fabricated in the same laboratory as the present work. This indicates that for graphene on amorphous SiO₂, ripples are more likely to have an effect similar to short-range disorder ($\sigma \sim \text{constant}$) rather than charged impurity disorder ($\sigma \sim n$).

4.2.2 Experimental studies of transport in graphene

Experimentally, the conductivity of graphene on SiO₂ is observed by several groups to be linear in density [6,17]. Tan, *et al.* [29] have reported the most extensive data on the range of behaviors observed for graphene on SiO₂, and noted a correlation between lower mobility, larger threshold shift, and broader minimum conductivity region. Their result is consistent with the theory of charged impurity scattering, though they could not correlate the observations with an independent measure of charged impurity density, and presumably the experiments could also be understood considering ripple scattering with $2H = 2$.

Schedin, *et al.* [80] studied the doping of graphene by molecular species at room temperature, but failed to observe any dependence of the mobility or minimum conductivity upon molecular doping (though they explored a much smaller range of $V_{g,\text{min}}$ shift than in the present work). They concluded that charged impurity scattering contributes negligibly to the mobility of graphene; calculating $C > 10^{17} \text{ V}^{-1}\text{s}^{-1}$, more than an order of magnitude larger than theoretical expectations and the experimental value found in this work. However, their experiments are confounded by the lack of UHV environment (especially the presence of adsorbed water), resist residue on the

sample (which may be responsible for the unexpected irreversible adsorption of gases at room temperature), and low initial sample mobility. Within the model of charged impurity scattering, the low initial mobility reported in Schedin, *et al.* together with the $V_{g,\min}$ near zero, indicates significant concentrations n_{imp}^+ and n_{imp}^- of positively and negatively charged impurities, respectively. While it cannot be determined which confounding factor prevented them from measuring the effects of charged impurity scattering, a reasonable explanation is that molecular doping may compensate some of the existing impurities [81]. Compensation results in an increase in net impurity charge $n_{imp}^+ - n_{imp}^-$, while reducing the absolute number of impurities $n_{imp}^+ + n_{imp}^-$ and *increasing* mobility. In principle a combination of compensation and addition of new impurities can cause any behavior in between, and can explain a shift in $V_{g,\min}$ absent a change in mobility.

4.2.3 Comparison of our work to theory

We identify six specific effects of charged impurity scattering on transport in graphene: (1) the mobility decreases with increasing n_{imp} , (2) the gate-voltage dependence of the conductivity $\sigma(V_g)$ becomes more linear with increasing n_{imp} , (3) for positive impurities, the mobility becomes larger for holes than electrons, (4) the gate voltage of minimum conductivity $V_{g,\min}$ shifts to more negative gate voltage with increasing n_{imp} , (5) the width of the minimum conductivity region in V_g broadens, (6) the minimum conductivity σ_{\min} decreases and then increases with increasing n_{imp} . In addition we observe a seventh effect (7); we observe a residual conductivity σ_{res} (defined in Eqn. 4.1) which is roughly independent of n_{imp} . Of these, effects (1) and (2)

are ubiquitously accepted by the theoretical community [18,19,21,22,25,73-75], and our results are in quantitative agreement in the magnitude of the constant C in Eqn. (4.2.1). Effect (3) was recently pointed out [89] as a property of Dirac fermions which is not observed for massive quasiparticles. Adam, *et al.* [25] give an analytical expression for effect (5), however this effect is anticipated by several other works [21,22,88]. Quantitative predictions for effects (4) and (6) have only been attempted by Adam [25], but (4) is in general expected, and follows directly from work on the problem of semiconductor band tails [87]. Effect (7) was unanticipated in early work on charged impurity scattering, but was recently found using two separate techniques [74,75] though there is no quantitative prediction for the residual conductivity as a function of impurity density.

Together, our results indicate good quantitative agreement with the theory of charged impurity scattering in the high-density regime. In particular, charged impurity scattering produces a constant field-effect mobility (linear $\sigma(V_g)$), with the mobility-impurity density product $C = 5 \times 10^{15} \text{ V}^{-1} \text{ s}^{-1}$. We also find that the gate voltage shift of the minimum conductivity point is accurately described taking into account the screened impurity potential, indicating the physics of the minimum conductivity point is governed by charge-carrier inhomogeneity produced by charged impurities. Near the minimum conductivity point, we find qualitative agreement with theory; the minimum conductivity decreases initially with addition of charged impurities, and the minimum conductivity region broadens. Our experimental observation of a residual conductivity at zero density and the non-monotonic dependence of the minimum conductivity on impurity density indicate that there still

remain subtle issues to be understood regarding the minimum conductivity in graphene.

Experimentally, we tune only the density of charged impurities, so we can only make comparisons to the theory of charged impurity scattering. However, we can argue that other contributions to scattering in graphene at low temperature are small, at least in the samples presently available, for the following reasons. First, the linear behavior which is characteristic of charged impurity scattering is observed over a wide range of impurity densities. The sublinear behavior observed at the lowest impurity density can be used to put a bound on any other contribution to the mobility; a contribution with a characteristic $\sigma(n) = \text{constant}$ (e.g. from point defects) could at most contribute to one-third of the resistivity at a carrier concentration of $3 \times 10^{12} \text{ cm}^{-2}$, or a mobility of $> 3 \text{ m}^2/\text{Vs}$ at that density (and higher at lower density; $\sigma(n) = \text{constant}$ implies $\mu \propto n^{-1}$). This is significantly higher than the mobility of the best samples at present, but future experiments on graphene with significantly lower charged impurity density may be able to probe this scattering contribution. Second, the linear conductivity behavior seen in all experimental samples to date is associated with only two types of scatterers: charged impurities, and ripples with a particular height-height correlation function exponent $2H = 2$. However, our experiments clearly show that the experimentally observed transport behaviors can quantitatively be described with reasonable charged impurity concentrations. The same is not true for ripples; there is no experimental evidence that ripples with the proper height-height correlation exponent or magnitude exist in graphene on SiO_2 . On the contrary,

graphene on SiO₂ exhibits a height-height correlation exponent $2H \approx 1$ [66], indicating ripples should have a similar effect to short-range disorder.

4.2.4 Effect of Impurity Charge $Z \neq 1$

The theoretical models used in the main text to compare with our experimental results assume that the valence of the potassium impurity atoms $Z = 1$, although experimental estimates give $Z \sim 0.7$ for potassium on graphite [82,90]. Following the experimental procedure where mobility μ is measured directly through the linear fit of conductivity with gate voltage, one can estimate, that to first order, allowing $Z \neq 1$ would change our estimates for the experimentally derived quantities as follows: $C \rightarrow C/Z^2$, $V_{g,\min} \rightarrow V_{g,\min}/Z^2$, while the minimum conductivity σ_{\min} and plateau width ΔV_g are unchanged to this level of approximation. Therefore, using $Z = 0.7$ instead of $Z = 1$ would change the theoretical predictions for some quantities by a factor of ~ 2 . We feel that this is not a significant correction, since we do not expect the accuracy of the theory when compared to experiment to be better than a factor of 2, and moreover, the precise value of Z for potassium on graphene is unknown.

4.2.5 Determination of Potassium Dosing Rate

We use the fact that the product of mobility and impurity concentration is a constant, $\mu n_{\text{imp}} = C$, where $C = 5 \times 10^{15} \text{ V}^{-1} \text{ s}^{-1}$, with the linear fits in figure 4.3 of the main text to obtain the dosing rate $dn_{\text{imp}}/dt = (2.6 \sim 3.2) \times 10^{15} \text{ m}^{-2} \text{ s}^{-1}$. The value corresponds to a maximum concentration of $(1.4 \sim 1.8) \times 10^{-3}$ potassium atoms per carbon atom for the largest dosing time (18s) used.

The dosing rate was also estimated from residual gas analysis of the K flux during evaporation. Correcting for the geometry factor, the RGA-reported K-pressure would correspond to a flux of approximately $5 \times 10^{14} \text{ m}^{-2} \text{ s}^{-1}$ at the sample. Since the RGA has not been calibrated for potassium, the value cannot be used quantitatively, but does confirm the order of magnitude of the deposition rate.

Chapter 5 : Tuning the effective fine structure constant in graphene ; opposing effects of dielectric screening on short- and long-range potential scattering ²

Abstract : We reduce the dimensionless interaction strength α in graphene by adding a water overlayer in ultrahigh vacuum, thereby increasing dielectric screening. The mobility limited by long-range impurity scattering is increased over 30%, due to the background dielectric constant enhancement leading to a reduced interaction of electrons with charged impurities. However, the carrier-density-independent conductivity due to short-range impurities is decreased by almost 40%, due to reduced screening of the impurity potential by conduction electrons. The minimum conductivity is nearly unchanged, due to canceling contributions from the electron-hole puddle density and long-range impurity mobility. Experimental data are compared with theoretical predictions with excellent agreement.

² This chapter was adapted from: C. Jang, S. Adam, J.-H. Chen, E.D. Williams, S. Das Sarma, and M.S. Fuhrer, *Phys. Rev. Lett.* **101**, 146805 (2008)

Most theoretical and experimental work on graphene has focused on its gapless, linear electronic energy dispersion $E = \hbar v_F k$. One important consequence of this linear spectrum is that the dimensionless coupling constant α (or equivalently r_s , defined here as the ratio between the graphene Coulomb potential energy and kinetic energy) is a carrier-density independent constant [20,91], and as a result, the Coulomb potential of charged impurities in graphene is renormalized by screening, but strictly maintains its long-range character. Thus there is a clear dichotomy between long-range and short-range scattering in graphene, with the former giving rise to a conductivity linear [20,22] in carrier density (constant mobility), and the latter having a constant conductivity independent of carrier density. Charged impurity scattering necessarily dominates at low carrier density, and the minimum conductivity at charge neutrality is determined by the charged impurity scattering and the self-consistent electron and hole puddles of the screened impurity potential[12,22,25,29] .

Apart from the linear spectrum, an additional striking aspect of graphene, setting it apart from all other two-dimensional electron systems, is that the electrons are confined to a plane of atomic thickness. This fact has a number of ramifications which are only beginning to be explored [92]. One such consequence is that graphene's properties may be tuned enormously by changing the surrounding environment. Here we provide a clear demonstration of this by reducing the dimensionless coupling constant α in graphene by more than 30 percent through the addition of a dielectric layer (ice) on top of the graphene sheet. Upon addition of the ice layer, the mobility limited by long-range scattering by charged impurities increases by 31 percent, while the conductivity limited by short-range scatterers

decreases by 38 percent. The minimum conductivity value remains nearly unchanged. The opposing effects of reducing α on short-and long-range scattering are easily understood theoretically. The major effect on long-range scattering is to reduce the Coulomb interaction of electrons with charged impurities, reducing the scattering [93]. In contrast, the dielectric does not modify the atomic-scale potential of short-range scatterers, and there the leading effect is the reduction of screening by the charge carriers, which increases scattering resulting in lower high-density conductivity. Such screening of short-range potentials has been predicted theoretically [2,94], although in other 2D systems, this effect is difficult to observe experimentally. The minimum conductivity is nearly unchanged due to competing effects of increased mobility and reduced carrier concentration in electron-hole puddles due to reduced screening [25,30].

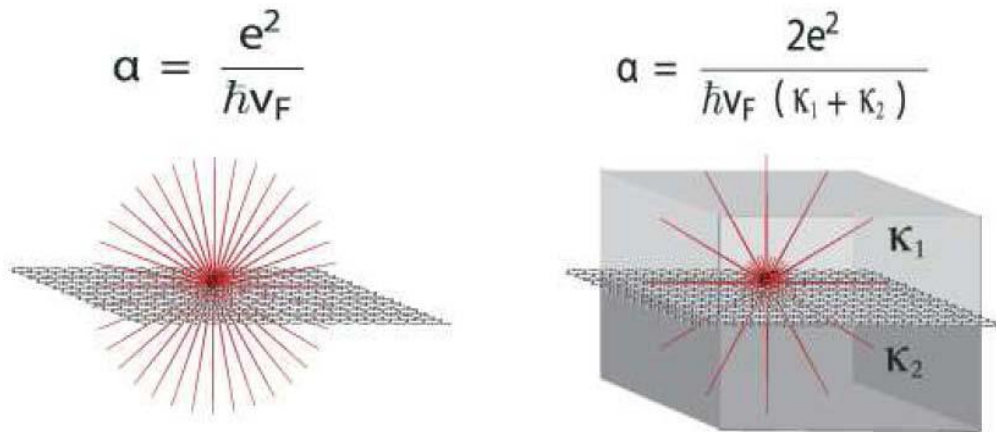


Figure 5.1 Schematic illustrating dielectric screening in graphene. The dielectric environment controls in the interaction strength parameterized by the coupling constant α .

Figure 5.1 illustrates the effect of the dielectric environment on graphene. For graphene sandwiched between two dielectric slabs with κ_1 and κ_2 ,

$$\alpha = \frac{2e^2}{(\kappa_1 + \kappa_2)\hbar v_F} \quad (5.1)$$

,where e is the electronic charge, \hbar is Planck's constant, and v_F is the Fermi velocity, which we take to be $1.1 \times 10^6 \text{ ms}^{-1}$ [16,17,95]. Typically, graphene transport experiments [12,16,17,29] are performed on a SiO_2 substrate with $\kappa_1 \approx 3.9$ and in air/vacuum $\kappa_2 \approx 1$, making graphene a weakly interacting electron system with $\alpha \approx 0.8$ (although very recently work on substrate-free graphene [96] explored the strong coupling regime with $\alpha \approx 2$). Here we deposit ice ($\kappa_2 \approx 3.2$ [97]) on graphene on SiO_2 , decreasing α from ≈ 0.81 to ≈ 0.56 .

Graphene is obtained by mechanical exfoliation of Kish graphite on a SiO_2 (300 nm)/Si substrate [17]. The heavily n-doped silicon substrate is used as a back gate. Graphene monolayers are identified from the color contrast in an optical microscope image and confirmed by Raman spectroscopy [64]. The final device (see Figure 5.2 inset) was fabricated by patterning electrodes using electron beam lithography and thermally evaporated Cr/Au, followed by annealing in Ar/ H_2 to remove resist residue (see chapter 3 for details). The experiments are performed in a cryostat cold finger placed in an ultra high vacuum (UHV) chamber. In order to remove residual adsorbed gases on the device and the substrate, the sample was baked at 430 K overnight in UHV following a vacuum bakeout. The conductivity was

measured using a conventional four-probe technique with an ac current of 50 nA at a base pressure ($\sim 10^{-10}$ torr) and device temperature (~ 77 K). Deionized nanopure water was introduced through a leak valve attached to the chamber. The water gas pressure (determined by a residual gas analyzer) was $5 \pm 3 \times 10^{-8}$ torr. The amount of ice deposited was estimated by assuming a sticking coefficient of unity and the ice I_h layer density of $9.54 \times 10^{14} \text{ cm}^{-2}$ [98,99].

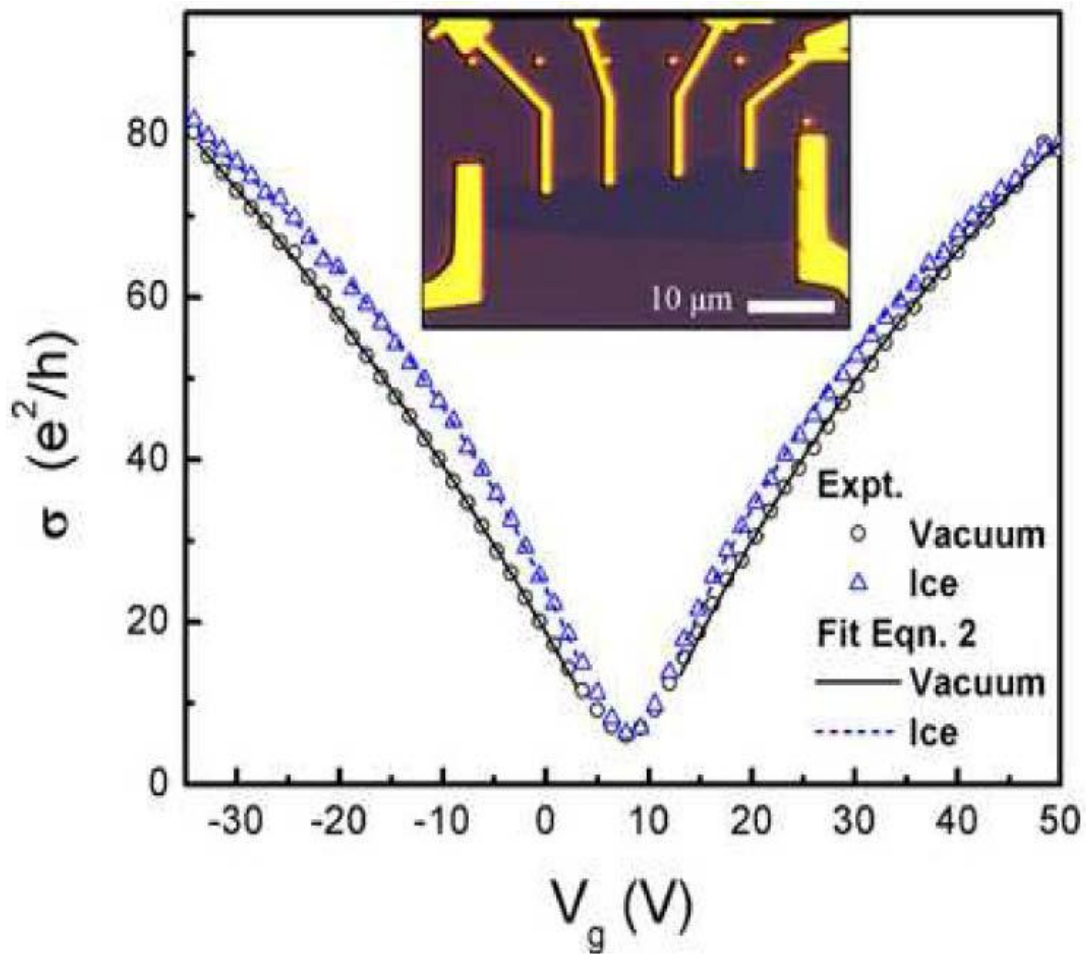


Figure 5.2 Conductivity of the graphene device as a function of back-gate voltage for pristine graphene (circles) and after deposition of 6 monolayers of ice (triangles). Lines are fits to Eq.(5.2). Inset: Optical microscope image of the device.

Figure 5.2 shows conductivity as a function of gate voltage for two different sample conditions, pristine graphene and ice-covered graphene. We observe several interesting effects of adding ice: (i) The offset gate voltage at which the conductivity is a minimum $V_{g,\min}$ remains unchanged; (ii) the minimum conductivity σ_{\min} value remains unchanged, (iii) the maximum slope of $\sigma(V_g)$ becomes steeper, and (iv) the curve $\sigma(V_g)$ in the presence of ice is more non-linear and crosses that of the pristine sample at some large carrier density. All these features can be understood qualitatively from the physical picture described above, and we show below that they are in quantitative agreement with the predictions of Boltzmann transport theory including screening within the Random Phase Approximation (RPA).

In order to interpret the experimental results quantitatively [100], we fit the conductivity data to

$$\sigma^{-1}(V_g, \alpha) = (ne\mu)^{-1} + \sigma_s^{-1} \quad (5.2)$$

,where $ne = c_g |V_g - V_{g,\min}|$, e is the electric charge and $c_g = 1.15 \times 10^{-8} \text{ V/cm}^2$ is the gate capacitance per unit area for the 300 nm thick SiO_2 . Since the transport curves are not symmetric about the minimum gate voltage, the fitting is performed separately for positive and negative carrier densities (i.e. electron and hole carriers), excluding data close to the Dirac point conductivity plateau ($V_{g,\min} \pm 5\text{V}$). We report both the symmetric μ_{sym} (σ_{sym}) and anti-symmetric μ_{asym} (σ_{asym}) contributions to the mobility (conductivity). Shown also in figure 5.2 is the result of the fit for pristine graphene and after deposition of 6 monolayers of ice.

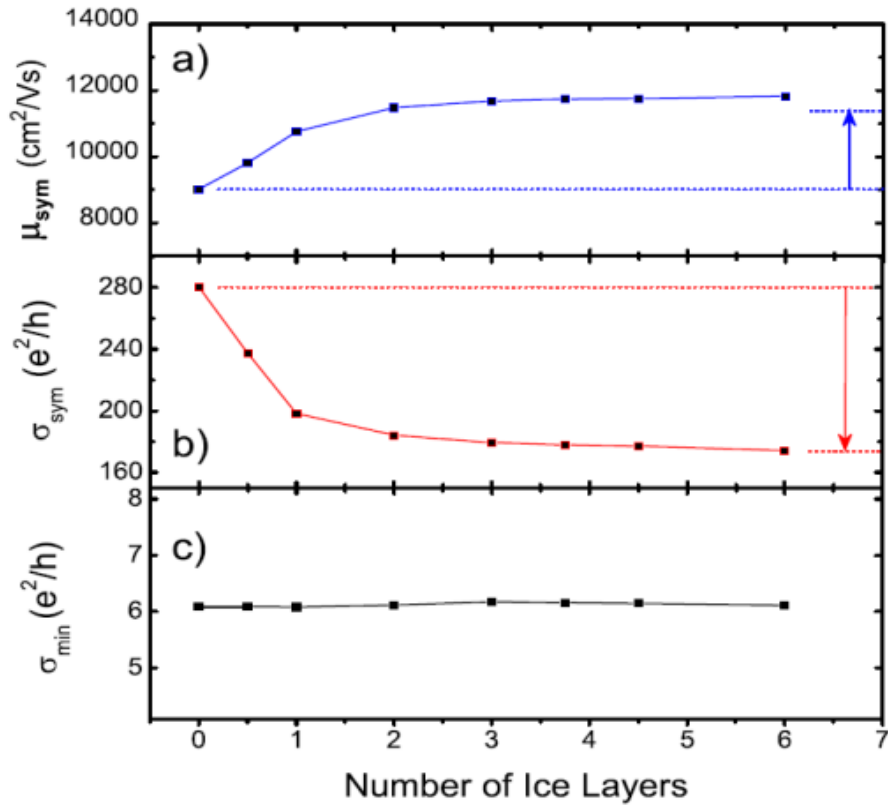


Figure 5.3 μ_{sym} , σ_{sym} and σ_{min} as a function of number of ice layers. Dashed lines show the values for pristine graphene and corresponding theoretical expectations for the ice-covered device.

Figure 5.3 shows μ_{sym} , σ_{sym} and σ_{min} as a function of number of ice layers. The mobility (Figure 5.3 (a)) of pristine graphene is $9,000 \text{ cm}^2\text{V}^{-1}\text{s}^{-1}$, which is typical for clean graphene devices on SiO_2 substrates at low temperature. As the number of water layers increases, the mobility increases, and saturates after about 3 layers of ice to about $12,000 \text{ cm}^2\text{V}^{-1}\text{s}^{-1}$. In contrast, the conductivity due to short-range scatterers (Figure 5.3 (b)) decreases from $280 e^2/h$ to $170 e^2/h$. The decrease in conductivity due to short-range scatterers shows a similar saturation behavior as the mobility,

suggesting they have the same origin³. The absence of any sharp change in the conductivity or mobility at very low ice coverage rules out ice itself acting as a significant source of short- or long-range scattering. This is corroborated by the absence of a shift in the gate voltage of the minimum conductivity, consistent with physisorbed ice [98] not donating charge to graphene [12,25,29]. Figure 5.3 (c) shows that the minimum conductivity is essentially unchanged during the addition of ice.

We now analyze the experimental results within Boltzmann transport theory. The conductivity of graphene depends strongly on the coupling constant α . For screened long-range impurities within RPA, we have [25]

$$\sigma_l = \frac{2e^2}{h} \frac{n}{n_{imp}} \frac{1}{F_l(\alpha)}, \quad (5.3)$$

$$F_l(\alpha) = \pi\alpha^2 + 24\alpha^3(1 - \pi\alpha) + \frac{16\alpha^3(6\alpha^2 - 1)\arccos[1/2\alpha]}{\sqrt{4\alpha^2 - 1}},$$

where in the last term, for $\alpha < 0.5$ both $\arccos[1/2\alpha]$ in the numerator and $\sqrt{4\alpha^2 - 1}$ in the denominator are purely imaginary so that $F_l(\alpha)$ is real and positive for all α . For screened short-range impurities, we have [27]

³ The saturation behavior shown in Fig. 5.3 indicates that the ice film is continuous well before the formation of 6 full ice layers, and has reached a constant value of the dielectric constant. Bulk dielectric constant has been observed in ultrathin films of SiO₂, see K. Hirose et al., Phys. Rev. B **67**, 195313 (2003), and it is reasonable to assume that these ultrathin ice layers have the bulk dielectric constant of ice.

$$\sigma_s = \frac{\sigma_0}{F_s(\alpha)},$$

$$F_s(\alpha) = \frac{\pi}{2} - \frac{32\alpha}{3} + 24\pi\alpha^2 + 320\alpha^3(1 - \pi\alpha) \quad (5.4)$$

$$+ 256\alpha^3(5\alpha^2 - 1) \frac{\arccos[1/2\alpha]}{\sqrt{4\alpha^2 - 1}},$$

where similarly $F_s(\alpha)$ is real and positive. Consistent with the physical picture outlined earlier, in the limit $\alpha \rightarrow 0$, $\sigma_1 \sim \alpha^{-2}$ which describes the scaling of the Coulomb scattering matrix element, while for short-range scattering, $\sigma_s \approx \text{const} (1 + (64/3\pi)\alpha)$ where increased screening of the potential by the carriers gives the leading order increase in conductivity. For the experimental values of α , the full functional form of F_s and F_1 should be used⁴. Dashed lines in Figures 5.3 (a)-(b) show the theoretical expectations for μ_{sym} and σ_{sym} for vacuum and ice on graphene in quantitative agreement with experiment.

Regarding the magnitude of the minimum conductivity, it was recently proposed [25] that one can estimate σ_{min} by computing the Boltzmann conductivity of the residual density n^* that is induced by the charged impurities. This residual density (i.e. rms density of electrons and hole puddles) has been seen directly in scanning

⁴ Results beyond the RPA approximation have been examined in A. V. Shytov et al., Phys. Rev. Lett. 99, 236801 (2007), R. R. Biswas et al., Phys. Rev. B 76, 205122 (2007), V. M. Pereira et al., Phys. Rev. Lett. 99, 166802 (2007), I. S. Terekhov et al., Phys. Rev. Lett. 100, 076803 (2008), M. S. Foster et al. Phys. Rev. B 77, 195413 (2008) and M. Mueller et al., arXiv:0805.1413v1 (2008). We believe that these effects are unobservable in the current experiment. Also M. Trushin et al. Europhys. Lett. 83, 17001 (2008) consider a phenomenological Yukawa potential. Generally one uses a model Yukawa potential in studying systems where the microscopic nature of the screened potential is unknown which is not the case for graphene. For the Yukawa potential, we find $F_y = \pi\alpha^2 + 8\alpha^3 - \pi\alpha(1 + 4\alpha^2)^{0.5}$ which is qualitatively similar to Eq. 5.3.

probe experiments [101] and in numerical simulations [30]. We therefore use Eq.(5.3), but replace n with $n^* = \langle V_D^2 \rangle / [\pi(\hbar v_F)^2]$ (where the angular brackets indicate ensemble averaging over configurations of the disorder potential V_D) to give [25]

$$\sigma_{\min} = \frac{2e^2}{h} \frac{1}{F_1(\alpha)} \frac{n^*(\alpha)}{n_{\text{imp}}}, \quad (5.5)$$

$$\langle V_D^2 \rangle = n_{\text{imp}} (\hbar v_F \alpha)^2 \int dq \left(\frac{e^{-qd}}{q\epsilon(q)} \right)^2,$$

where $\epsilon(q)$ is the RPA dielectric function and $d \approx 1$ nm is the typical impurity separation from the graphene sheet. The dominant contribution to both the disorder potential $\langle V_D^2 \rangle$ and $F_1(\alpha)$ is the Coulomb matrix element, giving $n^* \sim n_{\text{imp}} \alpha^2$ and $1/F_1(\alpha) \sim 1/\alpha^2$ so that to leading order, σ_{\min} is unchanged by dielectric screening⁵.

⁵ Estimating the charged impurity density $n_{\text{imp}} \approx 5.5 \times 10^{10} \text{ cm}^{-2}$ (which is comparable to similar experiments Y.-W. Tan, Y. Zhang, K. Bolotin, *et al.*, *Measurement of Scattering Rate and Minimum Conductivity in Graphene*, Phys. Rev. Lett. **99**, 246803 (2007). J.-H. Chen, C. Jang, M. S. Fuhrer, *et al.*, *Charged Impurity Scattering in Graphene*, Nat. Phys. **4**, 377 (2008).) we find S. Adam, E. H. Hwang, V. M. Galitski, *et al.*, *A self-consistent theory for graphene transport*, Proc. Natl. Acad. Sci. USA **104**, 18392 (2007). $\sigma_{\min}(\text{ice}) = \sigma_{\min}(\text{vac}) \approx 6.66/6.72 \approx 0.99$. The minimum conductivity (Fig. 5.3 c) shows almost no variation with ice layers, in agreement with this theoretical expectation. We ignore quantum coherent effects such as localization (see e.g. I. Aleiner and K. Efetov, Phys. Rev. Lett. **97**, 236801 (2006)) which are not expected to be important at 77 K, and are not experimentally observed.

		<i>Theory</i>	<i>Experiments</i>
Long-range (symmetric): $\frac{\mu_{sym}^{ice}}{\mu_{sym}^{vac}} = \frac{F_l(\alpha^{vac})}{F_l(\alpha^{ice})}$	Ref [25]	1.26	1.31
Short-range (symmetric): $\frac{\sigma_{sym}^{ice}}{\sigma_{sym}^{vac}} = \frac{F_s(\alpha^{vac})}{F_s(\alpha^{ice})}$	Ref [27]	0.62	0.62
Minimum Conductivity: $\frac{\sigma_{min}^{ice}}{\sigma_{min}^{vac}} = \frac{n^*(\alpha^{ice})F_l(\alpha^{vac})}{n^*(\alpha^{vac})F_l(\alpha^{ice})}$	Ref [25]	0.99	1.00
Long-range (anti-symmetric): $\frac{\mu_{asym}^{ice}}{\mu_{asym}^{vac}} = \frac{F_l(\alpha^{vac})\alpha^{ice}}{F_l(\alpha^{ice})\alpha^{vac}}$	Ref [73]	0.87	0.17
Short-range (anti-symmetric): $\frac{\sigma_{asym}^{ice}}{\sigma_{asym}^{vac}}$	Ref [102]		0.13

Table 5.1 Summary of our results in corresponding theoretical predictions.

The experimental data also show a mobility asymmetry (between electrons and holes) of about 10 percent. Novikov [73] argued that for Coulomb impurities in

graphene such an asymmetry is expected since electrons are slightly repelled by the negative impurity centers compared to holes resulting in slightly higher mobility for electrons (since $V_{g,\min} > 0$, we determine that there are more negatively charged impurity centers, see also Ref. [12]); and that for unscreened Coulomb impurities $\mu_{\text{usc}}(\pm V_g) \sim [C_2 \alpha^2 \pm C_3 \alpha^3 + C_4 \alpha^4 + \dots]^{-1}$. From the magnitude of the asymmetry, we know that $C_3 \alpha^3 \ll C_2 \alpha^2$, but if we further assume that $C_4 \alpha^4 \ll C_3 \alpha^3$ (although, in the current experiment, we cannot extract the value of C_4), then including the effects of screening gives $\mu_{\text{asym}} \sim \alpha/F_1(\alpha)$.

In table 5.1 we show all the experimental fit parameters and compare them to theoretical predictions. The quantitative agreement for μ_{sym} , σ_{\min} and σ_{sym} is already highlighted in figure 5.3, while we have only qualitative agreement for μ_{asym} , probably because the condition $C_4 \alpha^4 \ll C_3 \alpha^3$ does not hold in our experiments. There is no theoretical expectation of asymmetry in σ_s ; the experimental asymmetry (about 30 percent) could be explained by contact resistance [102] which we estimate to be a 20 percent correction to σ_s for our sample geometry.

In conclusion we have observed the effect of dielectric environment on the transport properties of graphene. The experiment highlights the difference between long-range and short-range potential scattering in graphene. The enhanced μ_l (i.e. the slope of σ against density) and reduced σ_s (i.e. the constant conductivity at high density) are attributed to the decreased interaction between charged carriers and impurities and decreased screening by charge carriers, respectively, upon an increase in background dielectric constant with ice deposition in UHV. These variations quantitatively agree with theoretical expectations for the dependence of electron

scattering on graphene's "fine structure constant" within the RPA approximation. This detailed knowledge of the scattering mechanisms in graphene is essential for design of any useful graphene device, for example, use of a high- κ gate dielectric will increase the transconductance of graphene at the expense of linearity, an important consideration for analog applications. As demonstrated here, dielectric deposition only improved mobility by 30 %, however the use of high- κ dielectric overlayers could significantly enhance this result.

Chapter 6 : Magnetic Field induced insulator-quantum Hall conductor transition in disordered graphene

Abstract: We have studied the insulator-quantum Hall conductor (I-QH) transition in disordered graphene covered with cobalt (Co) clusters. A clear critical magnetic field, separating insulating and metallic behaviors, was identified in the magnetotransport measurements for different temperatures from 2 – 10 K at fixed carrier density. Scaling analysis indicates that the transition is a quantum phase transition. The critical scaling exponent varies with carrier density, which may indicate the new universality class of the I-QH transition in graphene.

The localization-delocalization, or insulator-quantum Hall effect (I-QHE), transition in a two-dimensional electron system (2DES) is of fundamental interest as an example of a quantum phase transition. Graphene offers a qualitatively new 2DES to study this transition, as graphene exhibits an unconventional half-integer QHE [16,17] due to the chiral nature of relativistic Dirac fermions in graphene, and a complex interplay of weak localization and weak anti-localization. Recent experimental results on plateau-plateau (PP) transitions [40] and metal (QH plateau) to insulator (at $N = 0$ Landau level (LL)) [40-42,103-112] (PI) transitions have identified these phenomena as quantum phase transitions under scaling theory. Though the main properties of the transitions are similar to the results for conventional two dimensional electron gases (2DEGs) with massive charge carriers, several aspects such as the universality classes of the transitions [42,62,63] and the origin of the insulating states near $N = 0$ LL [41,106,108] are still not conclusive.

Unlike the conventional 2DESs with massive fermions, the massless Dirac fermions of graphene cannot be strongly localized with long-wavelength disorder (e.g. charged impurities) because the carriers are able to pass through potential barriers (Klein tunneling). Only disorder which causes inter-valley scattering can restore the usual localization behavior and in principle induce strong localization in graphene [21,113-116]. Once strong localization is achieved, one might expect a delocalization transition (I-QHE transition) in graphene with increased magnetic field, similar to conventional 2DESs [47-51,117-120]. Indeed, in the phase diagram derived from numerical simulations based on the tight binding model of disordered graphene in magnetic field [39], not only the PP and PI transitions, but also the transitions from

the insulating state to QH states with any LL filling factors higher than 2 are possible as magnetic field increases. However, experimentally the I-QH transition induced by low magnetic field in graphene has not been reported yet, likely due to the difficulty of achieving suitably disordered samples. Although several groups recently have reported insulating behavior in graphene with inter-valley scatterers obtained by oxidation [114], hydrogenation [113,116] and fluorination [115], the transition from the insulating states to QH regime has not been reported.

In this chapter, we investigate the transition from insulator to QH liquid in graphene with inter-valley scattering induced by cobalt nanoparticle decoration. Scaling analysis of the temperature and magnetic field dependence of the resistivity near the transition indicates a zero-temperature transition, i.e. a quantum phase transition. The temperature critical exponent varies with carrier density (tuned via back gated voltage), which is possibly an indication of a change in the universality class of the I-QH transition in graphene due to a change in the dominant disorder type with carrier density.

A graphene field effect transistor device was fabricated and placed in a UHV chamber (as described in Chapter 3). Then 1 nm thick Co was deposited on the graphene device using an e-beam evaporator with a rate of 0.1 \AA/s in UHV at 14 K. Later the device was annealed at 400 K overnight in the chamber expecting to form Co clusters on graphene as reported in Ref. [121]. Finally the annealed sample was transferred (exposing to air) to another cryostat (Quantum Design Physical Property Measurements System, PPMS) and resistivity and Hall effect measurements for various temperatures and magnetic fields were performed using a conventional 4-

probe low frequency lock-in technique. After transfer and exposure to air, p-type doping of the sample was observed. The doping could be reduced by baking the sample at 100 °C overnight in PPMS before the measurements.

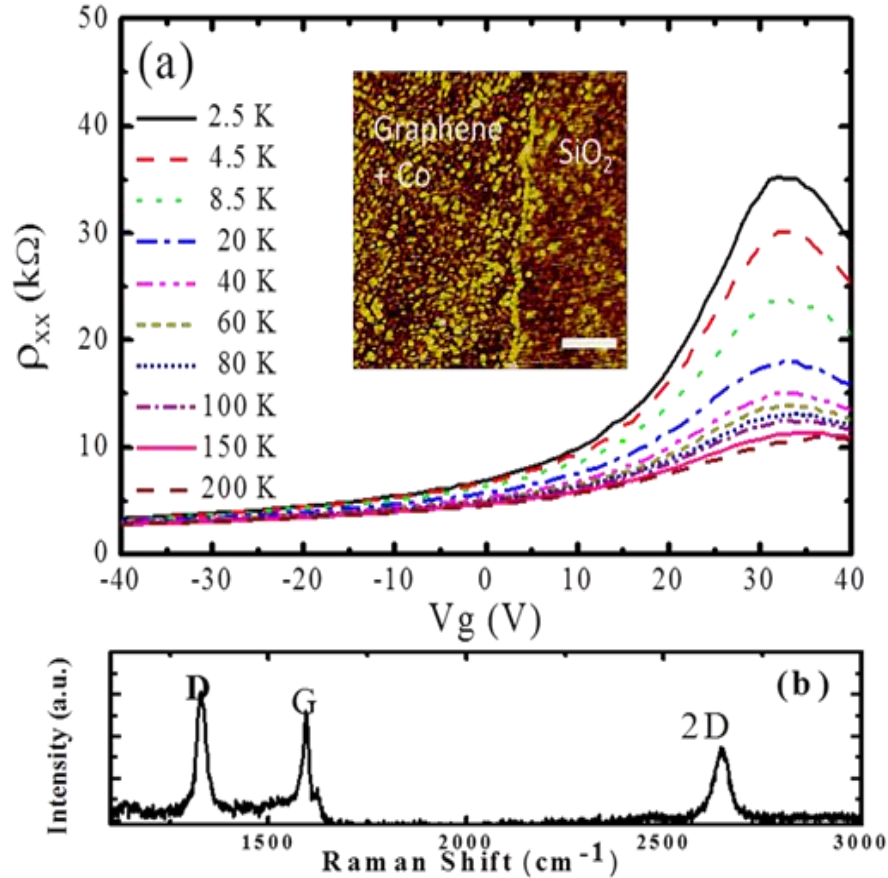


Figure 6.1 ρ_{xx} vs V_g for different temperatures, and Raman spectroscopy of the disordered device

(a) Longitudinal resistivity ρ_{xx} of cobalt-decorated graphene as a function of gate voltage for different temperatures from 2 – 200 K (as indicated in legend) and zero magnetic field. The inset shows an atomic force micrograph of the Co covered graphene on SiO_2 ; the left side is graphene, and the right side is bare SiO_2 substrate. The scale bar corresponds to 200 nm. (b) Raman spectroscopy of the Co covered graphene device.

Fig. 6.1 (a) shows the longitudinal resistivity ρ_{xx} as a function of gate voltage V_g for different temperatures T from 2 K to 200 K at zero magnetic field ($B = 0$). Surprisingly, the temperature dependence of the resistivity exhibits strong insulating behavior ($d\rho_{xx}/dT < 0$). Fig. 6.2 (a)-(b) shows the temperature dependences of the resistivity at different carrier densities. The carrier density is given by $n = c_g \Delta V_g / e$, where $c_g = 1.15 \times 10^{-8}$ F/cm² is the gate capacitance per unit area, e the elemental charge, and $\Delta V_g = |V_g - V_{g,CNP}|$ is the gate voltage measured relative to the gate voltage at charge neutrality, with $V_{g,CNP} = 33$ V for this sample. The facts that the temperature dependence of ρ_{xx} is faster than logarithmic (as might be expected for WL) and the resistivity greatly exceeds $\pi h/4e^2 \approx 20$ k Ω (maximum resistivity graphene in the absence of inter-valley scattering [122]) near the charge neutral point (CNP) at low temperature, suggest that electrons (holes) in the system are strongly localized. $\rho_{xx}(T)$ at different densities (figure 6.2) shows that below the resistivity of $h/2e^2$, the temperature dependence of resistivity follows logarithmic relation ($\approx \ln T$, consistent to the weak localization). However, the resistivity over the $h/2e^2$ increases even faster than the logarithmic function, which indicates that the localization strength is even stronger in the regime. As carrier density increases, the transition from WL to SL occurs at lower temperatures. The conductance mechanism of the strong localization regime cannot be described by simple mechanism such as variable range hopping (VRH). Especially, for temperatures below 5K, the resistivity deviates severely from the VRH conductance. We think the deviation implies magnetic impurity related mechanisms or electron-electron interaction or heating from current

source may need to be considered at the low temperature range (More studies are needed to resolve the temperature dependence.)

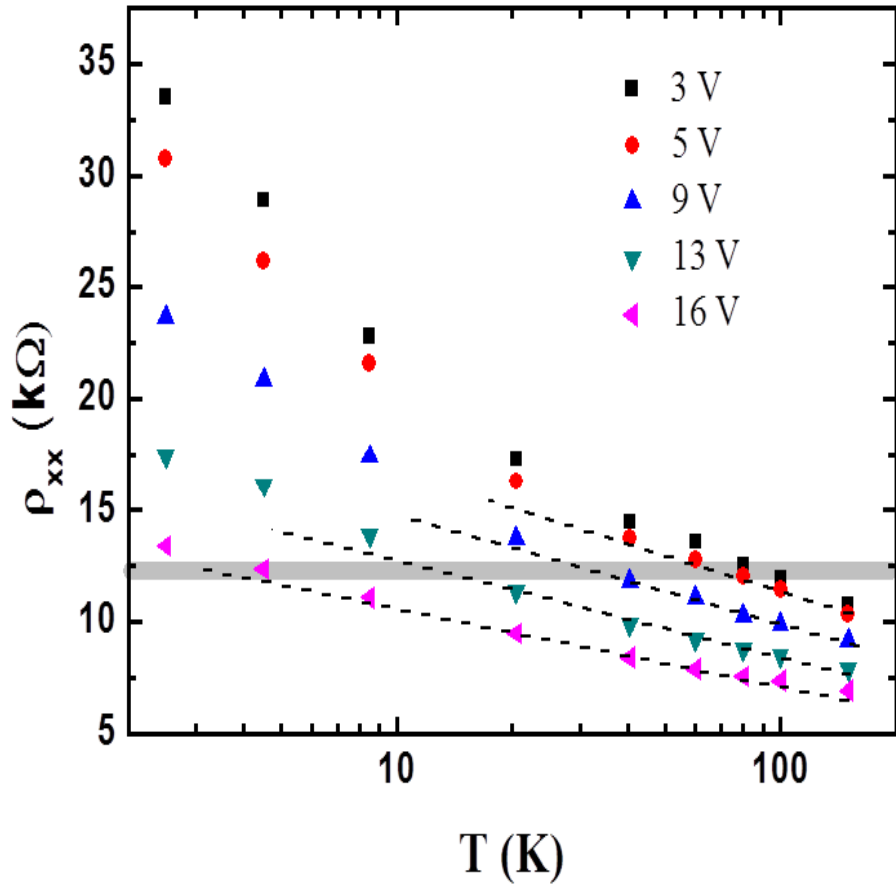


Figure 6.2 Temperature dependences of the ρ_{xx} for different carrier densities. Semi-log graph of ρ_{xx} vs T at four different carrier densities ($\Delta V_g = 3, 5, 9, 13, 16$ V). Above the resistivity (grey dark line $\sim h/2e^2$), the temperature dependence becomes stronger than a logarithmic relation (dashed line).

From both the atomic force microscope (AFM) image of the nano-scale Co clusters on graphene (see inset of Fig. 6.1 (a)) and the high intensity of the disorder (D) peak in Raman spectroscopy (indicating an increase in inter-valley scattering, see Fig. 6.1 (b)), we believe that the insulating behavior of the graphene is caused by increasing of the inter-valley scattering due to symmetry breaking associated with local hybridization between Co d orbitals and carbon (C) p_z states. Some theoretical simulations [123,124] indicate that Co atoms on graphene would chemically bond at the T site (directly above one of the carbon atoms in the unit cell) as the most favorable position. Note that such symmetry breaking is not achieved with adatoms sitting on h sites (center of hexagon) such as potassium ions, which explains the lack of insulating behavior for potassium on graphene as seen in chapter 4. Experimentally it is also observed that under certain conditions (the existence of hydrocarbon impurities), the reaction making Co-C bonds can be mediated by the impurities even under UHV. [125,126] Given the probable existence of some hydrocarbon contaminants in our sample (which cannot be completely removed even after resist residue cleaning), such chemical bonding could offer an alternate explanation for the observed symmetry breaking.

Figure 6.3 shows the gate voltage dependence of the longitudinal resistance $\rho_{xx}(V_g)$ and Hall resistance $\rho_{xy}(V_g)$ at a magnetic field $B = 10$ T at a temperature $T = 2.5$ K. The plateau in the Hall resistance $\rho_{xy} \approx h/2e^2$ and the corresponding $\rho_{xx} \sim 0$ indicate that the $\nu=2$ Landau level (LL) is quantized with the magnetic field even in this highly disordered insulating graphene sample. The inset of Fig. 6.3 shows the

magnetoresistance $\rho_{xx}(B)$ and Hall effect $\rho_{xy}(B)$ at $\Delta V_g = 8$ V. The giant negative magnetoresistance can be interpreted as the transition from the insulating regime to the quantum Hall regime. Note that in Fig. 6.3 main panel and inset, only the $\nu=2$ LL is observed, suggesting a transition from the insulating state directly to the $\nu=2$ LL as a function of magnetic field or gate voltage. This is consistent with numerical simulations of the quantum Hall effect in disordered graphene [39,127], in which the higher filling factor plateaus will disappear first with increasing disorder, and the $\nu = \pm 2$ plateaus are the most resistive to disorder.

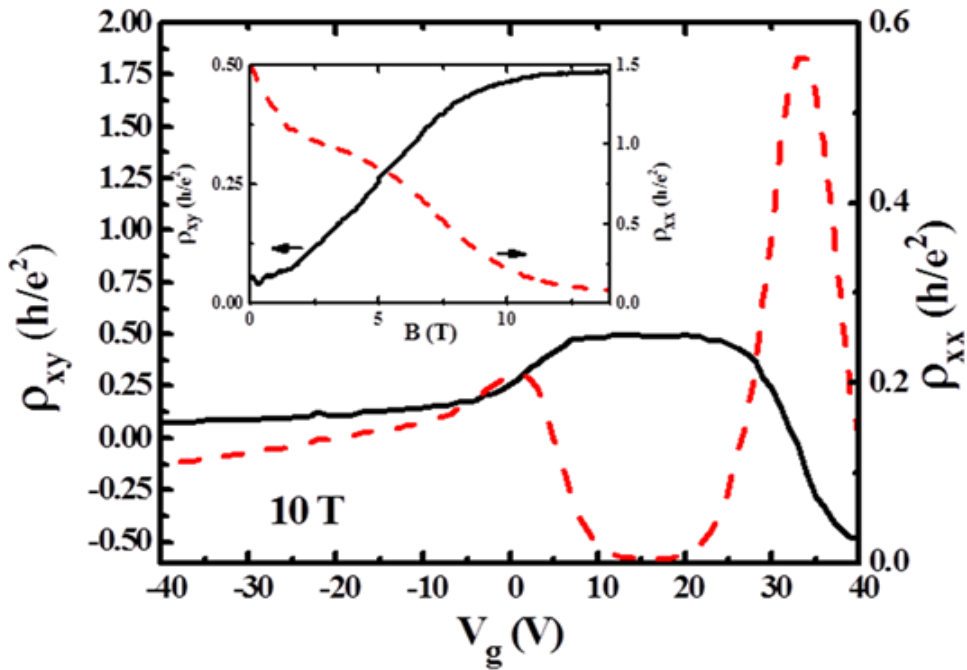


Figure 6.3 Longitudinal and Hall resistivities ρ_{xx}, ρ_{xy} of cobalt-decorated graphene as a function of gate voltage at 10 T and 2.5 K.

Inset shows ρ_{xx}, ρ_{xy} as a function of magnetic field at $\Delta V_g = 8$ V.

Fig. 6.4 (a) shows $\rho_{xx}(B)$ for five different temperatures from 2.5K to 10.5K. A clear temperature independent point B_c , separating insulating ($d\rho_{xx}/dT < 0$) from metallic ($d\rho_{xx}/dT > 0$) behavior is observed (arrow in Fig. 6.4 (a)). According to the scaling theory for two-dimensional quantum phase transitions, the resistivity should follow the scaling function: $\rho_{xx} = f[(B - B_c)T^{-\xi}]$ and hence $|d\rho_{xx}/dB|_{B=B_c} \propto T^{-\xi}$ near the transition point [51,128], where B_c is the critical magnetic field that the transition occurs and ξ is the temperature critical exponent. B_c was estimated from the Fig. 6.4 (a) by taking the cross point of the curves for different temperatures. Then ξ can be determined by plotting $\ln|d\rho_{xx}/dB|_{B_c}$ vs $\ln T$ as shown in Fig. 6.4 (b). From the slope of the linear fit, we obtained $\xi = 0.63 \pm 0.04$ for $\Delta V_g = 15$ V. The value is bigger than the universal value (0.42) known for other 2DEGs [129-131] and PP transitions in graphene, [40] while the number is close to the value (0.58) of PI transitions in graphene at high magnetic field [42]. It is also interesting to note that the QH state ($\nu = 2$) is four fold degenerate but the obtained values are not different from the cases of non-degenerate LL [132]. The deviations of the experimental data from the linear fit could be understood as marks of density fluctuations affected by magnetic field sweeps and gate voltage changes.

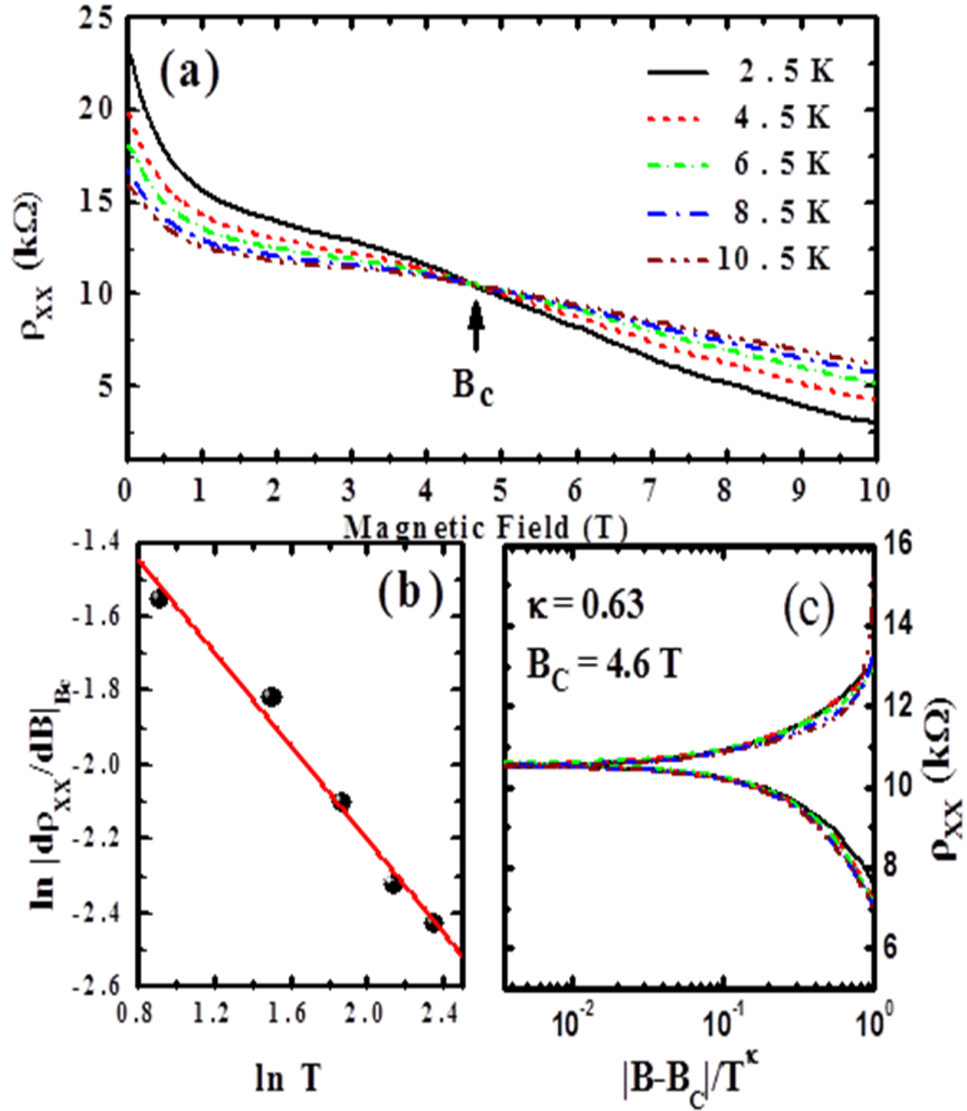


Figure 6.4 Phase transition at a fixed gate voltage.

(a) Longitudinal resistivity ρ_{xx} of cobalt-decorated graphene as a function of magnetic field at $\Delta V_g = 15$ V for different temperatures T from 2.5 to 10.5 K. The temperature independent point B_c , which separates insulating from metallic temperature-dependent resistivity, is depicted by an arrow. (b) $\ln |d\rho_{xx}/dB|_{B_c}$ vs. $\ln T$ at $\Delta V_g = 15$ V. The solid line has slope 0.63. (c) ρ_{xx} as a function of the dimensionless scaling variable $|B - B_c|/T^\xi$ for various temperatures.

Using the two parameters, B_c and ξ , we tested the scaling relation independently by plotting ρ_{xx} against the scaling variables of $|B - B_c|T^{-\xi}$. As shown in Fig. 6.4 (c), ρ_{xx} for five different temperatures collapse into two distinct branches with very symmetric shapes. The scaling behavior strongly suggests that the I-QH transition is indeed a quantum phase transition. The temperature range (~ 10 K) over which scaling persists in disordered graphene is relatively high compared to other 2DESSs, likely due to the large energy gaps between LLs and relative lack of temperature-dependent scattering.

Fig. 6.5 (a) shows four sets of (smoothed) magnetoresistance $\rho_{xx}(B)$ at various temperatures, corresponding to four different gate voltages away from the CNP ($\Delta V_g = 5V, 9V, 13V, 17V$) respectively. The sample is placed in air for several days after the first measurement (Fig. 6.4), but the second measurements (Fig 6.5) also show similar behaviors. As depicted in Fig 6.5. (b), the linear relation between $\ln|d\rho_{xx}/dB|_{B_c}$ and $\ln T$ for each gate voltage is used again to evaluate the critical exponent ξ . The scaling behavior of $\rho_{xx}(B)$ (such as seen in Fig 6.4 (b)) was also checked independently for all the gate voltages. Results of the evaluation of ξ as a function of relative gate voltage are summarized in Fig. 6.5 (c). The scaling exponent ξ for each carrier density is not universal, rather it varies with gate voltages from 0.4 to higher values as the charge carrier density increases. It might be interesting to note that slope of the linear relations appears to be systematically changing to lower value as temperature decreases. To verify the temperature dependence of the critical exponents, further measurements at lower temperatures are required.

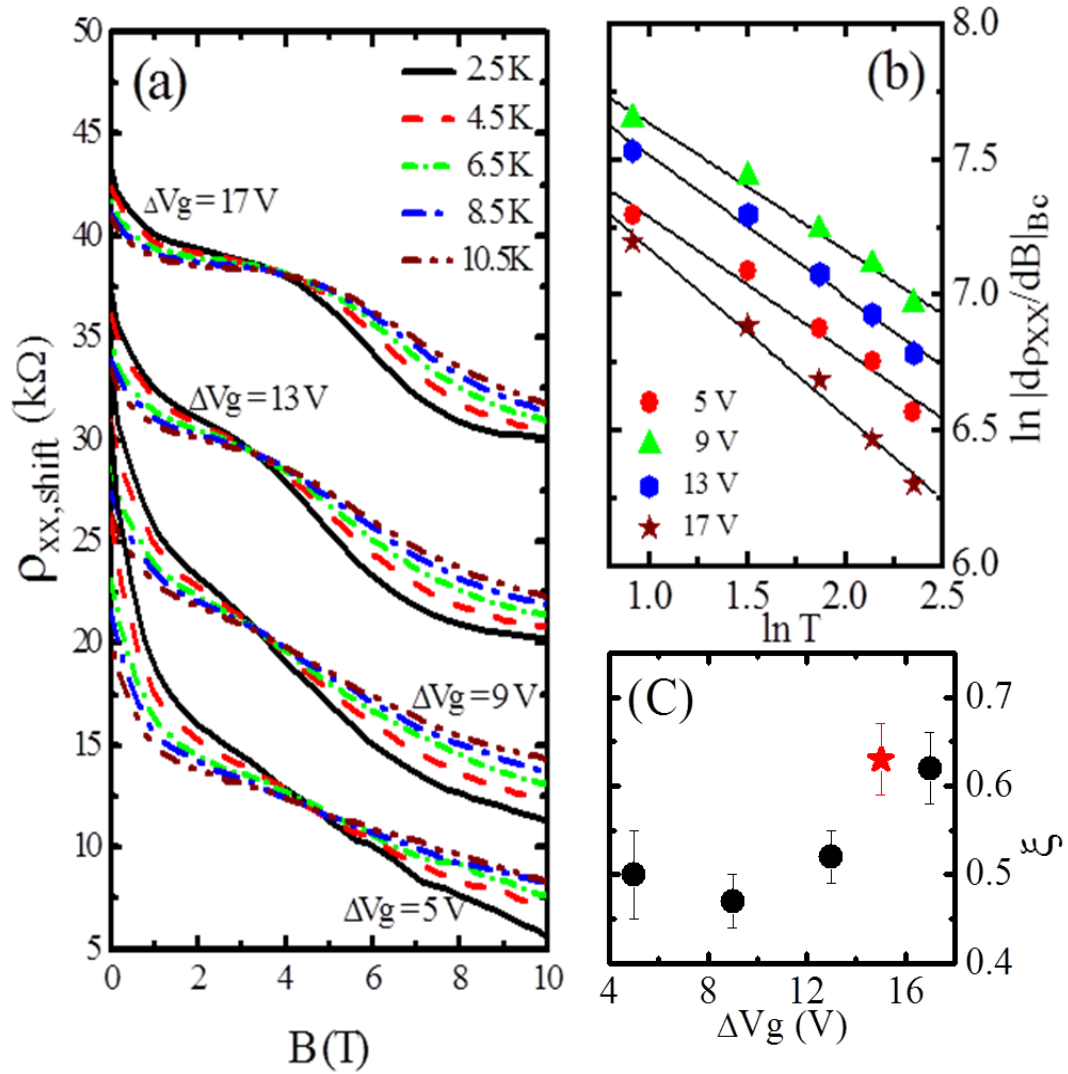


Figure 6.5 The phase transition at different carrier densities (gate voltages). (a) Longitudinal resistivity ρ_{xx} of cobalt-decorrated graphene as a function of magnetic field for different temperatures T from 2.5 K to 10.5 K at four different gate voltages. The resistivities are shifted upward for each gate voltage to show all lines separately. (b) $\ln |d\rho_{xx}/dB|_{B_c}$ vs $\ln T$ at four different gate voltages. The solid lines are the linear fits indicating the critical exponent ξ . (c) The critical exponent ξ determined from Fig 6.4 (red star) and (b) (black circle) as a function of ΔV_g

The temperature critical exponent can be expressed as $\xi = p/2\gamma$, where γ is the localization critical exponent and p is the temperature exponent of inelastic scattering [40,133]. Within Fermi liquid theory, p is expected to be 2 [133,134]. Given that inelastic scattering is unlikely limited by the sample size ($\approx 10\mu\text{m}$) within the temperature range of the measurements, we assume that the value of p does not change with carrier density. Then any density dependence of ξ would reflect density dependence of γ . Remarkably, unlike the universal value found for other 2DEGs ($\gamma = 7/3$) [129-131,133,135-140], graphene with certain types of disorder has been predicted to belong to a new universality class in which the value of γ varies continuously [62]. For example, with bond disorders with mass, numerical simulations showed that the value is close to $7/3$ and continuously decreases to 1 as the strength of the disorder changes from strong to weak [62,63]. In our sample it appears that localization behavior is diminished with increasing carrier density (see figure 6.2 (a),(b)), which qualitatively explains the non-universal and the variation of the critical exponents in Fig 6.5 (c). We note that for the gate voltage near the CNP, inhomogeneous carrier density (electron and hole puddles) make it difficult to measure ξ .

Another possible explanation for the density dependence of the critical exponents is the transition of the dominant percolation mechanism from classical to quantum as the temperature is lowered, as has been supposed to occur previously in conventional 2DEG experiments [60,141]. More theoretical work is needed on the classical to quantum transition in graphene to understand whether this could be the

case.

In the phase diagram found by numerical study [39], the transition into higher ($\nu > 2$) plateaus also can be expected when the disorder is reduced. I fabricated an additional cobalt-decorated sample which exhibited $\nu = 2$ and $\nu = 6$ plateaus, however insulating behavior could not be seen at a carrier density for which the $\nu = 6$ plateau occurred, so the insulator to $\nu = 6$ QH transition could not be studied. It seems that for present samples the impurity density needed to induce clear insulating behavior also is sufficient to destroy all but the $\nu = 2$ level at magnetic fields less than 15 T. Thus the I-QH transition for higher Landau level is not observable so far and might be difficult to be observed in the future. However, studies at higher magnetic fields, and also starting with cleaner samples (such that inter-valley scattering could become dominant at a lower total scattering rate) would be of interest.

In conclusion, strong localization in graphene was achieved with chemisorption of Co clusters. The transition from the insulating state to the quantum Hall state ($\nu = 2$) was observed as a function of magnetic field and carrier density. Scaling analysis supports that the transition is a quantum phase transition caused by magnetic fields in 2D. The critical scaling exponent ζ was possibly non-universal, increasing from near 0.4 to 0.8 with carrier density increase. This may reflect a change in the localization critical exponent γ which has been predicted for certain kinds of disorder in graphene. The fact that both the type and strength of disorder can be controllably tuned in a single graphene sample, and the relatively low transition magnetic field, make graphene an interesting system for further study of low dimensional quantum phase transitions.

Chapter 7 : Summary

The pace of graphene research is incredibly fast. The first gated graphene device was reported in 2004, one year before I joined my graduate program. And before the completion of my degree, the 2010 Nobel Prize was awarded to the researchers who demonstrated the initial graphene device. (One may blame my slow progress in graduate school though.) Therefore parts of the works described in my thesis already have been expanded upon by many other groups. Also relatively new results would induce similar research keeping up with the fast development. In this chapter I will summarize the main three topics of the thesis and introduce the effects of the works as briefly mentioning (future) follow up experiments.

In chapter 4, through the addition of potassium ions on graphene in ultrahigh vacuum, we investigated the effect of Coulomb scatterers on graphene conductivity. The measured conductivity with charged impurities quantitatively agrees with the prediction of the Boltzmann transport theory limited by long-range Coulomb disorder. The experiments demonstrated that the linear carrier-density-dependent conductivity is associated with long-range scattering, suggesting that long-range Coulomb disorder is the main scattering mechanism in graphene. Furthermore, the experiments demonstrated the relative insensitivity of the minimum conductivity in graphene to the amount of long-range disorder. The fact that the minimum conductivity is observed to be similar in samples of widely different mobility fabricated by different

research groups [6,29,142] is also consistent with long range scattering as the source of disorder in all graphene samples on SiO₂.

The identification of charged impurities (particularly charged impurities in the substrate) as a major source of disorder in graphene in the works discussed in this thesis as well as work by other researchers[143], has led to significant improvements in graphene device quality through use of alternative substrates to SiO₂ or removal of the substrate altogether. One example is the drastic improvement of mobility in suspended graphene with current annealing [96,110]. This suggests that the long-range scatterers are in the SiO₂ substrate, and removal of the substrate increases the mobility. Most interestingly and recently, high field effect mobility has been obtained in graphene devices fabricated on hexagonal boron nitride (h-BN) substrates [144], where it is assumed that the crystalline h-BN lattice has fewer charge traps than amorphous SiO₂. The reduction in long-range disorder has begun another era of graphene transport research, allowing researchers to discover new and useful properties of graphene such as fractional QHE and the opening of a band gap in bilayer graphene [145], made accessible in low-disorder graphene devices.

Another prediction of the transport theory with Coulomb scattering as the dominant mechanism, increased mobility by reducing the effective fine structure constant (r_s), is verified in chapter 5. There, r_s is changed by deposition of ice layers on graphene in ultrahigh vacuum, and 30% increased mobility is obtained with the ice top dielectric layer.

The results, which are successfully explained by transport theory of screened scattering, strongly suggested the use of high dielectric constant (κ) substrates (or upper layers) for achievement of high mobility graphene devices. However, experimental results obtained since that time have been at times inconclusive or controversial. Several groups have experimented with high κ dielectric overlayers on graphene [146-149]. In some cases the mobility of graphene has been increased slightly through deposition of a dielectric overlayer [146-148], but typically the mobility is decreased. This could be understood by an increase in the impurity density as the deposited material undoubtedly contains additional charge traps. More significantly, Ponomarenko et al. [150] reported that the mobility of graphene measured in high κ liquids (water, ethanol) was found to increase only slightly, though the very high dielectric constant of these liquids would predict a large mobility increase. The authors took this as evidence that charged impurities are not the dominant scattering source in graphene on SiO₂. Also other experiments with liquids showed a change in gating capacitance not mobility of the graphene sample [151]. The reasons for the apparent experimental disagreements are not well understood. There is a numerical study [152] that showed the increase in mobility would be limited by surface phonon of the substrates. A recent unpublished study of suspended graphene in polar and non-polar liquids showed the expected dependence of mobility on dielectric constant for non-polar liquids, but no increase in mobility for polar liquids. This was interpreted as evidence of additional scattering by charged ions in the polar liquids canceling any effect of increasing dielectric constant [153].

In addition to the semi-classical transport in graphene, quantum transport with adatoms was also investigated in the last part of the thesis (chapter 6); where magnetotransport of disordered graphene was used to probe the insulator-quantum Hall transition. Similar to other 2DES, we observed a low magnetic field induced phase transition in the Co added (disordered) graphene: localization to the delocalized $\nu=2$ quantum Hall state.

The insulating nature of graphene with disorder which increases inter-valley scattering has been reported by many other groups.[114-116,154] But the phase transition with magnetic field has not been studied previously. My experimental result suggests that the large negative magneto-resistance observed in the insulating graphene could be a signature of the phase transition in the system.

In chapter 6, the role of Co clusters on graphene as magnetic impurity is not considered. But graphene can be considered as a good material for spintronics [155,156] due to long spin scattering time rooted from long mean free path and extremely small spin-orbit coupling [157]. The fact that graphene retains its Dirac electronic properties with minimal doping in the presence of cobalt overlayers may open possibilities for increasing the spin-orbit interaction in graphene through the addition of magnetic adatoms. Further studies of the interaction between magnetic impurities and charge and spin transport in graphene may be interesting.

Finally, I will finish this dissertation by discussing the ambitious future of graphene. One of the main future research directions is to make graphene transistors which could replace silicon in the semiconductor industry. The physical limit of

making silicon transistors smaller requires a new breakthrough in order to make semiconductor chips with better performance and lower power consumption. For graphene, a lack of band gap is the main obstacle to the final goal. Graphene nanoribbons in which a band gap is generated by quantum confinement, and the tunable band gap opened by electric field applied perpendicular to clean bilayer graphene seem to be promising approaches so far.

Even without modification to open a bandgap, graphene also is promising for many applications. A long spin diffusion length even at room temperature makes it an interesting candidate for spintronics. A true two dimensional nature of the material implies variety usages such as strain sensors, chemical and biological sensors. The lack of gap combined with transparency of graphene suggests the use as a transparent electrode for applications such as solar photovoltaic cells. The linear dispersion allows adsorption of light with wide spectrum. Even in the biological area, one can find possible applications, for example DNA sequencing. Nanopores in graphene sheets could be made just big enough for DNA strands to pass through, and the electrical property change of graphene due to interaction with each base pair could be detected[158-160]. The possible applications of graphene as a new material in industry are almost limitless, it could replace carbon fiber in composite form to make lighter and stronger plates useful for aero industry, embedding graphene on transparent and flexible substrate possibly opens a way to make advanced conducting and transparent electrodes. Recently Samsung Electronics announced they would launch a new type of cell phone made out of the graphene-based flexible substrate by 2013. And graphene-based material is being used now as an additive by oil industry

to drilling fluids to prevent from clogging pores. We will likely see that graphene become common place material as plastic is now.

Bibliography

- 1 Klitzing, K. v., Dorda, G. & Pepper, M. New Method for High-Accuracy Determination of the Fine-Structure Constant Based on Quantized Hall Resistance. *Phys. Rev. Lett.* **45**, 494 (1980).
- 2 Ando, T., Fowler, A. B. & Stern, F. Electronic properties of two-dimensional systems. *Reviews of Modern Physics* **54**, 437 (1982).
- 3 Pierret, R. F. & Neudeck, G. (Addison-Wesley, Reading, MA, 1983).
- 4 Lu, X., Yu, M., Huang, H. & Ruoff, R. S. Tailoring graphite with the goal of achieving single sheets. *Nanotechnology* **10**, 269 (1999).
- 5 Zhang, Y., Small, J. P., Pontius, W. V. & Kim, P. Fabrication and electric-field-dependent transport measurements of mesoscopic graphite devices. *Appl. Phys. Lett.* **86**, 073104 (2005).
- 6 Novoselov, K., Geim, A., Morozov, S. *et al.* Electric field effect in atomically thin carbon films. *Science* **306**, 666 (2004).
- 7 Wallace, P. The band theory of graphite. *Physical Review* **71**, 622 (1947).
- 8 McClure, J. Band structure of graphite and de Haas-van Alphen effect. *Physical Review* **108**, 612 (1957).
- 9 Slonczewski, J. & Weiss, P. Band structure of graphite. *Physical Review* **109**, 272 (1958).
- 10 Wilson, M. Electrons in atomically thin carbon sheets behave like massless particles. *Physics Today* **59**, 21 (2006).

- 11 Semenoff, G. W. Condensed-Matter Simulation of a Three-Dimensional Anomaly. *Phys. Rev. Lett.* **53**, 2449 (1984).
- 12 Chen, J. H., Jang, C., Adam, S. *et al.* Charged-impurity scattering in graphene. *Nat Phys* **4**, 377 (2008).
- 13 Jang, C., Adam, S., Chen, J. H. *et al.* Tuning the effective fine structure constant in graphene: opposing effects of dielectric screening on short-and long-range potential scattering. *Phys. Rev. Lett.* **101**, 146805 (2008).
- 14 Shon, Y. & Ando, T. Quantum transport in two-dimensional graphite system. *JOURNAL-PHYSICAL SOCIETY OF JAPAN* **67**, 2421 (1998).
- 15 Novoselov, K., Jiang, D., Schedin, F. *et al.* Two-dimensional atomic crystals. *Proc. Natl. Acad. Sci. U. S. A.* **102**, 10451 (2005).
- 16 Zhang, Y., Tan, Y.-W., Stormer, H. L. & Kim, P. Experimental observation of the quantum Hall effect and Berry's phase in graphene. *Nature* **438**, 201 (2005).
- 17 Novoselov, K. S., Geim, A. K., Morozov, S. V. *et al.* Two-dimensional gas of massless Dirac fermions in graphene. *Nature* **438**, 197 (2005).
- 18 Ando, T. Screening effect and impurity scattering in monolayer graphene. *J. Phys. Soc. Jpn.* **75**, 4716 (2006).
- 19 Cheianov, V. V. & Fal'ko, V. I. Friedel oscillations, impurity scattering, and temperature dependence of resistivity in graphene. *Phys. Rev. Lett.* **97**, 226801 (2006).
- 20 Nomura, K. & MacDonald, A. H. Quantum Hall ferromagnetism in graphene. *Phys. Rev. Lett.* **96**, 256602 (2006).

- 21 Nomura, K. & MacDonald, A. Quantum transport of massless Dirac fermions. *Phys. Rev. Lett.* **98**, 76602 (2007).
- 22 Hwang, E., Adam, S. & Das Sarma, S. Carrier transport in two-dimensional graphene layers. *Phys. Rev. Lett.* **98**, 186806 (2007).
- 23 Katsnelson, M., Guinea, F. & Geim, A. Scattering of electrons in graphene by clusters of impurities. *Physical Review B* **79**, 195426 (2009).
- 24 Trushin, M. & Schliemann, J. Conductivity of graphene: How to distinguish between samples with short-and long-range scatterers. *EPL (Europhysics Letters)* **83**, 17001 (2008).
- 25 Adam, S., Hwang, E., Galitski, V. & Das Sarma, S. A self-consistent theory for graphene transport. *Proceedings of the National Academy of Sciences* **104**, 18392 (2007).
- 26 Hwang, E. & Sarma, S. D. Dielectric function, screening, and plasmons in two-dimensional graphene. *Physical Review B* **75**, 205418 (2007).
- 27 Adam, S., Hwang, E. & Das Sarma, S. Scattering mechanisms and Boltzmann transport in graphene. *Physica E: Low-dimensional Systems and Nanostructures* **40**, 1022 (2008).
- 28 Katsnelson, M. Zitterbewegung, chirality, and minimal conductivity in graphene. *The European Physical Journal B-Condensed Matter and Complex Systems* **51**, 157 (2006).
- 29 Tan, Y. W., Zhang, Y., Bolotin, K. *et al.* Measurement of scattering rate and minimum conductivity in graphene. *Phys. Rev. Lett.* **99**, 246803 (2007).

- 30 Rossi, E. & Das Sarma, S. Ground state of graphene in the presence of random charged impurities. *Phys. Rev. Lett.* **101**, 166803 (2008).
- 31 Rossi, E., Adam, S. & Sarma, S. D. Effective medium theory for disordered two-dimensional graphene. *Physical Review B* **79**, 245423 (2009).
- 32 Peres, N., Guinea, F. & Neto, A. H. C. Electronic properties of disordered two-dimensional carbon. *Physical Review B* **73**, 125411 (2006).
- 33 Jackiw, R. Fractional charge and zero modes for planar systems in a magnetic field. *Physical Review D* **29**, 2375 (1984).
- 34 Haldane, F. Model for a Quantum Hall Effect without Landau Levels: Condensed-Matter Realization of the "Parity Anomaly". *Phys. Rev. Lett.* **61**, 2015 (1988).
- 35 Gusynin, V. & Sharapov, S. Unconventional integer quantum Hall effect in graphene. *Phys. Rev. Lett.* **95**, 146801 (2005).
- 36 Mikitik, G. & Sharlai, Y. V. Manifestation of Berry's phase in metal physics. *Phys. Rev. Lett.* **82**, 2147 (1999).
- 37 Luk'yanchuk, I. A. & Kopelevich, Y. Phase analysis of quantum oscillations in graphite. *Phys. Rev. Lett.* **93**, 166402 (2004).
- 38 Abrahams, E., Anderson, P., Licciardello, D. & Ramakrishnan, T. Scaling theory of localization: Absence of quantum diffusion in two dimensions. *Phys. Rev. Lett.* **42**, 673 (1979).
- 39 Sheng, D., Sheng, L. & Weng, Z. Quantum Hall effect in graphene: Disorder effect and phase diagram. *Physical Review B* **73**, 233406 (2006).

- 40 Giesbers, A., Zeitler, U., Ponomarenko, L. *et al.* Scaling of the quantum Hall plateau-plateau transition in graphene. *Physical Review B* **80**, 241411 (2009).
- 41 Zhang, L., Zhang, Y., Khodas, M., Valla, T. & Zaliznyak, I. Metal to insulator transition on the $N=0$ Landau level in graphene. *Phys. Rev. Lett.* **105**, 46804 (2010).
- 42 Amado, M., Diez, E., López-Romero, D. *et al.* Plateau–insulator transition in graphene. *New Journal of Physics* **12**, 053004 (2010).
- 43 Novoselov, K., McCann, E., Morozov, S. *et al.* Unconventional quantum Hall effect and Berry’s phase of 2π in bilayer graphene. *Nature Physics* **2**, 177 (2006).
- 44 Khmelnitskii, D. Quantum hall effect and additional oscillations of conductivity in weak magnetic fields. *Phys. Lett. A* **106**, 182 (1984).
- 45 Laughlin, R. Levitation of extended-state bands in a strong magnetic field. *Phys. Rev. Lett.* **52**, 2304 (1984).
- 46 Kivelson, S., Lee, D. H. & Zhang, S. C. Global phase diagram in the quantum Hall effect. *Physical Review B* **46**, 2223 (1992).
- 47 Huang, T. Y., Liang, C. T., Kim, G. H. *et al.* From insulator to quantum Hall liquid at low magnetic fields. *Physical Review B* **78**, 113305 (2008).
- 48 Kim, G. H., Liang, C. T., Huang, C. *et al.* From localization to Landau quantization in a two-dimensional GaAs electron system containing self-assembled InAs quantum dots. *Physical Review B* **69**, 073311 (2004).

- 49 Song, S. H., Shahar, D., Tsui, D., Xie, Y. & Monroe, D. New Universality at the Magnetic Field Driven Insulator to Integer Quantum Hall Effect Transitions. *Phys. Rev. Lett.* **78**, 2200 (1997).
- 50 Jiang, H., Johnson, C., Wang, K. & Hannahs, S. Observation of magnetic-field-induced delocalization: Transition from Anderson insulator to Quantum Hall conductor. *Phys. Rev. Lett.* **71**, 1439 (1993).
- 51 Wang, T., Clark, K., Spencer, G., Mack, A. & Kirk, W. Magnetic-field-induced metal-insulator transition in two dimensions. *Phys. Rev. Lett.* **72**, 709 (1994).
- 52 Hughes, R., Nicholls, J., Frost, J. *et al.* Magnetic-field-induced insulator-quantum Hall-insulator transition in a disordered two-dimensional electron gas. *J. Phys.: Condens. Matter* **6**, 4763 (1994).
- 53 Shahar, D., Tsui, D. & Cunningham, J. Observation of the $\nu = 1$ quantum Hall effect in a strongly localized two-dimensional system. *Physical Review B* **52**, 14372 (1995).
- 54 Sheng, D. & Weng, Z. Disappearance of integer quantum Hall effect. *Phys. Rev. Lett.* **78**, 318 (1997).
- 55 Liu, D., Xie, X. & Niu, Q. Weak field phase diagram for an integer quantum hall liquid. *Phys. Rev. Lett.* **76**, 975 (1996).
- 56 Hilke, M., Shahar, D., Song, S., Tsui, D. & Xie, Y. Phase diagram of the integer quantum Hall effect in p-type germanium. *Physical Review B* **62**, 6940 (2000).

- 57 Lee, C., Chang, Y., Suen, Y. & Lin, H. Magnetic-field-induced delocalization in center-doped GaAs/Al_xGa_{1-x}As multiple quantum wells. *Physical Review B* **58**, 10629 (1998).
- 58 Xiong, G., Wang, S. D., Niu, Q., Wang, Y. & Wang, X. R. A possible unified picture for both scaling and non-scaling plateau-to-plateau transitions in quantum Hall systems. *EPL (Europhysics Letters)* **82**, 47008 (2008).
- 59 Suzuura, H. & Ando, T. Crossover from symplectic to orthogonal class in a two-dimensional honeycomb lattice. *Phys. Rev. Lett.* **89**, 266603 (2002).
- 60 Li, W., Csathy, G., Tsui, D., Pfeiffer, L. & West, K. Scaling and universality of integer quantum Hall plateau-to-plateau transitions. *Phys. Rev. Lett.* **94**, 206807 (2005).
- 61 Li, W., Vicente, C., Xia, J. *et al.* Scaling in Plateau-to-Plateau Transition: A Direct Connection of Quantum Hall Systems with the Anderson Localization Model. *Phys. Rev. Lett.* **102**, 216801 (2009).
- 62 Goswami, P., Jia, X. & Chakravarty, S. Quantum Hall plateau transition in the lowest Landau level of disordered graphene. *Physical Review B* **76**, 205408 (2007).
- 63 Jia, X., Goswami, P. & Chakravarty, S. Dissipation and criticality in the lowest Landau level of graphene. *Phys. Rev. Lett.* **101**, 36805 (2008).
- 64 Ferrari, A., Meyer, J., Scardaci, V. *et al.* Raman spectrum of graphene and graphene layers. *Phys. Rev. Lett.* **97**, 187401 (2006).
- 65 Berger, C., Song, Z., Li, X. *et al.* Electronic confinement and coherence in patterned epitaxial graphene. *Science* **312**, 1191 (2006).

- 66 Ishigami, M., Chen, J., Cullen, W., Fuhrer, M. & Williams, E. Atomic structure of graphene on SiO₂. *Nano Lett.* **7**, 1643 (2007).
- 67 Stanford Research Systems, Application note # 3.
- 68 Chen, J. H., Ishigami, M., Jang, C. *et al.* Printed Graphene Circuits. *Adv. Mater.* **19**, 3623, doi:10.1002/adma.200701059 (2007).
- 69 Cho, S. & Fuhrer, M. S. Charge transport and inhomogeneity near the minimum conductivity point in graphene. *Physical Review B* **77**, 081402 (2008).
- 70 Ziegler, K. Robust transport properties in graphene. *Phys. Rev. Lett.* **97**, 266802 (2006).
- 71 Kim, E. A. & Castro Neto, A. Graphene as an electronic membrane. *EPL (Europhysics Letters)* **84**, 57007 (2008).
- 72 Katsnelson, M. & Geim, A. Electron scattering on microscopic corrugations in graphene. *Philosophical Transactions of the Royal Society A: Mathematical, Physical and Engineering Sciences* **366**, 195 (2008).
- 73 Novikov, D. Numbers of donors and acceptors from transport measurements in graphene. *Appl. Phys. Lett.* **91**, 102102 (2007).
- 74 Trushin, M. & Schliemann, J. Minimum electrical and thermal conductivity of graphene: a quasiclassical approach. *Phys. Rev. Lett.* **99**, 216602 (2007).
- 75 Yan, X. Z., Romiah, Y. & Ting, C. Electric transport theory of Dirac fermions in graphene. *Physical Review B* **77**, 125409 (2008).
- 76 Chen, J. H., Ishigami, M., Jang, C. *et al.* Printed graphene circuits. *Arxiv preprint arXiv:0809.1634* (2008).

- 77 Fradkin, E. Critical behavior of disordered degenerate semiconductors. II. Spectrum and transport properties in mean-field theory. *Physical Review B* **33**, 3263 (1986).
- 78 Ludwig, A. W. W., Fisher, M. P. A., Shankar, R. & Grinstein, G. Integer quantum Hall transition: An alternative approach and exact results. *Physical Review B* **50**, 7526 (1994).
- 79 Sjövall, P. Intercalation of potassium in graphite studied by thermal desorption spectroscopy. *Surf. Sci.* **345**, L39 (1996).
- 80 Schedin, F., Geim, A., Morozov, S. *et al.* Detection of individual gas molecules absorbed on graphene. *Nat. Mater.* **6**, 652 (2007).
- 81 Hwang, E., Adam, S. & Sarma, S. D. Transport in chemically doped graphene in the presence of adsorbed molecules. *Physical Review B* **76**, 195421 (2007).
- 82 Caragiu, M. & Finberg, S. Alkali metal adsorption on graphite: a review. *J. Phys.: Condens. Matter* **17**, R995 (2005).
- 83 Dresselhaus, M. & Dresselhaus, G. Intercalation compounds of graphite. *Advances in Physics* **30**, 139 (1981).
- 84 Ziambaras, E., Kleis, J., Schröder, E. & Hyldgaard, P. Potassium intercalation in graphite: A van der Waals density-functional study. *Physical Review B* **76**, 155425 (2007).
- 85 Rutter, G., Crain, J., Guisinger, N. & Li, T. Scattering and interference in epitaxial graphene. *Science* **317**, 219 (2007).
- 86 Tworzydło, J., Trauzettel, B., Titov, M., Rycerz, A. & Beenakker, C. W. J. Sub-Poissonian shot noise in graphene. *Phys. Rev. Lett.* **96**, 246802 (2006).

- 87 Van Mieghem, P. Theory of band tails in heavily doped semiconductors. *Reviews of Modern Physics* **64**, 755 (1992).
- 88 Cheianov, V. V., Fal'ko, V. I., Altshuler, B. L. & Aleiner, I. L. Random resistor network model of minimal conductivity in graphene. *Phys. Rev. Lett.* **99**, 176801 (2007).
- 89 Mohr, M., Maultzsch, J., Dobardži, E. *et al.* Phonon dispersion of graphite by inelastic x-ray scattering. *Physical Review B* **76**, 035439 (2007).
- 90 Li, Z., Hock, K., Palmer, R. & Annett, J. Potassium-adsorption-induced plasmon frequency shift in graphite. *J. Phys.: Condens. Matter* **3**, S103 (1991).
- 91 Peres, N., Guinea, F. & Neto, A. H. C. Coulomb interactions and ferromagnetism in pure and doped graphene. *Physical Review B* **72**, 174406 (2005).
- 92 Min, H., Bistritzer, R., Su, J. J. & MacDonald, A. Room-temperature superfluidity in graphene bilayers. *physical review B* **78**, 121401(R) (2008).
- 93 Jena, D. & Konar, A. Enhancement of carrier mobility in semiconductor nanostructures by dielectric engineering. *Phys. Rev. Lett.* **98**, 136805 (2007).
- 94 Sarma, S. D. & Vinter, B. Effect of impurity scattering on the distribution function in two-dimensional Fermi systems. *Physical Review B* **24**, 549 (1981).
- 95 Jiang, Z., Henriksen, E., Tung, L. *et al.* Infrared spectroscopy of Landau levels of graphene. *Phys. Rev. Lett.* **98**, 197403 (2007).

- 96 Bolotin, K., Sikes, K., Jiang, Z. *et al.* Ultrahigh electron mobility in suspended graphene. *Solid State Commun.* **146**, 351 (2008).
- 97 Petrenko, V. F. & Whitworth, R. W. *Physics of ice*. (Oxford University Press, USA, 1999).
- 98 Cabrera Sanfelix, P., Holloway, S., Kolasinski, K. & Darling, G. The structure of water on the (0 0 0 1) surface of graphite. *Surf. Sci.* **532**, 166 (2003).
- 99 Thiel, P. A. & Madey, T. E. The interaction of water with solid surfaces: fundamental aspects. *Surf. Sci. Rep.* **7**, 211 (1987).
- 100 Morozov, S., Novoselov, K., Katsnelson, M. *et al.* Giant intrinsic carrier mobilities in graphene and its bilayer. *Phys. Rev. Lett.* **100**, 16602 (2008).
- 101 Martin, J., Akerman, N., Ulbricht, G. *et al.* Observation of electron-hole puddles in graphene using a scanning single electron transistor. *Nature Physics* **4**, 144 (2007).
- 102 Huard, B., Stander, N., Sulpizio, J. & Goldhaber-Gordon, D. Evidence of the role of contacts on the observed electron-hole asymmetry in graphene. *Physical Review B* **78**, 121402 (2008).
- 103 Zhang, Y., Jiang, Z., Small, J. *et al.* Landau-level splitting in graphene in high magnetic fields. *Phys. Rev. Lett.* **96**, 136806 (2006).
- 104 Jiang, Z., Zhang, Y., Stormer, H. & Kim, P. Quantum Hall states near the charge-neutral Dirac point in graphene. *Phys. Rev. Lett.* **99**, 106802 (2007).
- 105 Giesbers, A., Zeitler, U., Katsnelson, M. *et al.* Quantum-Hall activation gaps in graphene. *Phys. Rev. Lett.* **99**, 206803 (2007).

- 106 Giesbers, A., Ponomarenko, L., Novoselov, K. *et al.* Gap opening in the zeroth Landau level of graphene. *Physical Review B* **80**, 201403 (2009).
- 107 Checkelsky, J. G., Li, L. & Ong, N. Zero-energy state in graphene in a high magnetic field. *Phys. Rev. Lett.* **100**, 206801 (2008).
- 108 Checkelsky, J. G., Li, L. & Ong, N. Divergent resistance at the Dirac point in graphene: Evidence for a transition in a high magnetic field. *Physical Review B* **79**, 115434 (2009).
- 109 Zhang, L., Camacho, J., Cao, H. *et al.* Breakdown of the $N=0$ quantum Hall state in graphene: Two insulating regimes. *Physical Review B* **80**, 241412 (2009).
- 110 Du, X., Skachko, I., Barker, A. & Andrei, E. Y. Approaching ballistic transport in suspended graphene. *Nature Nanotechnology* **3**, 491 (2008).
- 111 Bolotin, K. I., Ghahari, F., Shulman, M. D., Stormer, H. L. & Kim, P. Observation of the fractional quantum Hall effect in graphene. *Nature* **462**, 196 (2009).
- 112 Feldman, B. E., Martin, J. & Yacoby, A. Broken-symmetry states and divergent resistance in suspended bilayer graphene. *Nature Physics* **5**, 889 (2009).
- 113 Bostwick, A., McChesney, J. L., Emtsev, K. V. *et al.* Quasiparticle transformation during a metal-insulator transition in graphene. *Phys. Rev. Lett.* **103**, 56404 (2009).

- 114 Moser, J., Tao, H., Roche, S. *et al.* Magnetotransport in disordered graphene exposed to ozone: From weak to strong localization. *Physical Review B* **81**, 205445 (2010).
- 115 Hong, X., Cheng, S. H., Herding, C. & Zhu, J. Colossal negative magnetoresistance in dilute fluorinated graphene. *Physical Review B* **83**, 085410 (2011).
- 116 Skrypnik, Y. V. & Loktev, V. M. Metal-insulator transition in hydrogenated graphene as manifestation of quasiparticle spectrum rearrangement of anomalous type. *Physical Review B* **83**, 085421 (2011).
- 117 Pudalov, V., D'lorio, M. & Campbell, J. Hall resistance and quantized Hall effect to insulator transitions in a 2D electron system. *JETP LETTERS C/C OF PIS'MA V ZHURNAL EKSPERIMENTAL'NOI TEORETICHESKOI FIZIKI* **57**, 608 (1993).
- 118 Lee, C. H., Chang, Y. H., Suen, Y. W. & Lin, H. H. Magnetic-field-induced insulator-quantum Hall conductor-insulator transitions in doped GaAs/Al_xGa_{1-x}As quantum wells. *Physical Review B* **56**, 15238 (1997).
- 119 Huang, C., Chang, Y., Lee, C. *et al.* Insulator-quantum Hall conductor transitions at low magnetic field. *Physical Review B* **65**, 045303 (2001).
- 120 Gao, K., Yu, G., Zhou, Y. *et al.* Insulator-quantum Hall conductor transition in high electron density gated InGaAs/InAlAs quantum wells. *J. Appl. Phys.* **108**, 063701 (2010).

- 121 Poon, S., Pan, J. & Tok, E. Nucleation and growth of cobalt nanostructures on highly oriented pyrolytic graphite. *PCCP* **8**, 3326 (2006).
- 122 Bardarson, J. H., Tworzydło, J., Brouwer, P. & Beenakker, C. One-parameter scaling at the Dirac point in graphene. *Phys. Rev. Lett.* **99**, 106801 (2007).
- 123 Chan, K. T., Lee, H. & Cohen, M. L. Gated adatoms on graphene studied with first-principles calculations. *Physical Review B* **83**, 035405 (2011).
- 124 Wehling, T. O., Balatsky, A. V., Katsnelson, M. I., Lichtenstein, A. I. & Rosch, A. Orbitally controlled Kondo effect of Co adatoms on graphene. *Physical Review B* **81**, 115427 (2010).
- 125 Wong, P., de Jong, M., Leonardus, L., Siekman, M. & van der Wiel, W. Growth mechanism and interface magnetic properties of Co nanostructures on graphite. *Physical Review B* **84**, 054420 (2011).
- 126 Zan, R., Bangert, U., Ramasse, Q. & Novoselov, K. S. Metal–Graphene Interaction Studied via Atomic Resolution Scanning Transmission Electron Microscopy. *Nano Lett.* **11**, 1087, doi:10.1021/nl103980h (2011).
- 127 Nomura, K., Ryu, S., Koshino, M., Mudry, C. & Furusaki, A. Quantum Hall effect of massless Dirac fermions in a vanishing magnetic field. *Phys. Rev. Lett.* **100**, 246806 (2008).
- 128 Fisher, M. P. A. Quantum phase transitions in disordered two-dimensional superconductors. *Phys. Rev. Lett.* **65**, 923 (1990).
- 129 Wei, H. P., Tsui, D. C., Paalanen, M. A. & Pruisken, A. M. M. Experiments on Delocalization and Universality in the Integral Quantum Hall Effect. *Phys. Rev. Lett.* **61**, 1294 (1988).

- 130 Pruisken, A. M. M. Universal Singularities in the Integral Quantum Hall Effect. *Phys. Rev. Lett.* **61**, 1297 (1988).
- 131 Huckestein, B. Scaling theory of the integer quantum Hall effect. *Reviews of Modern Physics* **67**, 357 (1995).
- 132 Hwang, S., Wei, H., Engel, L., Tsui, D. & Pruisken, A. Scaling in spin-degenerate Landau levels in the integer quantum Hall effect. *Physical Review B* **48**, 11416 (1993).
- 133 Koch, S., Haug, R., Klitzing, K. & Ploog, K. Size-dependent analysis of the metal-insulator transition in the integral quantum Hall effect. *Phys. Rev. Lett.* **67**, 883 (1991).
- 134 Brandes, T. Inelastic scattering, multifractality, and scaling in the integer quantum Hall effect. *Physical Review B* **52**, 8391 (1995).
- 135 Aoki, H. Aharonov-Bohm effect for the quantum Hall conductivity on a disordered lattice. *Phys. Rev. Lett.* **55**, 1136 (1985).
- 136 Huckestein, B. & Kramer, B. One-parameter scaling in the lowest Landau band: Precise determination of the critical behavior of the localization length. *Phys. Rev. Lett.* **64**, 1437 (1990).
- 137 Huo, Y. & Bhatt, R. N. Current carrying states in the lowest Landau level. *Phys. Rev. Lett.* **68**, 1375 (1992).
- 138 Liu, D. & Das Sarma, S. Universality in Two-Dimensional Landau Level Localization. *Mod. Phys. Lett. B* **7**, 449 (1993).
- 139 Chalker, J. & Coddington, P. Percolation, quantum tunnelling and the integer Hall effect. *Journal of Physics C: Solid State Physics* **21**, 2665 (1988).

- 140 Khmel'nitskii, D. Pis' ma Zh. Eksp. Teor. Fiz. 38, 454 (1983)[JETP Lett. 38, 552 (1983)]. *Phys. Lett. A* **106**, 182 (1984).
- 141 Li, W., Xia, J. S., Vicente, C. *et al.* Crossover from the nonuniversal scaling regime to the universal scaling regime in quantum Hall plateau transitions. *Physical Review B* **81**, 033305 (2010).
- 142 Geim, A. K. & Novoselov, K. S. The rise of graphene. *Nat Mater* **6**, 183 (2007).
- 143 Hong, X., Zou, K. & Zhu, J. Quantum scattering time and its implications on scattering sources in graphene. *Physical Review B* **80**, 241415 (2009).
- 144 Dean, C., Young, A., Meric, I. *et al.* Boron nitride substrates for high-quality graphene electronics. *Nature Nanotechnology* **5**, 722 (2010).
- 145 Castro, E. V., Novoselov, K., Morozov, S. *et al.* Biased bilayer graphene: semiconductor with a gap tunable by the electric field effect. *Phys. Rev. Lett.* **99**, 216802 (2007).
- 146 Meric, I., Han, M. Y., Young, A. F. *et al.* Current saturation in zero-bandgap, top-gated graphene field-effect transistors. *Nat Nano* **3**, 654 (2008).
- 147 Hong, X., Posadas, A., Zou, K., Ahn, C. H. & Zhu, J. High-Mobility Few-Layer Graphene Field Effect Transistors Fabricated on Epitaxial Ferroelectric Gate Oxides. *Phys. Rev. Lett.* **102**, 136808 (2009).
- 148 Liao, L., Bai, J., Qu, Y. *et al.* High-oxide nanoribbons as gate dielectrics for high mobility top-gated graphene transistors. *Proceedings of the National Academy of Sciences* **107**, 6711 (2010).

- 149 Farmer, D. B., Chiu, H.-Y., Lin, Y.-M. *et al.* Utilization of a Buffered Dielectric to Achieve High Field-Effect Carrier Mobility in Graphene Transistors. *Nano Lett.* **9**, 4474, doi:10.1021/nl902788u (2009).
- 150 Ponomarenko, L. A., Yang, R., Mohiuddin, T. M. *et al.* Effect of a High- κ Environment on Charge Carrier Mobility in Graphene. *Phys. Rev. Lett.* **102**, 206603 (2009).
- 151 Xia, J. L., Chen, F., Wiktor, P., Ferry, D. K. & Tao, N. J. Effect of Top Dielectric Medium on Gate Capacitance of Graphene Field Effect Transistors: Implications in Mobility Measurements and Sensor Applications. *Nano Lett.* **10**, 5060, doi:10.1021/nl103306a (2010).
- 152 Konar, A., Fang, T. & Jena, D. Effect of high- gate dielectrics on charge transport in graphene-based field effect transistors. *Physical Review B* **82**, 115452 (2010).
- 153 Bolotin, K. personal communication.
- 154 Li, W., He, Y., Wang, L. *et al.* Electron localization in metal-decorated graphene. *Physical Review B* **84**, 045431 (2011).
- 155 Tombros, N., Jozsa, C., Popinciuc, M., Jonkman, H. T. & van Wees, B. J. Electronic spin transport and spin precession in single graphene layers at room temperature. *Nature* **448**, 571 (2007).
- 156 Cho, S., Chen, Y. F. & Fuhrer, M. S. Gate-tunable graphene spin valve. *Appl. Phys. Lett.* **91**, 123105 (2007).
- 157 Min, H., Hill, J., Sinitsyn, N. *et al.* Intrinsic and Rashba spin-orbit interactions in graphene sheets. *Physical Review B* **74**, 165310 (2006).

- 158 Garaj, S., Hubbard, W., Reina, A. *et al.* Graphene as a subnanometre trans-electrode membrane. *Nature* **467**, 190 (2010).
- 159 Postma, H. W. C. Rapid Sequencing of Individual DNA Molecules in Graphene Nanogaps. *Nano Lett.* **10**, 420, doi:10.1021/nl9029237 (2010).
- 160 Schneider, G. g. F., Kowalczyk, S. W., Calado, V. E. *et al.* DNA Translocation through Graphene Nanopores. *Nano Lett.* **10**, 3163, doi:10.1021/nl102069z (2010).